2006

A methanol and hydrogen peroxide fuel cell using non-noble catalysts in alkaline solution

Woosuk Sung
Louisiana State University and Agricultural and Mechanical College

A METHANOL AND HYDROGEN PEROXIDE FUEL CELL USING NON-NOBLE CATALYSTS IN ALKALINE SOLUTION

A Thesis

Submitted to the Graduate Faculty of the
Louisiana State University and
Agricultural and Mechanical College
in partial fulfillment of the
requirements for the degree of
Master of Science in Electrical Engineering

in

The Department of Electrical and Computer Engineering

by
Woosuk Sung
B.S., Sungkyunkwan University, 2003
December 2006

ACKNOWLEGEMENTS

First and foremost, I would like to express my deepest gratitude to my advisor, Dr. Jin-Woo Choi, for his constant encouragement, guidance, and research support throughout my master's studies. His technical advice and suggestions made this work wonderful learning experience.

Also, I would like to thank to my committee members, Dr. Pratul K. Ajmera and Dr. Bingqing Wei, for taking time out of their busy schedule and agreeing to be part of my committee.

I would like to give special thanks to my friend, Kyungnam Kang, for his help and support during this difficult time. In addition, I would like to thank my other friends here at LSU and back home for all their help, love, and support.

Finally, I am grateful to my beloved parents who have always stood behind me regardless of my decisions. They have encouraged me to achieve my degree and succeed in life more than anyone. I hope the effort that I put to complete this degree will be a new starting point for my professional career that will open many doors to future success.

TABLE OF CONTENTS

LIST OF TABLES

LIST OF FIGURES

ABSTRACT

A primary goal of this work is to develop a novel liquid-based microscale fuel cell using non-noble metal catalysts. The developed fuel cell is based on a membraneless structure. The operational complications of a proton exchange membrane lead the development of a fuel cell with the membraneless structure. Non-noble metals with relatively mild catalytic activity, nickel hydroxide and silver oxide, were employed as anode and cathode catalysts to minimize the effect of cross reactions with the membraneless structure. Along with nickel hydroxide and silver oxide, methanol and hydrogen peroxide were selected as a fuel at the anode and an oxidant at the cathode. Using such a liquid-phase fuel and oxidant, an all-liquid system can be achieved and the effect of by-products becomes less significant. The electrochemical reactions of methanol and hydrogen peroxide at nickel hydroxide and silver oxide were electrochemically analyzed using cyclic voltammetry. The methanol and hydrogen peroxide fuel cell concept was experimentally validated using a macroscale fuel cell with the membraneless structure. Also, with the macroscale fuel cell, the effect of operational conditions was examined including the catalyst surface conditions, fuel mixture composition, and distance between anode and cathode. Within macroscale distances, a shorter distance between anode and cathode resulted in a higher fuel cell output power. Microscale fuel cells with the membraneless structure were also developed. Four different designs, 10, 20, 50, and 100 μm width and spacing of interdigitated microelectrodes, were compared to investigate the distance effect in microscale distances.

With a fuel mixture flow rate of 200 μl/min, a maximum output power density of 28.73 $\mu W/cm^2$ was achieved from the 10 μm design, which was nearly three times higher than the 100 μm design. Besides, the microfluidic behavior of the microscale fuel cell was tested with different fuel mixture flow rates. The developed microscale fuel cell features no proton exchange membrane, inexpensive catalysts, and simple planar structure, which enables high design flexibility and easy integration of the microscale fuel cell into actual microfluidic systems and portable applications.

CHAPTER 1. INTRODUCTION

1.1 Overview

This thesis presents the development and demonstration of a methanol and hydrogen peroxide fuel cell using nickel hydroxide and silver oxide as anode and cathode catalysts in an alkaline solution. In essence, this fuel cell depends on the anodic oxidation of methanol on nickel hydroxide and the cathodic reduction of hydrogen peroxide on silver oxide in the presence of hydroxyl ions at both electrodes. In the actual operation, though, the electrochemical reactions in this fuel cell become complicated, mostly due to the lack of a proton exchange membrane between anode and cathode.

To yield insight on the complex nature of the associated reaction mechanism, the anode and cathode are characterized using an electroanalytical method. The cyclic voltammetry setup used as the electroanalytical apparatus in this work is constructed with the LabVIEW-controlled Field Point modules in combination with an operational amplifier-based potentiostat and a three-electrode cell. The reaction mechanism study includes not only desired reactions such as the nickel hydroxide-catalyzed oxidation of methanol and silver oxide-catalyzed reduction of hydrogen peroxide but also their cross reactions.

Based on this electroanalysis, a membraneless macroscale fuel cell is developed, and the diverse design considerations of this fuel cell such as the electrode conditions, fuel mixture composition, and distance between anode and cathode are experimentally

studied. The optimization of such components requires a consideration of both the magnitude and stability of the fuel cell output.

Following the membraneless macroscale fuel cell tests, a membraneless microscale fuel cell is designed and fabricated to further investigate the effect of distance between anode and cathode on the fuel cell output. A reduced diffusion length is expected to cause a reduced diffusion time, thereby expediting the electrochemical reactions and thus enhancing the output power.

The developed fuel cell does not require noble metal catalysts such as platinum or ruthenium. Due to its simple structure, the anode and cathode can be defined on the same plane without a separating membrane so that the fuel cell dimensions can be flexibly adjusted to meet specific design needs for the applications of micro power sources.

1.2 Research Goals

The goals of this research are:

1) To develop a fuel cell based on a membraneless structure, liquid fuel and oxidant, and non-noble metal catalysts;

2) To analyze electrochemical reactions in the developed fuel cell by means of an electroanalytical method;

3) To examine the effect of operational conditions on the fuel cell output using the macroscale fuel cell, and

4) To design, fabricate, and characterize the microscale fuel cells.

A novel liquid-based microscale fuel cell using non-noble catalysts is developed for the applications of microscale power sources. The developed fuel cells are based on a membraneless structure that can eliminate the operational complications imposed by the

use of a proton exchange membrane. Nickel hydroxide and silver oxide are employed as anode and cathode catalysts in order to minimize cross reactions with the membraneless structure. Anodic oxidation reactions at nickel hydroxide as well as cathodic reduction reactions at silver oxide are electroanalytically studied using cyclic voltammetry. With the macroscale fuel cell, the effect of operational conditions is experimentally studied including the catalyst surface conditions, fuel mixture composition, and distance between anode and cathode. The effect of distance between anode and cathode is further investigated using the microscale fuel cells.

1.3 Thesis Outline

The main body of this thesis comprises of six chapters.

Chapter 2 discusses the background for the research on liquid-based microscale fuel cells. The related literature is reviewed. This thesis work is initiated upon reflecting on the current status and problem statement of liquid-based microscale fuel cells. At the beginning, fuel cell basics are also presented.

Chapter 3 describes the associated reaction mechanism study on the basis of cyclic voltammetry. Readers interested in further discussion on the cyclic voltammetry setup developed in this work are referred to the Appendix.

Chapter 4 presents the membraneless macroscale fuel cell that provides the experimental validation to the non-noble catalysts deployed in this fuel cell. Also, its design considerations such as the electrode conditions, fuel mixture composition, and distance between anode and cathode are experimentally studied.

Chapter 5 presents the membraneless microscale fuel cell that demonstrates the extension of the distance effect observed in the membraneless macroscale fuel cell. The microfabrication process of this fuel cell is described in detail.

Chapter 6 summarizes the achieved works and suggests possible future research activities.

CHAPTER 2. BACKGROUND AND RESEARCH MOTIVATION

2.1 Fuel Cell Fundamentals

2.1.1 Basic Principles

A fuel cell is an electrochemical device that converts chemical energy into electrical energy. In terms of such energy conversion, fuel cells may look similar to batteries and combustion engines that are used to generate electrical energy. But unlike batteries, fuel cells can produce electricity as long as they are supplied with a fuel. Besides, in contrast to combustion engines, fuel cells can produce electricity directly from electrochemical reactions without multiple energy conversions, including heat and mechanical motions.

In a typical fuel cell, a fuel, usually hydrogen, is provided to the anode and oxidized, releasing protons and electrons. The generated electrons pass through an external load to do electrical work and travel back to the cathode, whereas the protons migrate across the electrolyte to the cathode. In the cathode, an oxidant, usually oxygen in the air, is supplied and reduced with the protons and electrons, creating pure water as a by-product. Figure 2.1 illustrates the comparison of a fuel cell and a rechargeable battery.

2.1.2 Historical Background of Fuel Cells

The history of fuel cells can be traced back to the early 1800s. The judge and scientist, Sir William Robert Grove, discovered that if electricity could split water into hydrogen and oxygen, then the opposite would also be possible such that combining hydrogen and oxygen in some way would produce electricity [1-2]. To test this

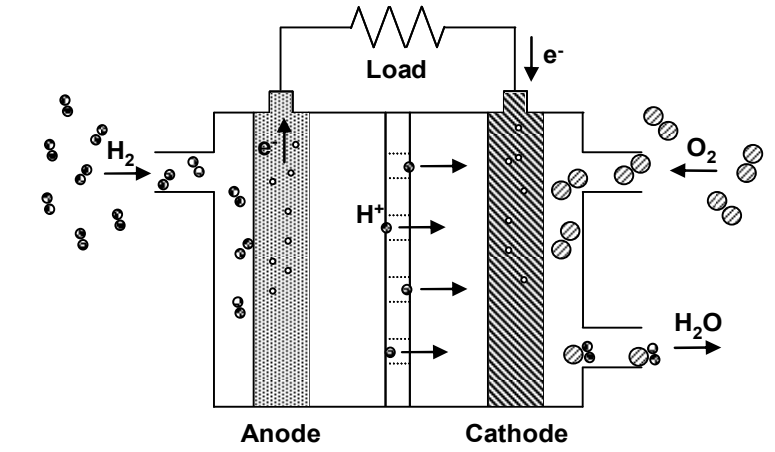

(a)

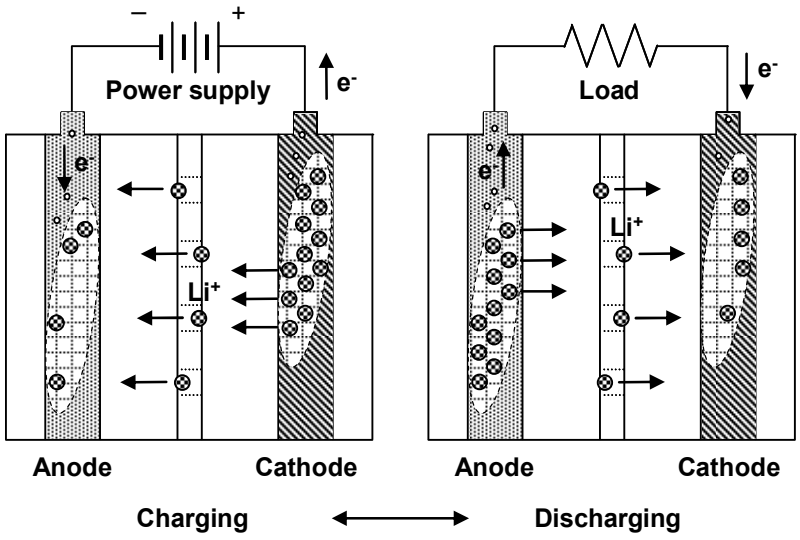

(b)

Figure 2.1. Schematic illustrations of a fuel cell and a rechargeable battery. Unlike batteries, fuel cells can produce electricity as long as they are supplied with a fuel. (a) A hydrogen fuel cell depends on the anodic oxidation: $H_2 \rightarrow 2H^+ + 2e^-$ and the cathodic reduction: $1/2O_2 + 2H^+ + 2e^- \rightarrow H_2O$. (b) When a lithium ion rechargeable battery is charged, lithium ions in the cathode (lithium compound) migrate via a separator to the anode (carbon material) and a charging current flows: $C_6 + 2LiCoO_2 \rightarrow LiC_6 + 2Li_{0.5}CoO_2$. By contrast, when a lithium ion rechargeable battery is discharged, lithium ions in the anode (carbon material) migrate via a separator to the cathode (lithium compound) and a discharging current flows: $LiC_6 + 2Li_{0.5}CoO_2 \rightarrow C_6 + 2LiCoO_2$.

hypothesis, Grove enclosed two platinum strips in separate sealed glass tubes; one contained hydrogen and the other contained oxygen. Once these containers were dipped into a dilute sulphuric acid solution, a current began to flow between the two electrodes and the water was formed in the oxygen glass tube. Grove connected several of these devices in series and completed what he referred to as a "gas battery" in 1839.

About 50 years later, the chemists, Ludwig Mond and Charles Langer, coined the term "fuel cell," as they attempted to develop the device that could convert coal or carbon into electricity [1].

In 1932, the engineer, Francis Thomas Bacon, developed the first successful fuel cell using hydrogen, oxygen, an alkaline electrolyte, and nickel electrodes – inexpensive alternatives to the catalysts used before such as platinum. In 1952, Bacon and his co-worker demonstrated a fuel cell capable of producing the maximum output power of 5 kW, enough to power a welding machine [1-2].

In the late 1950s, the National Aeronautics and Space Administration (NASA) was looking for a compact and efficient electricity generator for use on space missions [1-2]. NASA had already concluded that for this purpose nuclear power was too dangerous, batteries were too heavy, and solar power was too expensive, and thus began to search for an alternative. In the end, the fuel cell was chosen as a possible solution, and NASA soon proceeded with a number of research works in alliance with General Electric (GE), Pratt & Whitney (P&W), etc., to develop fuel cells suitable for spacecraft. As a result of such efforts, both alkaline and polymer electrolyte fuel cells have successfully demonstrated their capabilities in a series of manned space flights such as the Apollo, Gemini and Space Shuttle. Fuel cells now have a proven role as an electric

power source as well as drinkable water source for spacecraft. Since their successful demonstrations in space applications, fuel cells have achieved widespread recognition by industry and government as a clean and efficient energy source for the future. Today, a large research effort is dedicated to developing fuel cells for their commercialization in a range of applications. Fuel cells are now expected to replace conventional power sources in coming years, from miniature fuel cells to be used in cellular phones to large fuel cells for powering electric vehicles.

2.1.3 Advantages and Disadvantages of Fuel Cells

Fuel cells have several important advantages over conventional electrical energy generation. Fuel cells are simple in construction, with few moving parts. Due to this uncomplicated structure, fuel cells can be reliable and long-lasting; it makes fuel cells silent as well. In addition to those benefits, fuel cells from which water would be the only by-product are environmentally friendly. Besides, in contrast to batteries, fuel cells have continuous operation capability by refueling.

On the other hand, one of the greatest drawbacks of fuel cells is the cost involved. According to the U.S. Department of Energy (DOE) [3], fuel cells cost from $1,500 to $4,500 per kilowatt (kW), depending upon their type and end-use application. By comparison, diesel engines cost $800 to $1,500 per kilowatt (kW), and natural gas turbines even less. The costs are expected to decrease in the future (projections are for around $400/kW) as more fuel cells are produced and utilized. After cost, fuel supply is the next greatest problem. Hydrogen is the most preferred fuel of fuel cells due to its high reactivity for the anode oxidation reaction and lack of any emission other than pure water. However, hydrogen does not exist naturally as fossil fuel, and so over 95% of

hydrogen is currently produced from fossil sources such as methane (CH_4), ammonia (NH_3), methanol (CH_3OH), ethanol (C_2H_5OH), gasoline (C_8H_{18}), etc. [4]. These hydrogen sources need to go through fuel processing to be converted to mainly hydrogen with the addition of a small percentage of carbon dioxide, using different chemical conversion techniques [5]. However, after taking into account all potential losses during fuel processing and handling, fuel cells are comparatively neither more efficient nor completely environmentally friendly.

2.1.4 Fuel Cell Types and Potential Applications

A variety of fuel cells are currently in the different stages of development for their possible commercialization. Major differences among various fuel cells are shown in Table 2.1.

2.1.4.1 Classification by the Type of Electrolyte

The different fuel cell types are usually classified by the electrolyte that is used, though there are other important differences as well.

Proton exchange membrane fuel cells (PEMFCs) – The electrolyte in the PEMFCs is an ion-exchange membrane that is conductive to protons. Due to critical water management in this membrane, the operating temperature of the PEMFCs is limited, usually less than 100°C. Catalysts, mostly platinum, for both anode and cathode react with a hydrogen-rich fuel and oxygen that are fed into the anode and the cathode, respectively. The PEMFCs have been employed in a range of applications, from a few watts for portable electronic devices to hundreds of kilowatts for buses and combined heat and power (CHP) systems [6-7].

Table 2.1. Summary of major differences of the fuel cell types [14].

Fuel cell type	Electrolyte	Working temp. (°C)	Mobile ion	Electrochemical reactions
PEMFC	Ion exchange membrane	30 – 100	H^+	Ox: $H_2 \rightarrow 2H^+ + 2e^-$ Red: $1/2O_2 + 2H^+ + 2e^- \rightarrow H_2O$ Net: $H_2 + 1/2O_2 \rightarrow H_2O$
DMFC	Ion exchange membrane	20 – 90	H^+	Ox: $CH_3OH + H_2O \rightarrow 6H^+ + 6e^- + CO_2$ Red: $3/2O_2 + 6H^+ + 6e^- \rightarrow 3H_2O$ Net: $CH_3OH + 3/2O_2 \rightarrow CO_2 + 2H_2O$
AFC	Mobilized or immobilized potassium hydroxide	50 – 200	OH^-	Ox: $H_2 + 2OH^- \rightarrow 2H_2O + 2e^-$ Red: $1/2O_2 + H_2O + 2e^- \rightarrow 2OH^-$ Net: $H_2 + 1/2O_2 \rightarrow H_2O$
PAFC	Immobilized liquid phosphoric acid	~ 220	H^+	Ox: $H_2 \rightarrow 2H^+ + 2e^-$ Red: $1/2O_2 + 2H^+ + 2e^- \rightarrow H_2O$ Net: $H_2 + 1/2O_2 \rightarrow H_2O$
MCFC	Immobilized liquid molten carbonate	~ 650	CO_3^{2-}	Ox: $H_2 + CO_3^{2-} \rightarrow H_2O + CO_2 + 2e^-$ Red: $1/2O_2 + CO_2 + 2e^- \rightarrow CO_3^{2-}$ Net: $H_2 + 1/2O_2 + CO_2 \rightarrow H_2O + CO_2$
SOFC	Ceramic	500 – 1000	O^{2-}	Ox: $H_2 + O^{2-} \rightarrow H_2O + 2e^-$ Red: $1/2O_2 + 2e^- \rightarrow O^{2-}$ Net: $H_2 + 1/2O_2 \rightarrow H_2O$

Alkaline fuel cells (AFCs) – The AFCs use an electrolyte composed largely of a potassium hydroxide (KOH) solution whose concentration can be varied with the operating temperature, ranging from 65 to 220°C. The overall reaction of the AFCs is the same as that of the PEMFCs, but the reactions at each electrode are different. At the anode, hydrogen combines with hydroxyl ions to produce electrons and water, while oxygen combines with electrons from the anode and water in the electrolyte at the cathode to produce hydroxyl ions. The AFCs are very sensitive to carbon dioxide (CO_2) reacting with potassium hydroxide, thus changing it to potassium carbonate (K_2CO_3). As a result, the amount of hydroxyl ions decreases in the electrolyte whereas the amount of carbonate ions increases. This alters the composition of the electrolyte and degrades the performance of the AFCs. The CO_2-free hydrogen and oxygen are therefore required, which limits the applications of the AFCs except in space and underwater vehicles [8].

Phosphoric acid fuel cells (PAFCs) – The PAFCs use concentrated phosphoric acid (H_3PO_4) as an electrolyte that can allow high operating temperatures with no concerns about water management in the membrane. Operating temperatures around 200°C increase the tolerance of platinum catalysts against carbon monoxide (CO) so that the externally reformed hydrogen, usually from natural gas, can be supplied to the PAFCs. On the other hand, the components for the PAFCs are required to resist corrosion due to the use of the concentrated phosphoric acid. For small stationary power generation, the phosphoric acid fuel cell systems, typically in the 50 to 200 kW range, are commercially available now [9-10].

Molten carbonate fuel cells (MCFCs) – The electrolyte in the MCFCs is a molten mixture of alkali carbonates. At high operating temperatures, typically 600 to

700°C, the alkali carbonates become conductive to carbonate ions (CO_3^2) so that these ions can flow from the cathode to the anode where they combine with hydrogen, producing water, carbon dioxide, and electrons. Then, electrons travel an external circuit providing electric power and return to the cathode. High-temperature fuel cells such as MCFCs and SOFCs have both advantages and disadvantages compared to low-temperature fuel cells such as PEMFCs. The high operating temperatures may imply that a reaction rate can be fast enough with a comparatively inexpensive catalyst – nickel at the anode and nickel oxide at the cathode in the case of the MCFCs. In the MCFCs, due to the high operating temperatures, natural gas can be internally reformed to produce hydrogen without an external fuel processor. In addition, the by-product heat from the high-temperature fuel cells can be used to generate high-pressure steam that can be used in many industrial and commercial applications. By contrast, the high-temperature fuel cells require a significant time to reach operating conditions and respond slowly to varying power demands. Such characteristics make the MCFCs better suited for constant power applications, for example, stationary power generation systems [11].

Solid oxide fuel cells (SOFCs) – The operating temperatures of the SOFCs, from 800 to 1000°C, are currently the highest. To operate at such high temperatures, the electrolyte is a solid ceramic material like zirconium dioxide (ZrO_2) stabilized with the addition of yttrium oxide (Y_2O_3) that becomes conductive to oxygen ions beyond about 800°C. At the cathode, oxygen molecules are split into oxygen ions and produce electrons. The oxygen ions are conducted across the electrolyte and react with hydrogen at the anode, releasing electrons. The electrons travel an external circuit providing electric power. Suitable applications for the SOFCs are very similar to those for the

MCFCs because their characteristics are analogous in terms of high operating temperatures [12-13].

2.1.4.2 Classification by the Type of Fuel

In essence, the fuel that is used for a fuel cell is hydrogen. In other words, there can be a number of materials that could carry hydrogen; however, their end product for use in a fuel cell is hydrogen. In the oxidation reaction of a fuel cell, a fuel (or reductant) is hydrogen regardless of the type of the fuel species supplied. Hydrogen storage materials of interest are, for example, cryogenic hydrogen, methanol, ethanol, ammonia, and sodium borohydride ($NaBH_4$) solution [14]. Using liquid-phase hydrogen carriers, fueling for fuel cells can be facilitated compared to using gas-phase hydrogen, that is, normally compressed at high pressure. However, each of those hydrogen carriers has its own critical limitations. Apart from individual drawbacks, those hydrogen carriers commonly undergo a significant loss in stored energy during fuel processing taking place prior to actual use, such as a liquefaction process for cryogenic hydrogen, a reformation process for methanol and ethanol, and a chemical reaction with water for sodium borohydride.

This problem can be solved by using the liquid-phase hydrogen carriers "directly" as a fuel, as opposed to extracting hydrogen from them using fuel processing. Among many hydrogen carriers, an approach has recently been shown in the use of methanol as a fuel species of direct methanol fuel cells (DMFCs). Methanol is a readily available and low-cost liquid fuel whose volumetric energy density is much higher than that of hydrogen [14], which is the main advantage of the DMFCs. Despite the low output power of the DMFCs, there are many potential applications where a low power but a high

energy density is required such as 'always on' mobile telephones, personal digital assistants, remote monitoring and sensing equipment [15]. In addition to the DMFCs, there are also other fuel cells based on the direct use of a liquid fuel, direct ethanol fuel cells (DEFCs) [16]; direct formic acid fuel cells (DFAFCs) [17]; direct dimethyl ether fuel cells (DMEFCs) [18], and direct borohydride fuel cells (DBFCs) [19].

2.2 Liquid-Based Microscale Fuel Cells

2.2.1 Introduction

Recently, there has been a rapidly growing demand for high energy density power sources for portable electronic telecommunication and computing devices such as mobile phones, personal digital assistants, and laptop computers [20]. Battery technology has advanced significantly over the years so that such needs can be generally met by lithium ion [21] and nickel metal hydride-based rechargeable batteries [22]. However, with the ever-increasing energy demand in recent years, the power available from the rechargeable batteries may become insufficient to keep pace with the power required from the portable devices [23].

Table 2.2 shows thermodynamic energy densities and practical packaging efficiencies for several batteries and fuel cells [24]. These energy densities are listed in terms of a volumetric energy density because the volume of a device is a more important design consideration than its weight. On a gravimetric basis, the energy densities of fuel cells are even more advantageous. As shown in Table 2.2, the energy density of a methanol fuel cell exceeds that of all battery types by nearly an order of magnitude. When compared to batteries, this higher energy density is the main advantage of methanol fuel cells in addition to their continuous operation capability by refueling.

Table 2.2. Comparison of thermodynamic energy densities, packaging efficiencies, and practical energy densities of various batteries and fuel cells [24].

Battery and fuel cell type	Energy density (Wh/l)	Packaging efficiency (%)	Practical energy density (Wh/l)	Electrochemical reaction
Li-polymer	1350	27	360	$C_6 + 2LiCoO_2 \rightarrow LiC_6 + 2Li_{0.5}CoO_2$
Li-metal hydride	988	21	205	$NiOOH + MH \rightarrow Ni(OH)_2 + M$
Ni-Cad	439	27	120	$2NiOOH + Cd + 2H_2O \rightarrow 2Ni(OH)_2 + Cd(OH)_2$
H_2 fuel cell	2.8	50 (est.)	1.4	$H_2 + 1/2O_2 \rightarrow H_2O$ unpressurized gaseous H_2 and air
H_2 fuel cell	4632	50 (est.)	2316	$H_2 + 1/2O_2 \rightarrow H_2O$ liquid H_2 and air
Methanol fuel cell	4767	40 (est.)	1906	$CH_3OH + 3/2O_2 \rightarrow CO_2 + 2H_2O$ 100% methanol
Methanol fuel cell	334	40 (est.)	134	$CH_3OH + 3/2O_2 \rightarrow CO_2 + 2H_2O$ 2M methanol (7%) in water

When considering only fuel cells, it is apparent that hydrogen is not comparable with methanol in terms of energy density unless liquefied or compressed, though neither of them is suited to the fuel cell for portable applications. This limitation is caused by the inherent characteristic of hydrogen which has a low volumetric energy density in contrast to a high gravimetric energy density. Methanol therefore emerges as one of the favorable fuels for fuel cells, particularly for portable applications [25-31]. Although methanol is currently most widely used, the advantages of methanol over hydrogen can be also expected with other liquid fuels such as ethanol [16], formic acid [17], and dimethyl ether [18], which are considered low-cost and readily available.

In addition to the use of liquid fuels, fuel cells for portable applications are expected to be miniaturized. Through miniaturization, a fuel cell can be scaled down to fit into a form factor appropriate for portable devices and even integrated microelectromechanical systems (MEMS). The miniaturization of a fuel cell can be realized by scaling down of components in the fuel cell such as flow channels for a fuel or an oxidant. Scaling down the channel dimensions not only alters the flow dynamics but also increases the surface area and reduces the length for reactant diffusion [32]. In this respect, a microscale fuel cell is also expected to deliver a higher power density utilizing an increased mass transfer rate that causes a faster electrochemical reaction rate.

For these reasons, the liquid-based microscale fuel cell has drawn wide attention as a miniaturized power source.

2.2.2 Literature Review of Liquid-Based Microscale Fuel Cells

Since the late 1990s, numerous research interests have been directed towards the development and characterization of liquid-based microscale fuel cells [25-34].

The Corrosion Research Center (CRC) at the University of Minnesota has pioneered the development of miniaturized fuel cells fabricated on micromachined silicon wafers [25-26]. The maximum power density obtained from the fuel cell, named m-PEFC (microfabricated, miniature polymer electrolyte fuel cells), with a working volume of 12 mm^3 was about 15 mW/cm^2 at room temperature. The membrane electrode assembly (MEA) in the m-PEFC consisted of platinum-ruthenium (Pt-Ru) electrodeposits (1.28 mg/cm^2) on the anode, platinum black (2.5 mg/cm^2) on the cathode, and Nafion® 117 membrane.

The Jet Propulsion Laboratory (JPL) has successfully demonstrated a prototype of a miniaturized DMFC based on a monopolar strip stack, so called "flat-pack," instead of the conventional bipolar stack [27]. Single fuel cells were placed side by side on the same membrane and they were electrically connected in series. The MEA in the single fuel cells was prepared by pressing the anode, electrolyte, and cathode at 8.62 MPa and 146°C. The platinum catalyst loading in both electrodes was 4 – 6 mg/cm^2. The Nafion® 117 was employed as the proton exchange membrane while segregating the anode and cathode compartments. Two "flat-packs" can be arranged in a back-to-back configuration with a common methanol feed, resulting in a so-called "twin-pack." In this stack assembly, six cells were connected in series in a planar configuration such that power densities of over 10 mW/cm^2 were achieved with 1 M methanol as a fuel and ambient air (20 to 25°C) as an oxidant.

A monopolar stack has also been demonstrated by Samsung Advanced Institute of Technology (SAIT), which has a low-profile form factor to fit in miniaturized fuel cells for powering portable electronics [28]. Single-cell tests at various methanol

concentrations and at different air feed rates resulted in power densities in the range of 10 – 50 mW/cm^2. The MEA in the monopolar stack was fabricated with a platinum-ruthenium black as an anode catalyst and a platinum black as a cathode catalyst sputtered onto a hybrid membrane. The hybrid membrane based on Nafion® or Co-PTFS (Co-polymer of poly-trifluorostyren) was prepared and tested for reducing methanol crossover while maintaining the proton conductivity similar to a plain Nafion® membrane near 10^{-1} S/cm.

Recent efforts at Motorola Labs on a miniaturized DMFC have shown that power densities between 15 – 22 mW/cm^2 could be extracted from a stack assembly in which four cells were connected in series in a planar configuration with a MEA area of 13 – 14 cm^2 [29]. The MEA was sandwiched by two porous ceramic plates incorporating the microchannels for delivering a mixture of methanol and water to the MEA and for exhausting carbon dioxide bubbles from the MEA. Platinum-ruthenium alloy and platinum were used as anode and cathode catalysts, respectively. In addition, the Nafion® 117 was also used as the proton exchange membrane while segregating the anode and cathode compartments. As a fuel, 1 M methanol was fed at a rate of 0.45 ml/min by means of a peristaltic pump, while oxygen from ambient air was supplied as an oxidant.

The Electrochemical Engine Center (ECEC) at Pennsylvania State University (PSU), in collaboration with the University of California at Los Angeles (UCLA), has engaged in the development of a micro DMFC [30-31]. The operating conditions of the microfabricated DMFC were 2 M methanol, 60°C, and ambient pressure, which led to the maximum power density of about 50 mW/cm^2. At room temperature, the maximum power density was reduced to 16.5 mW/cm^2. The MEA of the microfabricated DMFC,

with electrodes having an active area of 1.625 cm^2, was made out of the Nafion® 112 membrane that was sandwiched by the catalyzed anode and cathode. An important feature of this MEA was an enhanced resistance to methanol crossover by means of a compact microporous layer coated onto an anode backing structure.

Ethanol also emerges as one of the alternative fuels for liquid-based microscale fuel cells to avoid toxicity and volatility of methanol. Recent studies at the Nanomaterials and Nanomanufacturing Research Center (NNRC) at the University of South Florida on micro direct ethanol fuel cells (DEFCs) have shown an open circuit voltage of 260 mV and a maximum power density of 16.5 mW/cm^2 at room temperature (23°C) with a fuel supply of 8.5 M ethanol solution [33]. The fuel was fed to the anode by the capillary force of the micropores in a porous silicon electrode, resulting in a pressure of about 14.55 kPa in each microcapillary, independent of the orientation. An oxidant, oxygen in the air, was supplied to the cathode by natural convection. The porous silicon substrate at both electrodes was platinized to create catalyst layers and integrated with a Nafion® 115 membrane to build the micro fuel cell stack.

In addition to ethanol, formic acid has also been considered as a fuel for liquid-based microscale fuel cells. Formic acid was introduced to reduce the deleterious effect of fuel crossover across the Nafion® membrane [17]. The benefit of the use of formic acid as a fuel has been demonstrated with microscale silicon-based direct formic acid fuel cells (Si-DFAFCs) [34]. This Si-DFAFC was tested with a palladium or platinum catalyst at the anode and with a forced oxygen or ambient air environment at the cathode. In the presence of a forced oxygen flow on the cathode in conjunction with a palladium catalyst on the anode, a maximum power density of about 30 mW/cm^2 was achieved at

room temperature, limited by mass transfer of formic acid at the anode. Without a forced oxygen flow on the cathode, a maximum power density of 12.3 mW/cm^2 was attained, limited by oxygen transport at the cathode.

2.3 Current Status and Problem Statement

2.3.1 Issues on Liquid-Based Microscale Fuel Cells

Although the liquid-based microscale fuel cells have shown the feasibility of miniaturized power sources, there are a few issues that need to be addressed. One is a proton exchange membrane and the other is undesired by-products.

2.3.1.1 Proton Exchange Membrane

A proton exchange membrane is considered to be an essential component to realize a fuel cell as it allows protons to pass through from the anode to the cathode while preventing fuel species to reach the cathode. However, there is a critical requirement on the thickness of the membrane that could affect design flexibility of a microscale fuel cell. In principle, a thinner membrane can give a higher output power because the membrane thickness defines the distance between anode and cathode. A thinner membrane would reduce the transport time of a charge carrier and thus increase the reaction rate. However, a thinner membrane may also exhibit higher fuel crossover, which leads to mixed potentials on the cathode and a loss in fuel cell performance [35-39]. The optimal thickness of the membrane is desired in order to achieve the maximum fuel cell performance. In addition, segregation of fuel and oxidant compartments by the membrane could make the overall structure of a microscale fuel cell complicated [40]. Besides, a water-rich environment, particularly in a liquid-based fuel cell, leads to the swelling of the membrane [41]. The dimensional instability of the membrane would have

a deleterious effect on the dependability of an entire MEA and the lifetime of a fuel cell in the end.

2.3.1.2 Gaseous By-Product at Anode and Water Dews at Cathode

Gaseous by-product at the anode and water dews at the cathode, which would block fuel and oxidant from anode and cathode surfaces, is another limitation of liquid-based microscale fuel cells. On the anode side, gaseous by-product is normally created by the oxidation reaction of a fuel. For example, methanol at the anode creates carbon dioxide:

$$CH_3OH + H_2O \rightarrow 6H^+ + 6e^- + CO_2. \quad (2.1)$$

The generated carbon dioxide bubbles would accumulate on the anode surface, blocking the methanol transport and hence decreasing the effective area of the methanol oxidation reaction [42-43]. This transport blockage would be more critical in channels of small dimensions as the gaseous by-product could form bubbles and impede fuel flow in the microfluidic channels [44]. On the cathode side, water dews are created by the oxygen reduction reaction:

$$1.5O_2 + 6H^+ + 6e^- \rightarrow 3H_2O. \quad (2.2)$$

In the same sense as bubbles at the anode, cathode flooding could negatively affect the cathode performance [42,45].

2.3.2 Our Approach

The main motivation of this work is to develop and demonstrate a fuel cell based on a membraneless structure, liquid fuel and oxidant, and non-noble metal catalysts. As described earlier (section 2.3.1.1), a proton exchange membrane has limitations in thickness, structural complexity, and a swelling problem due to hydration. Such

operational complications lead the development of a fuel cell without a proton exchange membrane. Besides, due to the absence of a membrane, the distance between anode and cathode will not be restricted by the membrane thickness any more. The distance between anode and cathode determines diffusion length of reacting species. A shorter diffusion length is expected to cause a faster diffusion time, thereby expediting the electrochemical reactions and thus increasing the fuel cell output power.

However, in return for such merits of a membraneless structure, its expected drawbacks are that fuel and oxidant species would mix and reach the opposite electrode, undesirably allowing cross reactions. Even though this tangible loss may be offset to a certain degree by the potential gain from a reduced diffusion length of reacting species, it cannot be a radical solution. Rather, an alternative approach to this problem is to choose appropriate catalysts for use in a membraneless structure. Although platinum and/or platinum-alloys are known as effective catalysts for fuel cells, they are too reactive to be employed in a membraneless structure. Catalytic materials suitable for a membraneless structure are thus expected to be mildly electroactive, preferably, selectively electroactive.

For the selection of appropriate catalysts, the earlier work of C. Iwakura *et al.* [46] has been chosen. The methanol-hydrogen peroxide fuel cell in their work was based on an all-liquid system, which means that both a fuel and an oxidant are in liquid-phase. Methanol was used as a fuel and hydrogen peroxide was used as an oxidant, in the presence of hydroxyl ions. The all-liquid system was proposed to eliminate the problem of a gas-liquid system: the porous material for the gas-feed cathode was occasionally wet, thereby degrading cathode performance. The discharging characteristics of the methanol-hydrogen peroxide fuel cell were examined using several different types of ion exchange

membranes and filter cloths to separate the anode and cathode compartments. This investigation was also carried out without a separator, in which the limiting current density was much lower than that with a separator. In the presence of hydroxyl ions, nickel catalyzed the anodic oxidation of methanol, and silver catalyzed the cathodic reduction of hydrogen peroxide. Unfortunately, however, the detailed properties of the catalysts used were not clearly presented in this literature.

Referring to a similar fuel cell configuration, nickel hydroxide and silver oxide are employed as anode and cathode catalysts for the membraneless fuel cell structure in this work. In combination with nickel hydroxide and silver oxide, methanol and hydrogen peroxide are selected as a fuel at the anode and an oxidant at the cathode, respectively. Thus, a mixture of methanol, hydrogen peroxide, and hydroxyl ions should be supplied as the fuel for the membraneless fuel cell using nickel hydroxide and silver oxide as catalysts. Using such a fuel mixture, an all-liquid system can be achieved and the by-product issues (section 2.3.1.2) become less significant. Although the viability of the all-liquid system using nickel and silver as catalysts has been shown even without a separating membrane, the associated reaction mechanism is still not understood. Uncertain reaction mechanisms contribute to the difficulty of designing fuel cells, particularly microscale fuel cells. The related reaction mechanisms are therefore studied using electroanalytical methods in Chapter 3.

CHAPTER 3. REACTION MECHANISM STUDY

3.1 Introduction

Nickel hydroxide and silver oxide were chosen as anode and cathode catalysts for a membraneless fuel cell structure. Although several studies on methanol oxidation at nickel hydroxide as well as hydrogen peroxide reduction at silver oxide have been reported, the actual catalytic reactions for the fuel cell applications are not well understood. Uncertain reaction mechanisms create difficulties in designing fuel cells, particularly microscale fuel cells. In this chapter, the associated reaction mechanisms are therefore studied using electroanalytical methods.

3.1.1 Electrochemical Cells

An electrochemical cell consists of at least two electrodes where electrochemical reactions take place, an electrolyte for conduction of ions, and an external conductor for conduction of electrons. A unique aspect of electrochemical reactions in the electrochemical cell is the transfer of electrons from a reductant (electron donor) to an oxidant (electron acceptor). Oxidation means that an atom, ion, or molecule releases electrons and is oxidized. On the other hand, reduction means that an atom, ion, or molecule receives electrons and is reduced. These oxidation and reduction reactions, often called redox reactions, must occur in pairs. The number of electrons released in the oxidation reaction must equal the number of electrons received in the reduction reaction. Electrochemical cells are either electrolytic or galvanic. An electrolytic cell requires an external source of electrical energy for operation, while a galvanic cell stores electrical

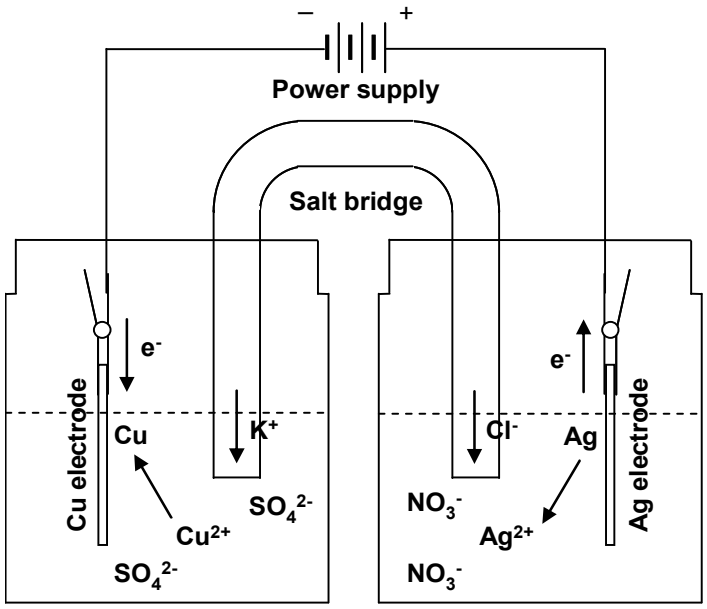

(a)

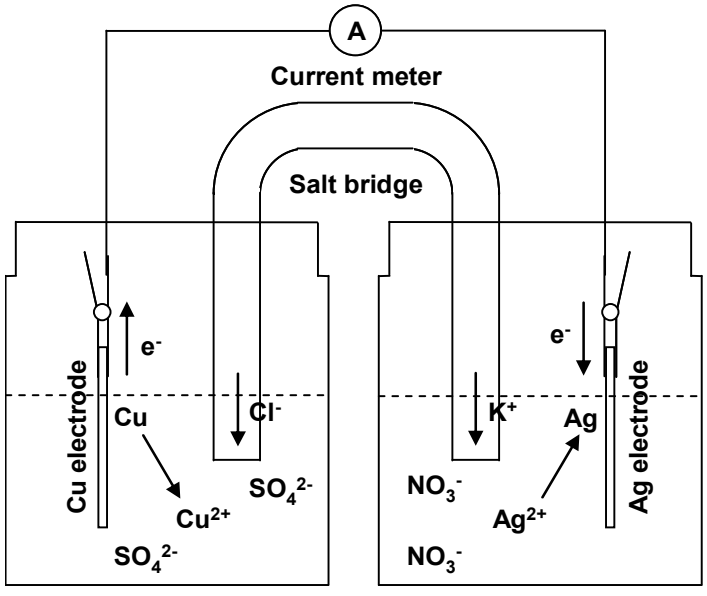

(b)

Figure 3.1. Schematic illustrations of (a) an electrolytic cell and (b) a galvanic cell. A copper-silver cell is exhibited as an example of an electrochemical cell.

energy that leads to spontaneous redox reactions. Figure 3.1 illustrates the comparison of an electrolytic cell and a galvanic cell. In a galvanic cell, the oxidation reaction occurs at the anode, which supplies electrons to the external circuit. The cathode receives electrons from the external circuit for the reduction reaction. Electric charge balance inside the cell is maintained by a flow of ions across an electrolyte separating the anode and cathode compartments. A fuel cell is one such galvanic cell that can produce an electric current. In a typical fuel cell, the electric current is produced by the hydrogen oxidation at the anode and the oxygen reduction at the cathode. Hydrogen and oxygen are commonly catalyzed by platinum and/or platinum-alloys. The fuel cell using nickel hydroxide and silver oxide as catalysts has a basic concept similar to that of a typical fuel cell but differs in many aspects of the reaction mechanism as shown in Figure 3.2. The operation of this fuel cell is based on the anodic oxidation of methanol (CH_3OH) in combination with the cathodic reduction of hydrogen peroxide (H_2O_2). Methanol and hydrogen peroxide are catalyzed by nickel hydroxide and silver oxide, respectively. Additionally, due to the membraneless structure of this fuel cell, methanol and hydrogen peroxide could mix and reach to both electrodes (anode and cathode). As a result, some cross reactions would occur at both electrodes such that hydrogen peroxide could be catalyzed by nickel hydroxide while methanol could be catalyzed by silver oxide.

3.1.2 Fuel Cell Using Nickel Hydroxide and Silver Oxide as Catalysts

3.1.2.1 Electrochemical Reactions on Nickel Hydroxide in Fuel Mixture

There has been great interest in nickel-based materials that were applied as catalysts for water electrolysis [47-48] and organic synthesis [49-50]. In addition, nickel-

based materials can be also used as catalysts for the oxidation of alcohols, particularly in fuel cell applications [46].

Several studies on the oxidation of alcohols at nickel-based materials have been reported [51-54]. Fleischmann *et al.* [51] reported the oxidation of organic compounds at a passivated nickel in an alkaline solution. Most of the applied organic compounds including amines and alcohols were found to be oxidized at the same potential where the nickel surface became oxidized to nickel oxyhydroxide (NiOOH). NiOOH was therefore assumed to be a catalyst for the oxidation of the organic compounds. In addition, products from the oxidation of each organic compound could be predicted using the proposed reaction mechanism. More recently, Taraszewska and Roslonek [52] and El-Shafei [53] investigated the oxidation of methanol at a nickel hydroxide/glassy carbon

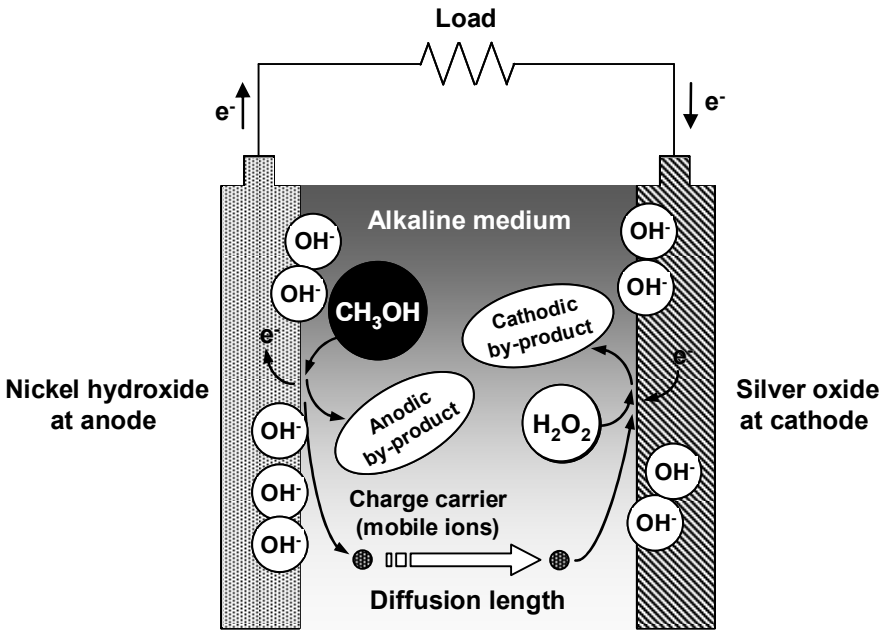

Figure 3.2. Schematic illustration of the fuel cell using nickel hydroxide and silver oxide as catalysts. The distance between anode and cathode determines diffusion length of a charge carrier. In this reaction mechanism scheme, mobile ions are assumed to be cations to illustrate the transport direction of mobile ions.

($Ni(OH)_2$/GC) electrode by cyclic voltammetry. The effects of the methanol concentration and the scan rate on oxidation reaction were experimentally studied. The cyclovoltammograms in their studies also demonstrated the relationship between methanol oxidation and the formation of NiOOH, which is consistent with that reported by Fleischmann *et al.* [51]. Abdel Rahim *et al.* [54] observed that as the voltammetry-cycling progressed, the current for methanol oxidation decreased and the potential for methanol oxidation slightly shifted toward less positive potentials, which indicated a loss of catalytic activity of the electroplated nickel/carbon electrode used.

Despite disagreements with detailed reaction mechanisms in the literature [51-54], the oxidation of methanol is based on the nickel hydroxide cycling between two phases: $Ni(OH)_2$ and NiOOH. $Ni(OH)_2$ and NiOOH can be formed on the nickel surface in an alkaline solution and there exist two different forms of nickel hydroxide. They are denoted as β-$Ni(OH)_2$ and α-$Ni(OH)_2$, which can be oxidized to β-NiOOH and γ-NiOOH, respectively [55-58]. Although the mechanism for such phase transformation is not clearly understood, more electrons can be exchanged with α-$Ni(OH)_2$ compared to β-$Ni(OH)_2$ because the oxidation state of γ-NiOOH is higher than that of β-NiOOH [56]. Therefore, α-$Ni(OH)_2$ is expected to be a better electroactive material for the oxidation of methanol [57]. However, α-$Ni(OH)_2$ transforms into β-$Ni(OH)_2$ in an alkaline solution, resulting in degradation of electrochemical properties [57]. Nickel hydroxide is thus required to be stabilized to make use of it as a catalyst for the oxidation of methanol.

Aside from the oxidation of methanol, the electrochemical reaction of hydrogen peroxide on nickel-based materials should also be considered as it is probable with the membraneless structure. However, very few reports were found regarding the

electrochemical reaction of H_2O_2 on nickel-based materials, particularly in an alkaline solution. Although Hall *et al.* have recently reported the mechanism of hydrogen peroxide oxidation on several electrodes including platinum [59] and nickel [60], their results are not directly applicable to the electrochemical reaction of H_2O_2 on nickel-based materials in an alkaline solution because the results were obtained in a neutral electrolyte.

Thus, in this work, the electrochemical reaction of hydrogen peroxide on nickel hydroxide is experimentally studied using an electroanalytical method. In addition, the nickel hydroxide-catalyzed oxidation of methanol is electrochemically analyzed.

3.1.2.2 Electrochemical Reactions on Silver Oxide in Fuel Mixture

The electrochemical properties of silver-based materials in an alkaline solution, typically silver oxide, have been extensively studied as they are related to the development of the cathode of batteries [61] and fuel cells [46,62-64]. In conjunction with zinc, cadmium, or iron as an anode material, silver oxide can serve as a cathode material in alkaline rechargeable batteries as silver oxide offers an excellent life cycle [61]. In addition, the silver oxide-catalyzed reduction of hydrogen peroxide is of interest for fuel cells in which hydrogen peroxide is used as an oxidant [46].

There have been several reports on the reduction of hydrogen peroxide on silver-based materials [65-68]. Bianchi *et al.* [65] reported that hydrogen peroxide was decomposed into oxygen and hydroxyl ions, and the produced oxygen was then reduced at silver oxide in an alkaline solution. Similar observation was also reported by Iwakura *et al.* [66] whose results showed that hydrogen peroxide reduction involved hydrogen peroxide decomposition followed by oxygen reduction. Another reaction model was proposed by Honda *et al.* [67] who explained that the reduction of H_2O_2 is associated

with the molecular form of hydrogen peroxide (H_2O_2) and the ionic form of hydrogen peroxide (HO_2^-). It was explained that the dissociation of hydrogen peroxide resulted in the coexistence of two different forms of hydrogen peroxide: H_2O_2 and HO_2^-. H_2O_2 dissociation is caused by splitting off a proton from H_2O_2. This reaction is reversible so that both dissociation and recombination occur at the same rate. The reduction of oxygen that was produced by the oxidation of ionic hydrogen peroxide (HO_2^-) can be negligible because the rate of oxygen reduction is much slower than the rate of hydrogen peroxide (H_2O_2) reduction [67]. More recently, Savinova *et al.* [68] also suggested the reaction mechanism of hydrogen peroxide reduction that the rate of hydrogen peroxide reduction was strongly affected by the oxidation state of silver in an alkaline solution.

Although there is a contradiction regarding detailed reaction mechanisms in the literature [65-68], two catalytic reactions are known to be combined in hydrogen peroxide reduction on silver oxide in an alkaline solution. One is the decomposition of hydrogen peroxide into oxygen and water [69]. This reaction is catalyzed by silver and takes place more rapidly in an alkaline solution [70]. The other is the reduction of hydrogen peroxide to water [69]. Several catalysts, such as platinum, palladium, iridium, silver, and a combination of these, were shown to be electroactive for the reduction of hydrogen peroxide. Unfortunately, however, these metals are also known to decompose hydrogen peroxide [71]. Thus, H_2O_2 reduction is accompanied with H_2O_2 decomposition if silver is employed as a catalyst. Depending on the electrons involved, hydrogen peroxide decomposition can be either chemical or electrochemical. In contrast to the electrochemical decomposition of H_2O_2 and the reduction of H_2O_2, the chemical

decomposition of H_2O_2 is almost negligible in electron-consuming reduction reactions because it involves no electron transfer [71].

In addition to the reduction of hydrogen peroxide, the electrochemical reaction of methanol on silver-based materials also needs to be considered as it is probable with the membraneless structure. Although silver has been used as a catalyst for the oxidation of methanol to produce formaldehyde (CH_2O) on a large scale, this process requires high temperatures, usually 600 to 700°C, for high conversion efficiency [72-74]. Such reactions cannot occur at considerable rates in the fuel cell operation at room temperature.

In this work, the electrochemical reaction of hydrogen peroxide on silver oxide is experimentally studied using an electroanalytical method.

3.2 Catalyst Preparation

3.2.1 Nickel Hydroxide as Anode Catalyst

Figure 3.3 illustrates an electroplating system setup for nickel electrodeposition. An ammeter can be also added to monitor the actual supplied current. A nickel plate as an anode and a thin chromium/gold film (200 Å/3000 Å) on a glass substrate as a cathode were immersed in the nickel sulfate-based electrolyte. The composition of the electroplating solution is listed in Table 3.1 [75]. Nickel electroplating was carried out at a pH of 4 at room temperature (22 to 23°C). The current density of 5 mA/cm^2 was applied to the electrode area of 6.45 cm^2 for 20 minutes, resulting in the film thickness of 2 μm.

In order to form nickel hydroxide after electroplating, the electroplated nickel was voltammetry-cycled within the potential range of -1.2 to 0.6 V with respect to a silver/silver chloride (Ag/AgCl) reference electrode in 1 M KOH at a scan rate of 10

mV/s for 80 times [76-77]. After this treatment and between experiments, the nickel hydroxide samples were stored in 1 M KOH to prevent undesired reactions in the air.

Table 3.1. Composition of nickel electroplating solution [75].

Material	Quantity
Nickel Sulfate ($NiSO_4 \cdot 6H_2O$)	200 g/l
Nickel Chloride ($NiCl_2 \cdot 6H_2O$)	5 g/l
Boric Acid (H_3BO_3)	25 g/l
Saccharin ($C_7H_4NO_3S \cdot Na \cdot 2H_2O$)	3 g/l

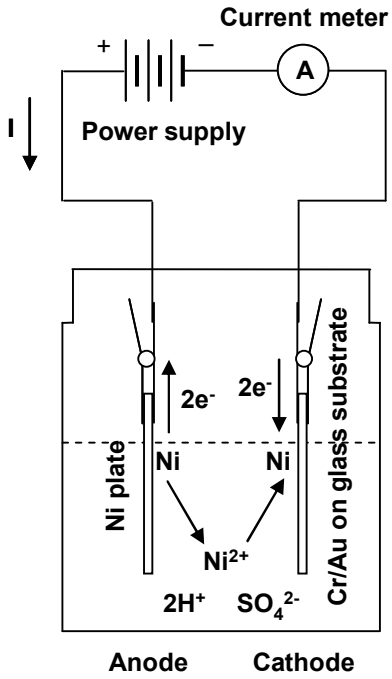

Figure 3.3. Schematic illustration of the electroplating setup for nickel deposition.

3.2.2 Silver Oxide as Cathode Catalyst

Silver was also prepared by electroplating. For silver electroplating, a silver plate as an anode and a thin chromium/gold film (200 Å/3000 Å) on a glass substrate as a cathode were immersed in a commercially available silver electroplating solution (Cy-less Silver, Technic). Silver electroplating was carried out at a pH of 8.5 at room temperature (22 to 23°C). The current density of 3 mA/cm^2 was applied to the electrode area of 6.45 cm^2 for 15 minutes resulting in the film thickness of 2 μm. After electroplating the silver layer, no further treatment was conducted other than immersion of the electroplated silver in 1 M KOH to form silver oxide. The silver oxide samples were also stored in 1 M KOH to prevent undesired reactions.

3.3 Electroanalytical Characterization: Cyclic Voltammetry

Cyclic voltammetry is one of the electroanalytical techniques used in electroanalytical chemistry. In cyclic voltammetry, the voltage is swept in positive and/or negative directions while the current is measured. A cyclic voltammetry experiment may use a full cycle, a partial cycle, or several cycles, depending upon the application [78]. The voltage applied to the electrode makes its surface negatively or positively charged, so that reducible species can receive electrons from the surface or oxidizable species can generate electrons to the surface. During oxidation or reduction, the current is measured at the electrode [79].

The electrochemical properties of the catalysts, nickel hydroxide and silver oxide, were analyzed by cyclic voltammetry. A cyclic voltammetry setup was built using a signal generator, potentiostat, and current-measuring amplifier. The latter two components were made by a fully differential amplifier (THS4141, Texas Instruments)

and a current-to-voltage converter (LM741CN, National Semiconductor). A triangular waveform-based voltage-time function was generated using a Field Point module (FP-AO-210, National Instruments) controlled by LabVIEW (LabVIEW 7 Express, National Instruments). Details on the cyclic voltammetry setup and its system validation study are described in Appendix.

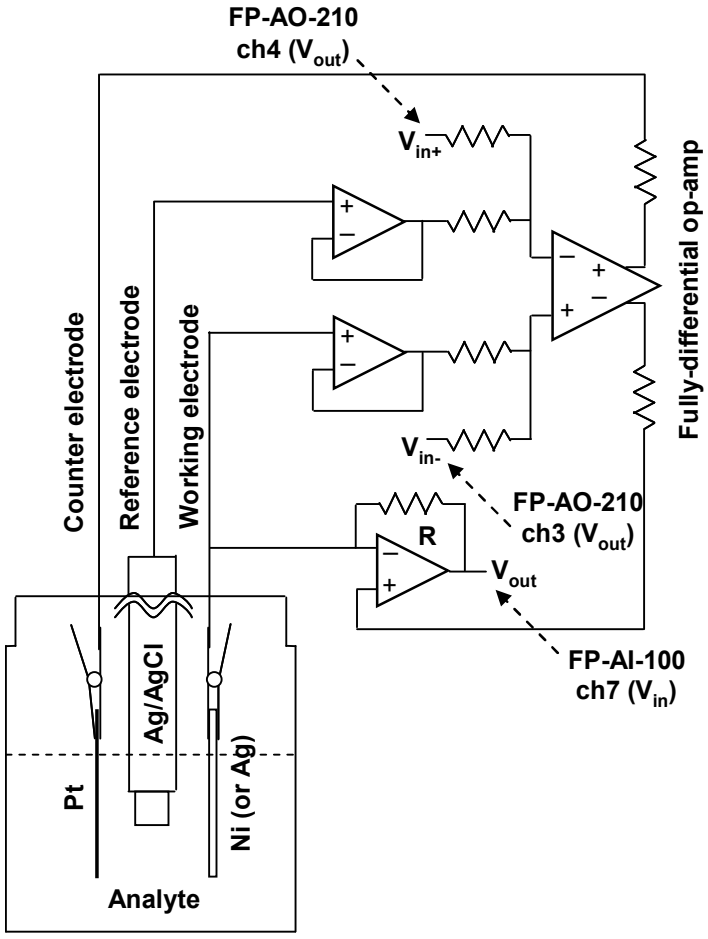

Figure 3.4. Schematic illustration of the experimental apparatus for cyclic voltammetry. The op amp-based potentiostat is connected to the LabVIEW-controlled Field Point modules. The voltage output module (FP-AO-210) was used to apply voltage excitations and the voltage input module (FP-AI-100) was used to read current responses. A more detailed diagram can be found in the Appendix.

The three-electrode cell for cyclic voltammetry is shown in Figure 3.4. The nickel hydroxide or silver oxide electrode (2.54 × 2.54 cm^2) and platinum wire coil were used as working and counter electrodes, respectively. Measured potentials in this work were with respect to an Ag/AgCl (in 3.5 M KCl) reference electrode (WRE5001, Weiss Research).

3.4 Cyclic Voltammetry Results and Discussion

3.4.1 Electrochemical Nickel Hydroxide Formation

In order to form nickel hydroxide, the electroplated nickel was voltammetry-cycled within -1.2 to 0.6 V with respect to a Ag/AgCl reference electrode in 1 M KOH at a scan rate of 10 mV/s for 80 times. Electrochemical nickel hydroxide formation was characterized as shown in Figure 3.5 (a). The anodic current (A_1) was observed at 110 mV (versus Ag/AgCl) that corresponds to the oxidation of nickel to $Ni(OH)_2$ based on the reaction [54]:

$$Ni + 2OH^- \rightarrow Ni(OH)_2 + 2e^-. \quad (3.1)$$

Another anodic current (A_1') at -550 mV (versus Ag/AgCl) was also transiently observed but its origin has not been ascertained. In conjunction with the anodic current (A_1), the cathode current (C_1) appeared at a potential where hydrogen was evolved, which was related to the reduction of $Ni(OH)_2$ to Ni, thus to the reactivation of the catalyst. Besides, the anodic current (A_2) was observed at 540 mV (versus Ag/AgCl), which resulted from the oxidation of $Ni(OH)_2$ to NiOOH. Another cathodic current (C_2) was detected at 340 mV (versus Ag/AgCl) that was caused by the reduction of NiOOH to $Ni(OH)_2$, which can be written as [51,53-54]:

$$Ni(OH)_2 + OH^- \leftrightarrow NiOOH + H_2O + e^- \quad (3.2a)$$

$$Ni(OH)_2 \leftrightarrow NiOOH + H^+ + e^-. \quad (3.2b)$$

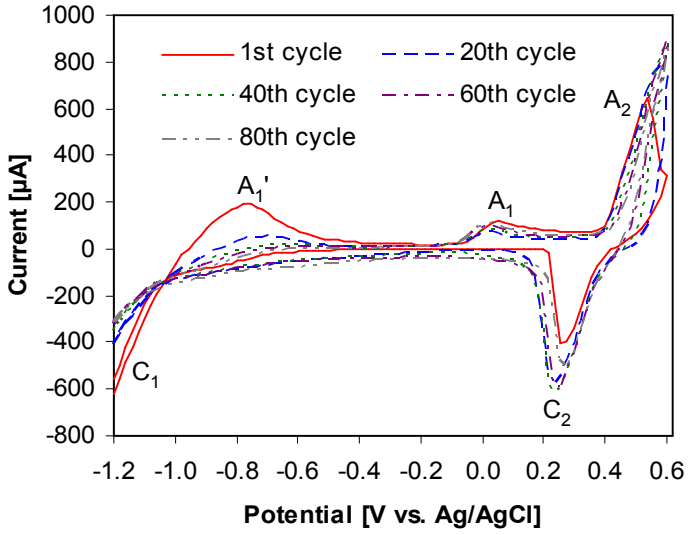

(a)

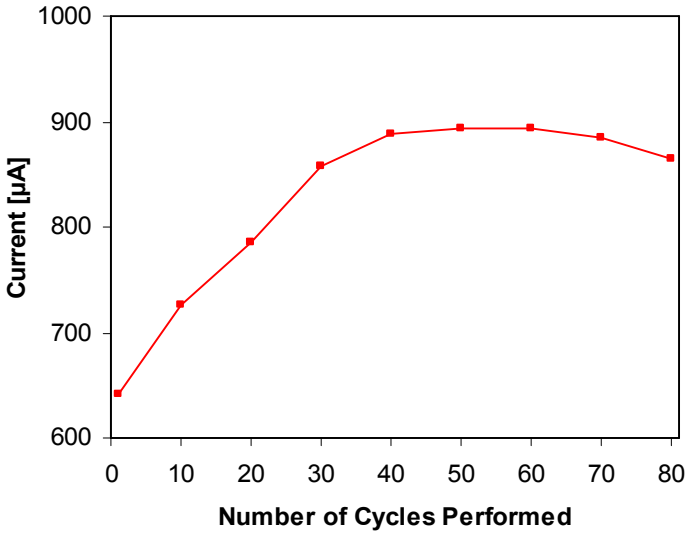

(b)

Figure 3.5. Effect of voltammetry-cycling on nickel hydroxide formation: (a) cyclovoltammograms for nickel oxidation in 1 M KOH and (b) peak current of nickel oxidation (A_2) versus number of voltammetry-cycles performed. Temperature was 22.5°C, electrode area was 6.45 cm^2, scan rate was 10 mV/s, and potential window was -1.2 to 0.6 V (versus Ag/AgCl). The voltammetry-cycling repeated for 80 times.

It should be noted that the anodic current (A_2) is larger than the cathodic current (C_2), which indicates that the amount of NiOOH generated from the oxidation of $Ni(OH)_2$ is greater than the amount of $Ni(OH)_2$ produced from the reduction of NiOOH. As a result, NiOOH can be accumulated. This difference in the redox currents shows quasi-reversibility or irreversibility of transformation between $Ni(OH)_2$ and NiOOH [54].

As the voltammetry-cycling repeated, the anodic current (A_2) representing the oxidation of $Ni(OH)_2$ to NiOOH was gradually increased and eventually reached a saturated value after 40 cycles as shown in Figure 3.5 (b). Such an increase in the oxidation current is believed to be a sign of the continuous formation of nickel hydroxide, particularly for NiOOH.

3.4.2 Electrochemical Reactions on Nickel Hydroxide in Fuel Mixture

3.4.2.1 Catalytic Effect of Nickel Hydroxide on Methanol Oxidation

In order to characterize the catalytic effect of nickel hydroxide on the methanol oxidation reaction, cyclic voltammetry was carried out in 1 M methanol with and without the hydroxyl ions (0.1 M KOH) that were required to maintain the reliability of nickel hydroxide. For this purpose, the Cr/Au/$Ni(OH)_2$ electrode was prepared by nickel electrodeposition followed by electrochemical hydroxide formation as described in section 3.2.1.

As shown in Figure 3.6, in the absence of hydroxyl ions (0 M KOH + 1 M CH_3OH), no significant current was detected. By contrast, in the presence of hydroxyl ions (0.1 M KOH + 1 M CH_3OH), several redox current peaks were observed indicating redox reactions. This implies that hydroxyl ions are required for nickel hydroxide to be electroactive for redox reactions. Considering nickel in 0.1 M KOH + 1 M CH_3OH, the

observed current peaks correspond to the phase transformation of nickel to nickel hydroxide along with the nickel hydroxide-catalyzed methanol oxidation in an alkaline solution. This complication can be elucidated by comparing the cyclovoltammogram in 0.1 M KOH + 1 M CH_3OH to that in 0.1 M KOH. The cyclovoltammogram in 0.1 M KOH + 1 M CH_3OH was different from that in 0.1 M KOH in terms of an evolution of the anodic current (A_2) as well as a disappearance of the cathodic current (C_2). Such

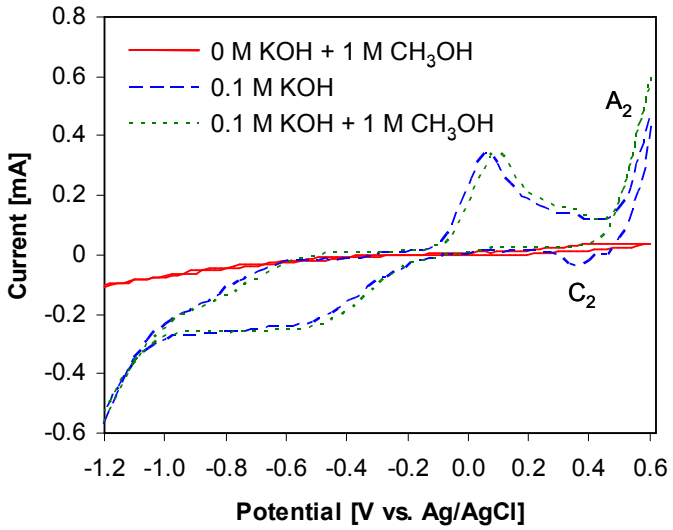

Figure 3.6. Effect of the presence of hydroxyl ions on the catalytic activity of nickel hydroxide. Cyclic voltammetry was performed for the Cr/Au/$Ni(OH)_2$ electrode in 0.1 M KOH + 1 M CH_3OH. Temperature was 22.5°C, electrode area was 6.45 cm^2, scan rate was 10 mV/s, and potential window was -1.2 to 0.6 V (versus Ag/AgCl).

changes were also observed by other researchers [51,54]. Fleischmann *et al.* [51] suggested that the anodic current (A_2) increased due to the overlapping of the currents produced from the oxidation of $Ni(OH)_2$ to NiOOH and the oxidation of methanol, while the cathodic current (C_2) diminished due to the oxidation of methanol along with the reduction of NiOOH to $Ni(OH)_2$:

$$Ni(OH)_2 + OH^- \leftrightarrow NiOOH + H_2O + e^- \qquad (3.2a)$$

$$NiOOH + \text{organic compound} \rightarrow Ni(OH)_2 + \text{intermediate} \quad (3.3)$$

$$\text{intermediate} \rightarrow \text{product} + e^- . \quad (3.4)$$

However, the role of NiOOH as a catalyst for the oxidation of alcohol has been questioned by other researchers [80-81]. Vértes and Horányi [80] observed that the currents produced from the oxidation of $Ni(OH)_2$ to NiOOH and the reduction of NiOOH to $Ni(OH)_2$ remained unchanged, while the anodic current corresponding to the oxidation of alcohol appeared at more positive potentials. Similar observation was also reported by Robertson [81].

3.4.2.2 Catalytic Effect of Nickel Hydroxide on Hydrogen Peroxide Oxidation/ Reduction

In order to analyze the catalytic effect of nickel hydroxide on hydrogen peroxide redox reactions, cyclic voltammetry was also carried out in 0.025 M hydrogen peroxide with and without hydroxyl ions (0.1 M KOH) at the Cr/Au/$Ni(OH)_2$ electrode. The results are shown in Figure 3.7.

Without hydroxyl ions (0 M KOH + 0.025 M H_2O_2), no current was measured. With hydroxyl ions (0.1 M KOH + 0.025 M H_2O_2), an anodic current was observed at potentials more positive than -180 mV (versus Ag/AgCl) presumably indicating the oxidation of hydrogen peroxide. At potentials more negative than -180 mV (versus Ag/AgCl), a cathodic current was observed, probably representing the reduction of hydrogen peroxide. Considering the difference in the observed redox currents, it can be inferred that the oxidation of hydrogen peroxide at nickel hydroxide is more electroactive than the reduction of hydrogen peroxide.

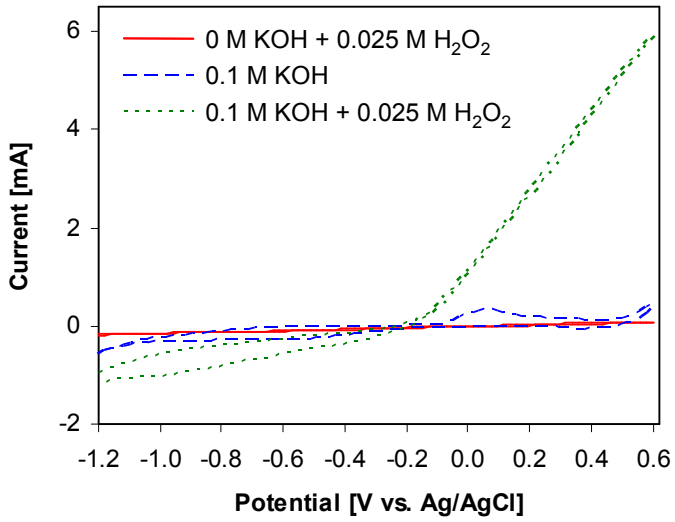

Figure 3.7. Effect of the presence of hydroxyl ions on the catalytic activity of nickel hydroxide. Cyclic voltammetry was performed for the Cr/Au/Ni(OH)$_2$ electrode in 0.1 M KOH + 0.025 M H_2O_2. Temperature was 22.5°C, electrode area was 6.45 cm^2, scan rate was 10 mV/s, and potential window was -1.2 to 0.6 V (versus Ag/AgCl).

3.4.3 Electrochemical Reactions on Silver Oxide in Fuel Mixture

3.4.3.1 Catalytic Effect of Silver Oxide on Hydrogen Peroxide Oxidation/Reduction

The Cr/Au/AgO electrode was prepared by silver electrodeposition followed by chemical oxide formation as described in section 3.2.2. Cyclic voltammetry was carried out in 0.025 M hydrogen peroxide with and without the hydroxyl ions (0.1 M KOH). As shown in Figure 3.8, without hydroxyl ions (0 M KOH + 0.025 M H_2O_2), no current was observed. With hydroxyl ions (0.1 M KOH + 0.025 M H_2O_2), large redox currents were observed and the equilibrium potential was near 40 mV (versus Ag/AgCl). Hydroxyl ions are also required for silver oxide to be electroactive for redox reactions as they are required for nickel hydroxide. Considering silver in 0.1 M KOH + 0.025 M H_2O_2, the observed currents are caused by the formation of silver oxide and the silver oxide-catalyzed hydrogen peroxide redox reactions in an alkaline solution. This complicated

current response can be elucidated by comparing the cyclovoltammogram in 0.1 M KOH + 0.025 M H_2O_2 to that in 0.1 M KOH. In the cyclovoltammogram in 0.1 M KOH, the anodic current (A_1) was detected at 460 mV (versus Ag/AgCl) that arose from the oxidation of Ag to Ag_2O. The cathodic current (C_1) coupled with the anodic current (A_1) was also observed at -25 mV (versus Ag/AgCl), which was caused by the reduction of Ag_2O to Ag. The results obtained are similar to the reactions reported by Iwakura *et al.* and Honda *et al.* [66-67]:

$$2Ag + 2OH^- \leftrightarrow Ag_2O + H_2O + 2e^-. \qquad (3.5)$$

A comparison of the cyclovoltammogram in 0.1 M KOH and that in 0.1 M KOH + 0.025 M H_2O_2 in Figure 3.8 shows an anodic current (A_2) at potentials higher than 40 mV (versus Ag/AgCl) and a cathodic current (C_2) at potentials lower than 40 mV (versus Ag/AgCl). Similar redox currents in the cyclovoltammograms have also been reported

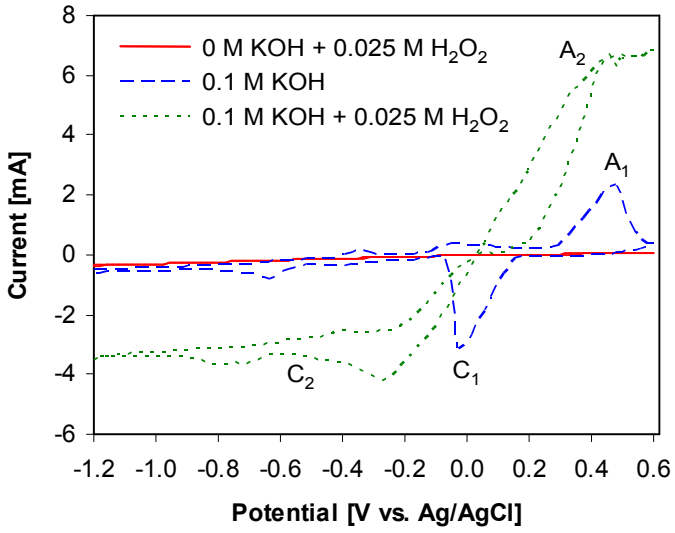

Figure 3.8. Effect of the presence of hydroxyl ions on the catalytic activity of silver oxide. Cyclic voltammetry was performed for the Cr/Au/AgO electrode in 0.1 M KOH + 0.025 M H_2O_2. Temperature was 22.5°C, electrode area was 6.45 cm^2, scan rate was 10 mV/s, and potential window was -1.2 to 0.6 V (versus Ag/AgCl).

by other researchers as a consequence of electrochemical reactions of hydrogen peroxide on silver oxide in the presence of hydroxyl ions [66-67]. Iwakura *et al.* [66] reported a broad cathodic current accompanied with a single peak at potentials lower than 100 mV (versus Hg/HgO) in 1 M KOH + 0.1 M H_2O_2 and explained that the cathodic current was produced from hydrogen peroxide decomposition followed by oxygen reduction. It is known that hydrogen peroxide is decomposed into oxygen and water, and the produced oxygen is then reduced on silver oxide in an alkaline solution:

$$O_2 + H_2O + 2e^- \rightarrow OH^- + HO_2^-. \quad (3.6)$$

Honda *et al.* [67] also showed a cathodic current at potentials lower than 100 mV (versus NHE (normal hydrogen electrode)) in 1 M KOH + 0.0125 M H_2O_2 and explained that the cathodic current was generated from the direct reduction of hydrogen peroxide based on the reaction:

$$H_2O_2 + 2e^- \rightarrow 2OH^-. \quad (3.7)$$

They also suggested that the reduction current was partially caused by the reduction of oxygen as well as the electrochemical decomposition of hydrogen peroxide. A cathodic current resulting from hydrogen peroxide reduction was also found by Savinova *et al.* [68]. In their work, a rotating disk electrode was used as a working electrode.

3.4.3.2 Catalytic Effect of Silver Oxide on Methanol Oxidation

In order to characterize the catalytic effect of silver oxide on methanol oxidation, cyclic voltammetry was carried out in 1 M methanol with and without hydroxyl ions (0.1 M KOH) at the Cr/Au/AgO electrode as shown in Figure 3.9.

No significant current was observed in the absence of hydroxyl ions (0 M KOH + 1 M CH_3OH) as expected. By contrast, several redox currents were observed in the

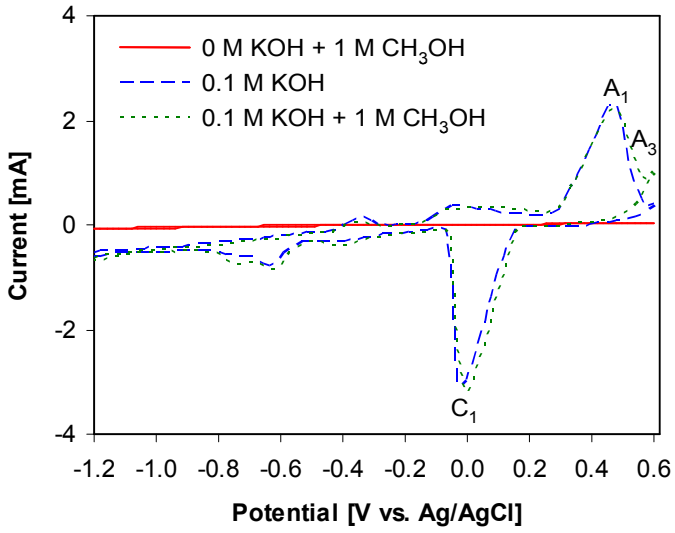

Figure 3.9. Effect of the presence of hydroxyl ions on the catalytic activity of silver oxide. Cyclic voltammetry was performed for the Cr/Au/AgO electrode in 0.1 M KOH + 1 M CH_3OH. Temperature was 22.5°C, electrode area was 6.45 cm^2, scan rate was 10 mV/s, and potential window was -1.2 to 0.6 V (versus Ag/AgCl).

presence of hydroxyl ions (0.1 M KOH + 1 M CH_3OH) implying the redox reactions of hydroxyl ions at the electroactive silver oxide. A comparison of the cyclovoltammogram in 0.1 M KOH and that in 0.1 M KOH + 1 M CH_3OH in Figure 3.9 exhibits an anodic current (A_3) at 600 mV (versus Ag/AgCl). Even though the observed current is inappreciable, it is likely to result from the oxidation of methanol at silver oxide considering silver in 0.1 M KOH + 1 M CH_3OH.

3.5 Conclusions

In this chapter, the redox reactions in the fuel cell using nickel hydroxide and silver oxide as catalysts were electrochemically analyzed using cyclic voltammetry. The role of nickel hydroxide and silver oxide as anode and cathode catalysts were examined for the redox reactions. Prior to electroanalytical experiments, nickel hydroxide on the anode was prepared by nickel electroplating followed by electrochemical hydroxide

formation, while silver oxide on the cathode was prepared by silver electroplating followed by chemical oxide formation. Hydroxyl ions were shown to be essential for both catalysts to be electroactive. According to the cyclic voltammetry results obtained, it can be inferred that in the presence of hydroxyl ions, nickel hydroxide catalyzed methanol by the anodic oxidation and silver oxide catalyzed hydrogen peroxide by the cathodic reduction. However, at the same time, hydrogen peroxide was found to be reactive at nickel hydroxide as well. It is thus believed that in addition to methanol, hydrogen peroxide serves as another reductant for the anodic oxidations in the fuel cell. According to the cyclic voltammetry results obtained, methanol was shown to be slightly reactive at silver oxide but the silver oxide-catalyzed methanol oxidation would be subordinate compared to the silver oxide-catalyzed hydrogen peroxide reduction. The obtained cyclic voltammetry results have shown the feasibility of nickel hydroxide and silver oxide as catalysts for the redox reactions, even though it is still difficult to predict the overall characteristics of the fuel cell depending on such information about only half cells (anode and cathode) because the anodic and cathodic reactions in the fuel cell are electrochemically connected by means of ions and electrons. For this reason, the actual performance of these catalysts will be validated using a fuel cell with a membraneless structure in Chapter 4.

CHAPTER 4. MACROSCALE FUEL CELL

4.1. Introduction

Nickel hydroxide ($Ni(OH)_2$) is electroactive as an anode catalyst for methanol oxidation and silver oxide (AgO) is electroactive as a cathode catalyst for hydrogen peroxide reduction as analyzed using cyclic voltammetry in sections 3.4.2 and 3.4.3 of Chapter 3. Based on the results obtained in the previous chapter, nickel hydroxide and silver oxide are employed as catalysts for the fuel cell in this work. The actual performance of these catalysts is validated by the use of a membraneless macroscale fuel cell. Figure 4.1 shows the fuel cell with a membraneless structure developed in this study. In this chapter, various operational conditions for the fuel cell are investigated including the catalyst surface conditions, fuel mixture composition, and distance effect between anode and cathode.

4.1.1 The Optimal Surface Condition of Catalysts

As briefly discussed in section 3.1.2 of Chapter 3, nickel hydroxide is known to suffer a phase transformation in an alkaline solution, which is related to the degradation of catalytic activity [57]. Stabilizing nickel hydroxide in an alkaline solution is therefore a critical issue that must be addressed before employing nickel hydroxide as a catalyst for a fuel cell. Another challenge in employing nickel hydroxide and silver oxide is their relatively low catalytic activity compared to platinum and/or platinum alloys, which could result in a low extractable output power. Consequently, the optimal surface

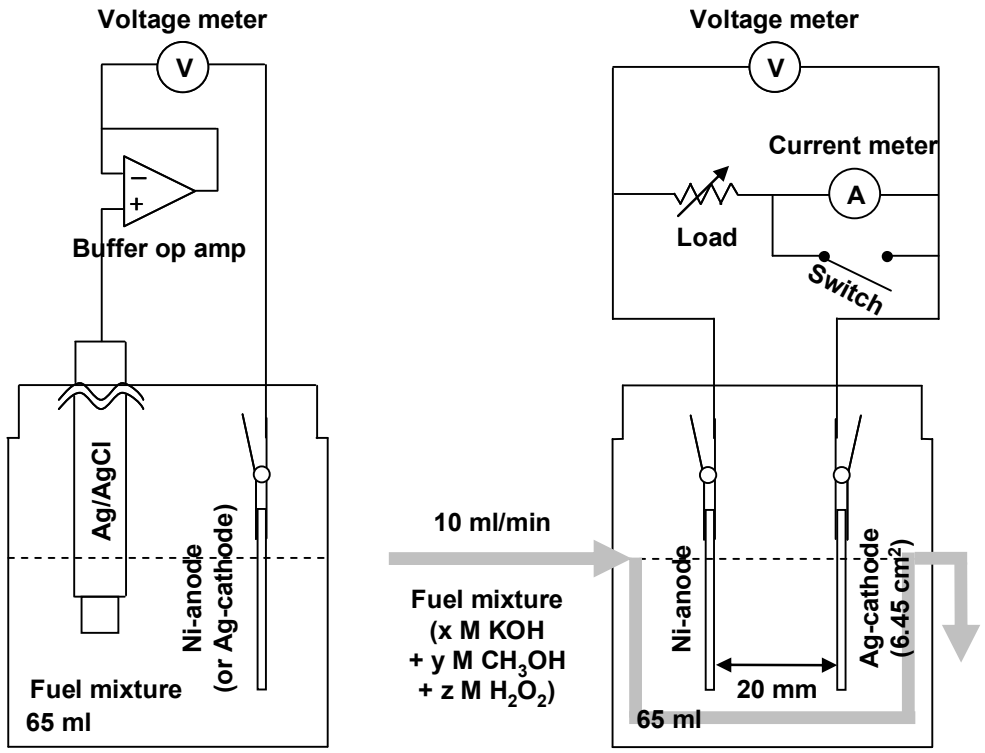

(a) (b)

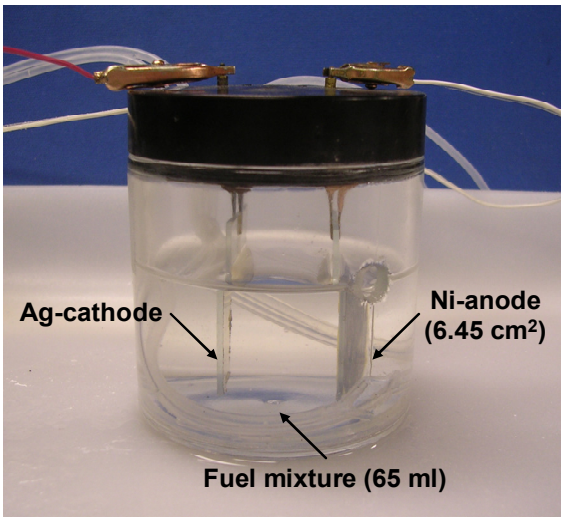

(c)

Figure 4.1. Schematic illustrations of the experimental apparatus: (a) half-cell potential measurement setup; (b) current-voltage measurement setup, and (c) photograph of the current-voltage measurement setup.

condition of nickel hydroxide should be examined to overcome its low and unstable catalytic activity.

4.1.2 The Optimal Composition of Fuel Mixture

As noted in section 2.3.2 of Chapter 2, a mixture of methanol, hydrogen peroxide, and hydroxyl ions is used as fuel in the fuel cell without a proton exchange membrane. The operation of this fuel cell depends on the anodic oxidation of methanol on nickel hydroxide and the cathodic reduction of hydrogen peroxide on silver oxide in the presence of hydroxyl ions. The concentration of these reactants is therefore an important parameter that must be optimized in order to extract the maximum output power. In this work, fuel cell output voltages and currents are measured with various combinations of reactant concentrations and different external loads. The optimal composition of a fuel mixture is decided by considering not only the magnitude but also the stability of the measured fuel cell output. Furthermore, the dependence of a relative amount of reactants and an absolute amount of reactants on the optimal composition of a fuel mixture is experimentally studied.

4.1.3 The Distance Effect on the Fuel Cell Output

The fuel mixture serves as a fuel and, at the same time, it serves as a diffusion path for the reactants involved in the membraneless structure of the fuel cell. A shorter diffusion length is expected to lead to a shorter diffusion time, particularly for a charge carrier moving from anode to cathode, which in turn causes a faster electrochemical reaction and thereby a higher output power. As reviewed in section 2.3.1 of Chapter 2, this causality has been demonstrated with a polymer electrolyte membrane whose thickness defines the distance between anode and cathode [35-36]. In the same sense, the

effect of distance between anode and cathode is investigated with the fuel cell in this work. This study differs from those using a polymer electrolyte membrane [35-36] since an electrolyte is not a solid membrane but a fuel mixture. Besides, fuel crossover is no more a restraining factor for the reduction of the distance between anode and cathode.

4.2 Experimental Setup

4.2.1 Half-Cell Potential Measurement

A typical electrochemical cell including a fuel cell comprises two half cells – anode and cathode. There is a salt bridge or an ion exchange membrane between anode and cathode preventing mixing of their reactants while maintaining their electrical contact. Unless two half cells are electrically shorted, the anode where oxidation occurs always has more electrons than the cathode. In this sense, the anode becomes relatively more negatively charged than the cathode. Electrons are, in turn, flowing from the anode to the cathode while a current flows from the cathode to the anode through an external conductor or a load resistor. The cathode potential is therefore higher than the anode potential, and their difference is a cell voltage. Typically, the only voltage that can be measured is this cell voltage and its change upon varying the load resistance. This overall cell voltage, however, cannot give enough information on each half cell. For this reason, a reference electrode was employed in the fuel cell setup, which enables the independent and direct measurement of half-cell potential [82].

The fuel cell setup for half-cell potential measurement is shown in Figure 4.1 (a). In this study, a commercially available silver/silver chloride (Ag/AgCl) reference electrode in saturated KCl (WRE5001, Weiss research) was used. The reference electrode was placed about 10 mm from the anode and cathode. An operational amplifier

(LM741CN, National Semiconductor) isolated the voltage source, the reference electrode in this experiment, from its measurement circuit, thereby resulting in no current entry to the reference electrode. The half-cell potential versus the reference electrode was measured using a Field Point module (FP-AI-100, National Instruments) and a user interface was created with LabVIEW (LabVIEW 7 Express, National Instruments).

4.2.2 Current-Voltage and Current-Time Measurement

In order to explore the electrical characteristics of the fuel cell, the output voltages and currents were measured with various external loads. For this measurement, the fuel cell setup for half-cell potential measurement was reused with a few modifications, as illustrated in Figure 4.1 (b). The output voltage measurement began in open circuit condition and ended in short circuit condition; between them, the external loads were applied to control the output current in order of 100 kΩ, 10 kΩ, 5.6 kΩ, 2.7 kΩ, 1 kΩ, 560 Ω, 470 Ω, 330 Ω, 150 Ω, 100 Ω, 56 Ω, 27 Ω, and 10 Ω. Maintaining consistency with the half-cell potential measurement, the output voltages and currents were measured using Field Point modules (FP-AI-100 and -110, National Instruments) and a user interface was created with LabVIEW (LabVIEW 7 Express, National Instruments). Additionally, a mechanical switch was employed across the current meter in order to eliminate the effect of the internal resistance of the current meter on the output voltage.

4.3 Macroscale Fuel Cell Test Results

4.3.1 The Effect of Electrode Condition

The effect of electrode conditions on the fuel cell output was experimentally studied to determine the optimal surface condition of the catalysts: nickel hydroxide and silver oxide. Nickel hydroxide at the anode was prepared by nickel electrodeposition

followed by electrochemical hydroxide formation, while silver oxide at the cathode was prepared by silver electrodeposition followed by chemical oxide formation, as described in sections 3.2.1 and 3.2.2 of Chapter 3. Three pairs of electrode samples were prepared and tested.

The fuel mixture used in this experiment was composed of 0.1 M potassium hydroxide, 1 M methanol, and 0.025 M hydrogen peroxide. In order to maintain the concentration of these reactants during the measurement, the fuel mixture was replenished at a rate of 10 ml/min using a syringe pump.

The catalysts in the fuel cell were characterized by observing fuel cell output voltages and currents in the following order. First, the anode and cathode potentials were measured (versus Ag/AgCl) in the fuel mixture. At this point, the current-voltage measurement could be unreliable because the catalysts were unstable due to the phase transformation of nickel hydroxide in an alkaline solution as stated in section 3.1.2 of Chapter 3. So, the output current was measured with a load resistance of 100 Ω until the current became stable. After the output current was stabilized, the anode and cathode potentials were measured again (versus Ag/AgCl), and subsequently, the output voltage and current were measured with various external loads.

As shown in Figure 4.2, the output current continuously decreased for 5 to 6 hours, and then settled at stabilized values. It is believed that the observed decline in the output current was caused by the aging effect of nickel hydroxide at the anode [56]. It was reported that the phase transformation of nickel hydroxide in an alkaline solution caused the degradation of electrochemical properties [57]. As shown in Figure 4.3, the fuel cell with the stabilized catalysts delivered an open circuit voltage of 123.9 mV, a short circuit

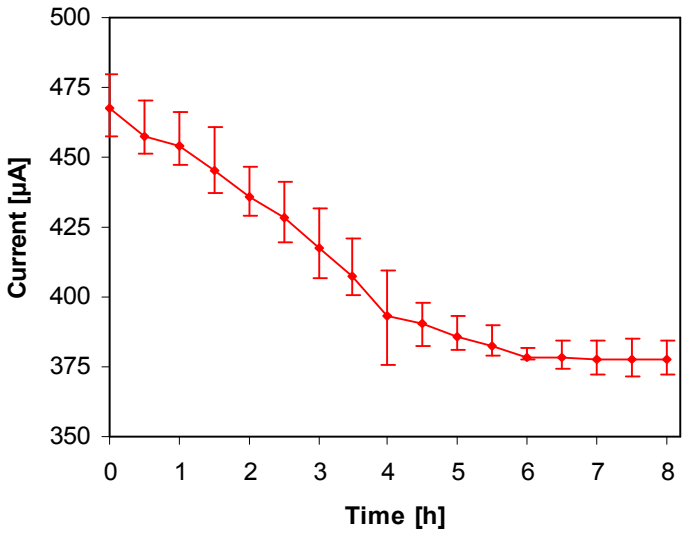

Figure 4.2. Aging effect of the anode catalyst (nickel hydroxide) on the fuel cell output current. The cathode catalyst was silver oxide. The output current was measured with a 100 Ω load resistance for 8 hours. Three pairs of electrode samples (6.45 cm^2) were tested. Three sets of the output current were averaged and then plotted with an error bar. The fuel mixture of 0.1 M KOH + 1 M CH_3OH + 0.025 M H_2O_2 (65 ml) was supplied at a rate of 10 ml/min. Distance between anode and cathode was 20 mm and temperature was 22.5°C.

current of 607.43 μA, and a maximum output power of 23.84 μW. As shown in Table 4.1, the measured potential of the stabilized nickel hydroxide electrode (-149 mV versus Ag/AgCl) remained unchanged even after testing the fuel cell with a 100 Ω load resistance for 8 hours.

Silver oxide at the cathode was demonstrated to be relatively stable with a few evidences. As shown in Table 4.1, the measured potential of the chemically formed silver oxide electrode (-25 mV versus Ag/AgCl) remained unvaried during fuel cell operation. Also, it was observed that the fuel cell output current was stabilized as long as nickel hydroxide at the anode became stable regardless of the condition of silver oxide at the cathode.

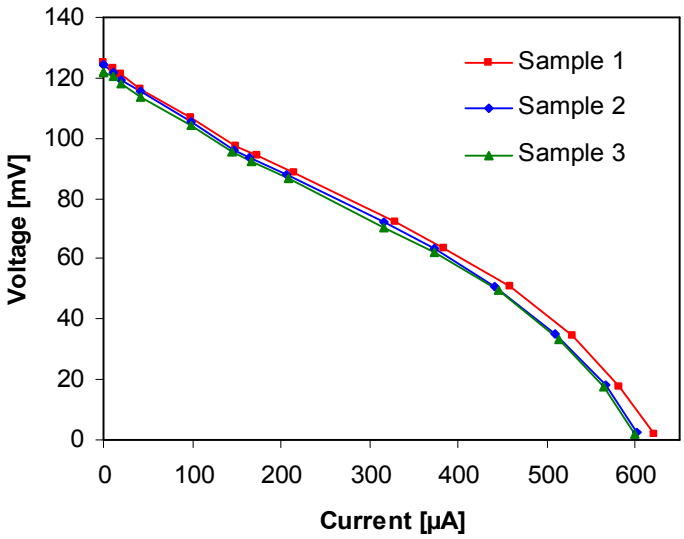

(a)

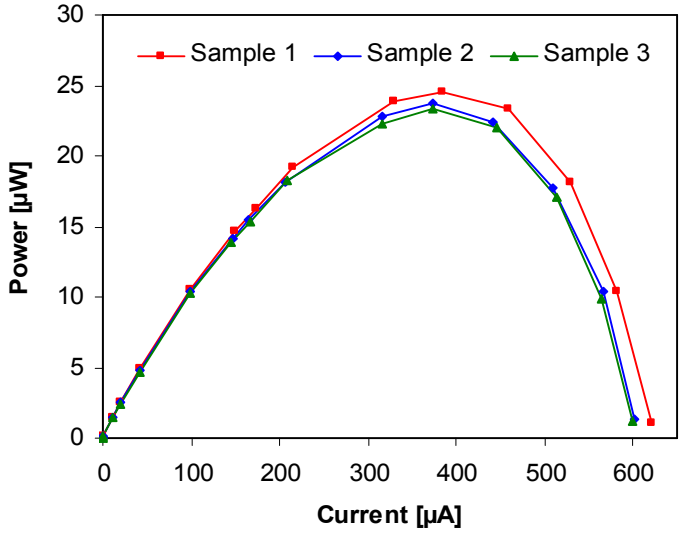

(b)

Figure 4.3. Experimental results of the fuel cell using nickel hydroxide and silver oxide as catalysts: (a) the output voltage versus the output current and (b) the output power versus the output current. The output voltage and current were measured with various external loads. Three pairs of electrode samples (6.45 cm^2) were tested. The fuel mixture of 0.1 M KOH + 1 M CH_3OH + 0.025 M H_2O_2 (65 ml) was supplied at a rate of 10 ml/min. Distance between anode and cathode was 20 mm and temperature was 22.5°C.

Table 4.1. Variation of anode, cathode, and cell potentials during fuel cell operation. Half-cell potentials were measured with respect to a Ag/AgCl reference electrode. Three pairs of electrode samples (6.45 cm^2) were tested. The fuel mixture of 0.1 M KOH + 1 M CH_3OH + 0.025 M H_2O_2 (65 ml) was used. The anode catalyst was nickel hydroxide and the cathode catalyst was silver oxide. Temperature was 22.5°C.

		Sample 1	Sample 2	Sample 3
Potentials (mV) "before" fuel cell operation	Anode	-151	-150	-148
	Cathode	-27	-24	-24
	Cell	124	125	124
Potentials (mV) "after" fuel cell operation	Anode	-151	-149	-147
	Cathode	-26	-24	-25
	Cell	125	125	122

Nickel hydroxide at the anode was stabilized through the long-term fuel cell operation in conjunction with silver oxide at the cathode. As a result, nickel hydroxide and silver oxide were chosen as the anode and cathode catalysts of the fuel cell in this study.

4.3.2 The Effect of Fuel Mixture Composition

The effect of reactant concentration on the fuel cell output was also experimentally studied to determine the optimal composition of a fuel mixture. Seventy two combinations of reactant concentration were applied: six KOH concentrations were applied as 0.01, 0.02, 0.05, 0.1, 0.2, and 0.5 M; four CH_3OH concentrations were applied as 0, 0.5, 1, and 2 M; and three H_2O_2 concentrations were applied as 0.01, 0.025, and 0.05 M. The possible combinations including either 0 M KOH or 0 M H_2O_2 were not applied because the fuel cell output could not be stable without such reactants.

The fuel cell in this experiment was composed of the electrochemically formed nickel hydroxide as an anode catalyst and the chemically formed silver oxide as a cathode catalyst.

4.3.2.1 Half-Cell Potential Measurement

The concentration of hydroxyl ions plays an important role in the oxidation of nickel and silver, which leads to nickel hydroxide and silver oxide, respectively. The electrons released from the oxidation of nickel develop the anode potential while the electrons generated from the oxidation of silver develop the cathode potential, excluding minor influences from the other reactants. The difference at the open circuit condition is called an open circuit voltage (OCV).

In this respect, the potential at the anode and cathode was measured (versus Ag/AgCl) for different OH^- concentrations. The measured anode and cathode potentials (versus Ag/AgCl) are shown in Figure 4.4. For both anode and cathode, the potential decreased as OH^- concentration increased. More hydroxyl ions can produce more electrons and hence develop a greater potential (versus Ag/AgCl), which is consistent with the nickel oxidation reaction at the anode [51,54]

$$Ni + 2OH^- \rightarrow Ni(OH)_2 + 2e^- \quad (4.1)$$

$$Ni(OH)_2 + OH^- \rightarrow NiOOH + H_2O + e^- \quad (4.2)$$

and the silver oxidation reaction at the cathode [66-67]

$$2Ag + 2OH^- \rightarrow Ag_2O + H_2O + 2e^-. \quad (4.3)$$

The dependence of the anode and cathode potential on OH^- concentration became weak for OH^- concentrations higher than 0.2 M.

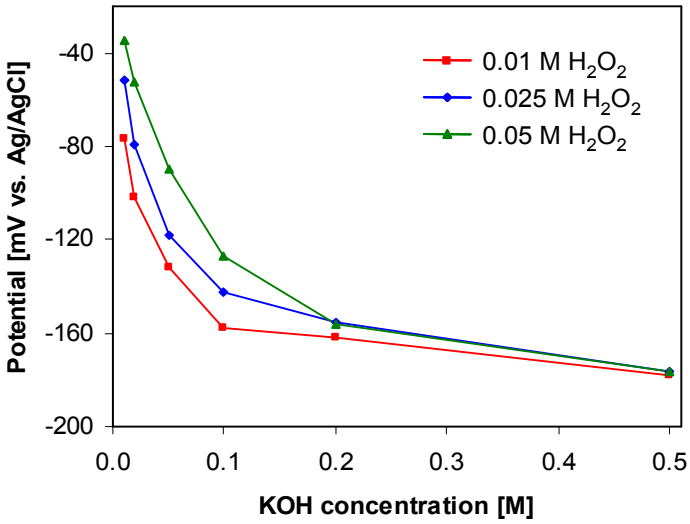

(a)

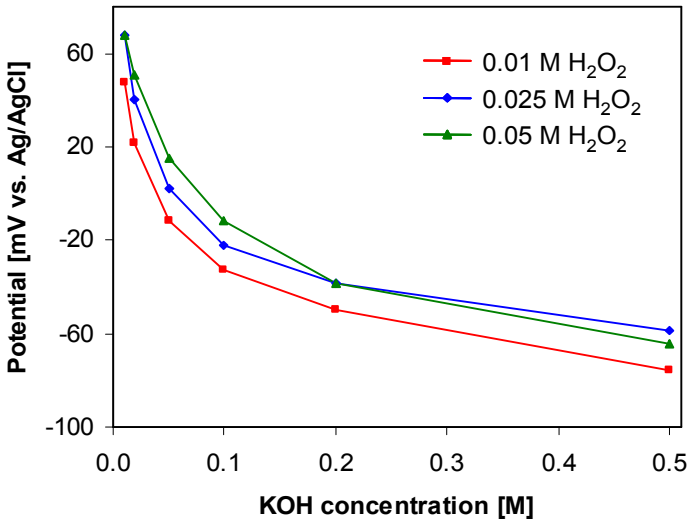

(b)

Figure 4.4. Effect of KOH and H_2O_2 concentrations: (a) half-cell potential at the anode and (b) half-cell potential at the cathode. CH_3OH concentration was fixed to 1 M. Half-cell potentials were measured with respect to a Ag/AgCl reference electrode. The anode catalyst was nickel hydroxide and the cathode catalyst was silver oxide. Temperature was 22.5°C.

The effect of H_2O_2 concentrations on the half-cell potential at the anode and cathode is also shown in Figure 4.4. For both anode and cathode, the potential increased as H_2O_2 concentration increased, which indicates that hydrogen peroxide led to undesirable reduction reactions (electron-consuming) even at the anode. Thus, for both electrodes, more hydrogen peroxide can lead to a faster hydrogen peroxide reduction reaction, which in turn consumes more electrons and hence develops a smaller potential (versus Ag/AgCl). However, similar to OH^- concentration dependence, H_2O_2 concentration dependence of the half-cell potential of anode and cathode became less sensitive for OH^- concentrations higher than 0.2 M.

Subsequently, CH_3OH concentration dependence of the anode and cathode potentials was also investigated in the same manner. At the anode, the half-cell potential decreased as the CH_3OH concentration increased, as shown in Figure 4.5. More methanol can generate more electrons because methanol is oxidized on nickel hydroxide, thereby resulting in a higher potential (versus Ag/AgCl). By contrast, at the cathode, the half-cell potential was almost insensitive to CH_3OH concentration for the OH^- concentrations considered.

4.3.2.2 Current-Voltage Measurement

To determine the optimal composition of a fuel mixture, the current-voltage measurement was carried out with different external loads. The obtained maximum output powers with respect to the applied combinations of reactant concentration are presented in the form of a table (Table 4.2) and a graph (Figure 4.6). As shown in these charts, as the amount of reactants increased in the ratio of 1 : 4 : 40 (H_2O_2 : KOH : CH_3OH), the maximum output power increased. The highest output power (32.39 μW)

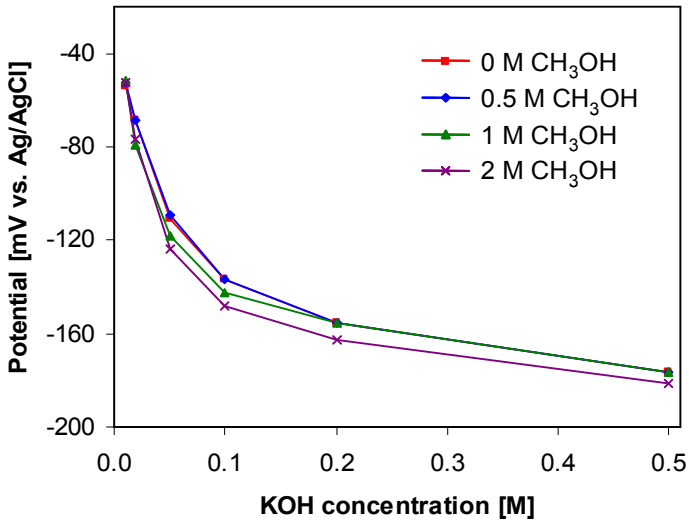

(a)

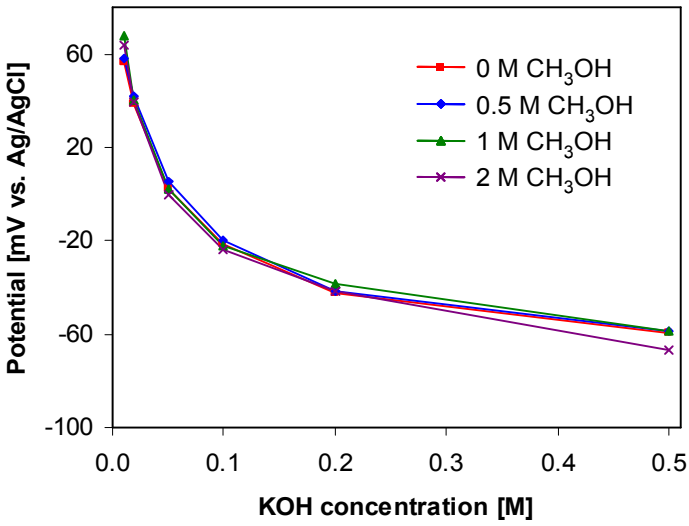

(b)

Figure 4.5. Effect of KOH and CH_3OH concentrations: (a) half-cell potential at the anode and (b) half-cell potential at the cathode. H_2O_2 concentration was fixed to 0.025 M. Half-cell potentials were measured with respect to a Ag/AgCl reference electrode. The anode catalyst was nickel hydroxide and the cathode catalyst was silver oxide. Temperature was 22.5°C.

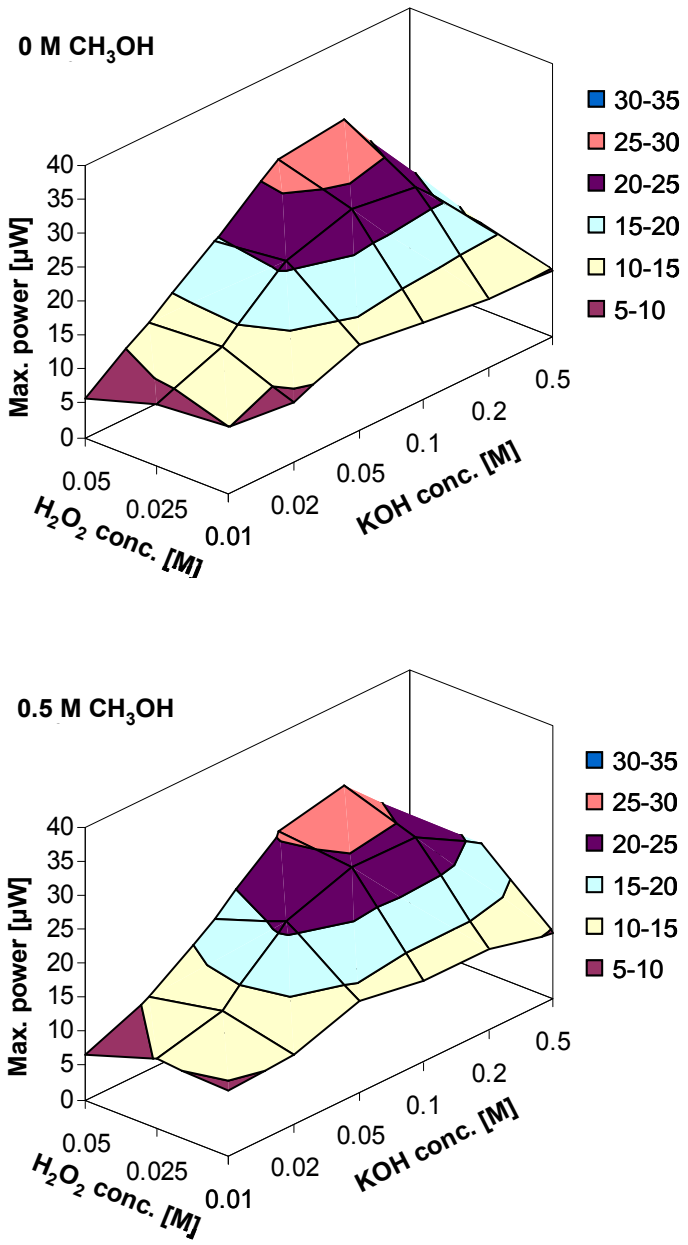

Figure 4.6. Effect of various combinations of reactant concentrations on the maximum output power. The output voltage and current were measured with various external loads. The anode catalyst was nickel hydroxide and the cathode catalyst was silver oxide (6.45 cm^2). The fuel mixture of 0.1 M KOH + 1 M CH_3OH + 0.025 M H_2O_2 (65 ml) was supplied at a rate of 10 ml/min. Distance between anode and cathode was 20 mm and temperature was 22.5°C.

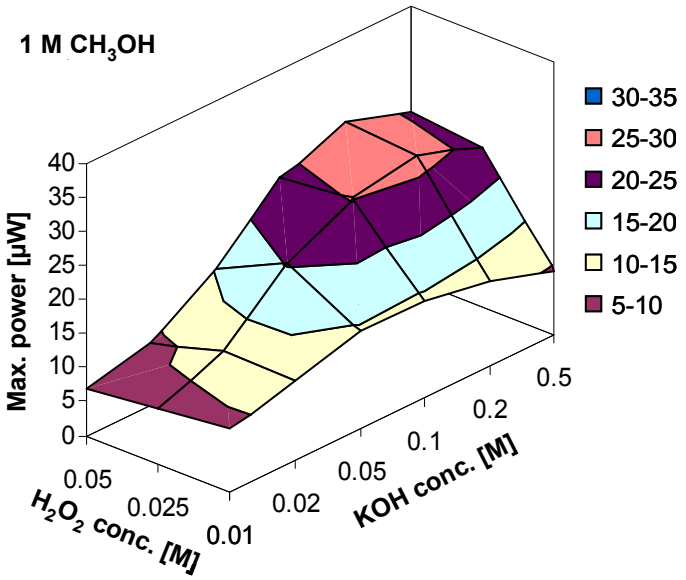
1 M CH3OH
Max. power [µW]
40
35
30
25
20
15
10
5
0
0.05
0.025
0.01
H2O2 conc. [M]
0.02
0.05
0.1
0.2
0.5
KOH conc. [M]
30-35
25-30
20-25
15-20
10-15
5-10

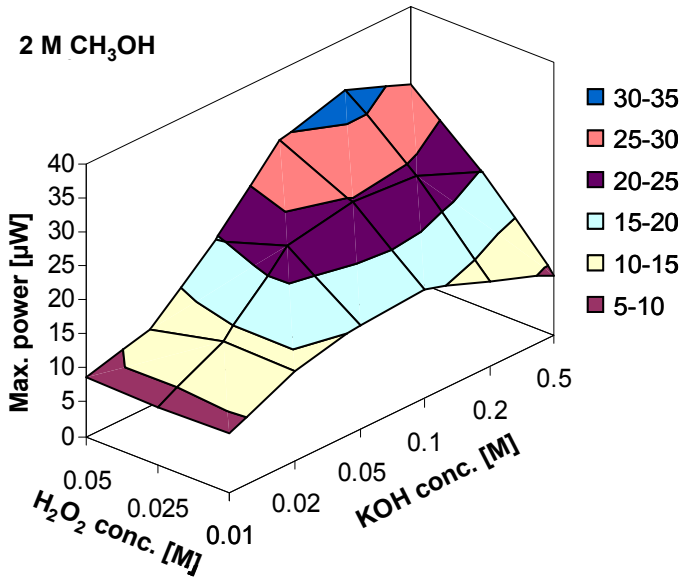
2 M CH3OH
Max. power [µW]
40
35
30
25
20
15
10
5
0
0.05
0.025
0.01
H2O2 conc. [M]
0.02
0.05
0.1
0.2
0.5
KOH conc. [M]
30-35
25-30
20-25
15-20
10-15
5-10

(Fig. cont'd)

was achieved with the fuel mixture of 0.2 M hydroxyl ions, 2 M methanol, and 0.05 M hydrogen peroxide. Consequently, a relative amount of reactants was found to be a more critical issue than their absolute amount.

For a fixed ratio of 1 : 4 : 40 (H_2O_2 : KOH : CH_3OH), however, an absolute amount of reactants also had an effect on the maximum output power as shown in Figure 4.7. The maximum output power increased as the amount of reactants increased, maintaining the fuel mixture ratio of 1 : 4 : 40 (H_2O_2 : KOH : CH_3OH). However, this

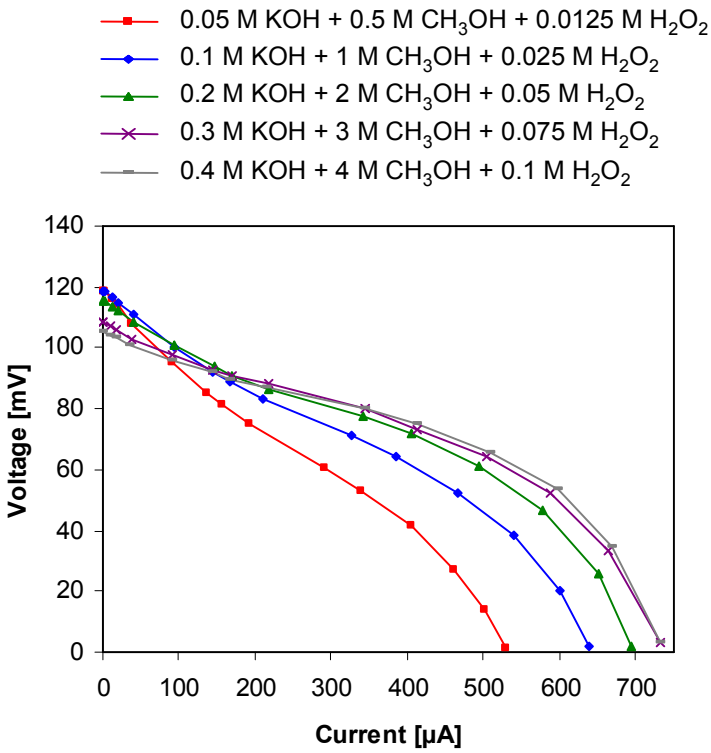

(a)

Figure 4.7. Effect of an absolute amount of reactants on the fuel cell output: (a) the output voltage versus the output current; (b) the output power versus the output current, and (c) the maximum output power versus combination of reactant concentration under the ratio of 1 : 4 : 40 (H_2O_2 : KOH : CH_3OH). The output voltage and current were measured with various external loads. The anode catalyst was nickel hydroxide and the cathode catalyst was silver oxide (6.45 cm^2). The fuel mixture of 0.1 M KOH + 1 M CH_3OH + 0.025 M H_2O_2 (65 ml) was supplied at a rate of 10 ml/min. Distance between anode and cathode was 20 mm and temperature was 22.5°C.

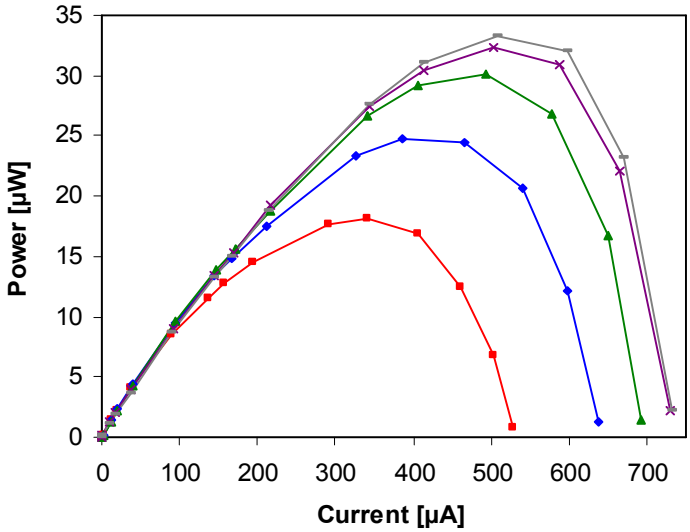
Power [µW]
Current [µA]
0
5
10
15
20
25
30
35
0
100
200
300
400
500
600
700

(b)

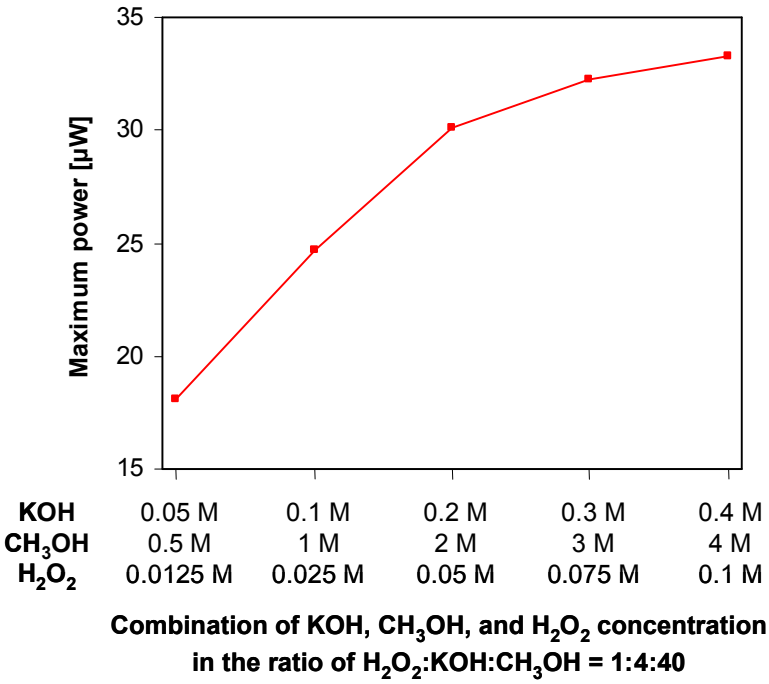
Maximum power [µW]
15
20
25
30
35
KOH
CH3OH
H2O2
0.05 M
0.5 M
0.0125 M
0.1 M
1 M
0.025 M
0.2 M
2 M
0.05 M
0.3 M
3 M
0.075 M
0.4 M
4 M
0.1 M
Combination of KOH, CH3OH, and H2O2 concentration
in the ratio of H2O2:KOH:CH3OH = 1:4:40

(c)

(Fig. cont'd)

dependence became weak for CH_3OH concentrations larger than 2 M. The 3 and 4 M CH_3OH-based fuel mixtures underwent relatively unstable output currents and showed a longer transient time compared to the 2 M CH_3OH-based fuel mixture as shown in Figure 4.8. Furthermore, the 4 M CH_3OH based fuel mixture was shown to suffer a discoloration problem on the surface of the silver oxide probably due to high H_2O_2 concentration (0.1 M). Considering the magnitude and stability of the fuel cell output, the optimal composition of a fuel mixture was determined to be 0.2 M KOH + 2 M CH_3OH + 0.05 M H_2O_2.

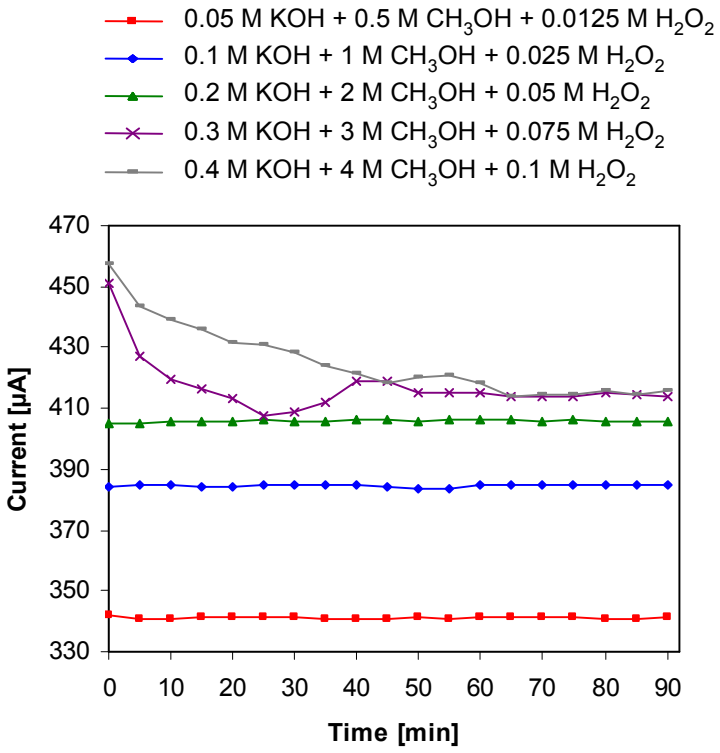

Figure 4.8. Effect of an absolute amount of reactants on the stability of the fuel cell output current. A relative amount of reactants was in the ratio of 1 : 4 : 40 (H_2O_2 : KOH : CH_3OH). The output current was measured with a 100 Ω load resistance for 1.5 hours. The anode catalyst was nickel hydroxide and the cathode catalyst was silver oxide (6.45 cm^2). The fuel mixture of 0.1 M KOH + 1 M CH_3OH + 0.025 M H_2O_2 (65 ml) was supplied at a rate of 10 ml/min. Distance between anode and cathode was 20 mm and temperature was 22.5°C.

Table 4.2. Variation of the maximum output power (μW) extractable from the membraneless macroscale fuel cell with respect to the combinations of reactant concentrations. Test conditions are detailed in Figure 4.6.

CH_3OH [M] = 0	KOH [M]					
H_2O_2 [M]	0.01	0.02	0.05	0.1	0.2	0.5
0.01	10.02	8.86	12.7	11.4	10.28	9.82
0.025	8.9	12.92	20.91	23.7	22.51	12.55
0.05	5.87	12.36	19.63	26.99	28.16	6
CH_3OH [M] = 0.5	KOH [M]					
H_2O_2 [M]	0.01	0.02	0.05	0.1	0.2	0.5
0.01	9.63	10.28	13.48	11.91	11.9	9.59
0.025	10.2	12.52	21.11	24.54	24.05	18.71
0.05	6.5	10.53	17.19	25.45	27.52	11.56
CH_3OH [M] = 1	KOH [M]					
H_2O_2 [M]	0.01	0.02	0.05	0.1	0.2	0.5
0.01	9.25	11.65	14.42	14.14	12.42	9.36
0.025	8.13	11.9	20.28	25.19	26.95	23.43
0.05	6.95	8.95	15.12	24.04	27.58	24.43
CH_3OH [M] = 2	KOH [M]					
H_2O_2 [M]	0.01	0.02	0.05	0.1	0.2	0.5
0.01	8.88	13.38	15.37	16.09	12.69	8.92
0.025	8.57	13.47	22.8	24.67	23.84	19.79
0.05	8.6	11.03	19.51	29.54	32.39	28.62
H_2O_2 [M] = 0.05	KOH [M]					
CH_3OH [M]	0.01	0.02	0.05	0.1	0.2	0.5
3	N/A			26.26	31.55	28.86
4				22.92	31.5	28.97

4.3.3 The Effect of Distance between Anode and Cathode

The effect of distance between anode and cathode on the fuel cell output was experimentally studied to ascertain the potential benefit from a reduced diffusion length of reacting species moving between anode and cathode. The distance between anode and cathode was set from 1 mm to 100 mm.

The fuel mixture of 0.2 M KOH + 2 M CH_3OH + 0.05 M H_2O_2 was supplied at a rate of 10 ml/min during the experiment using a syringe pump as shown in Figure 4.9.

The output voltage and the output power with respect to the output current at various load resistances were measured for different distances between anode and cathode as shown in Figures 4.10 (a) and 4.10 (b). As the distance between anode and

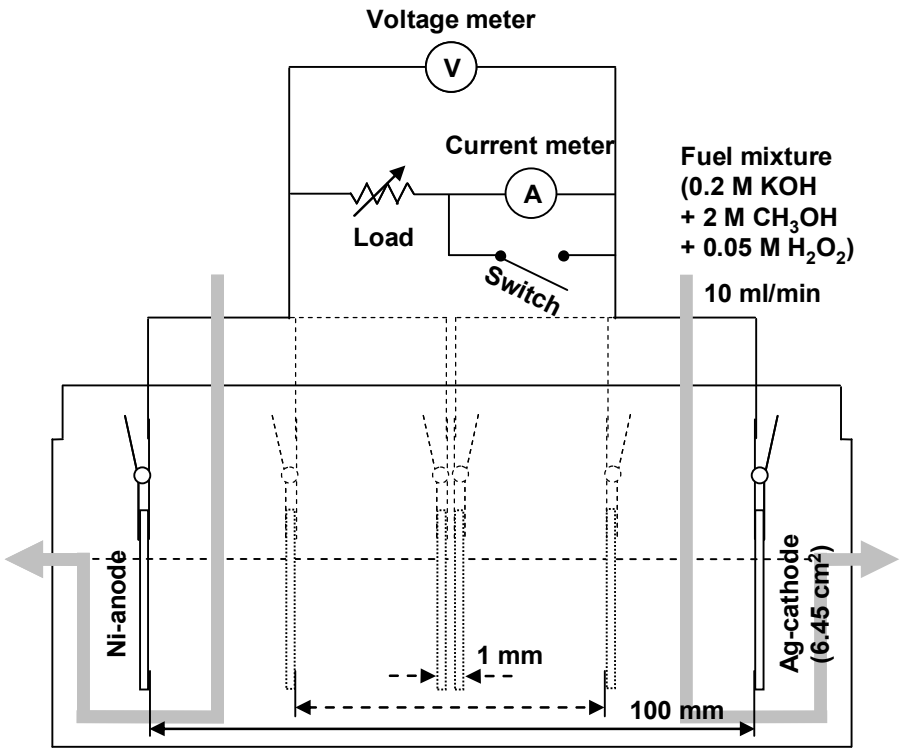

Figure 4.9. Schematic illustration of the experimental apparatus for testing the effect of distance between anode and cathode on the fuel cell output.

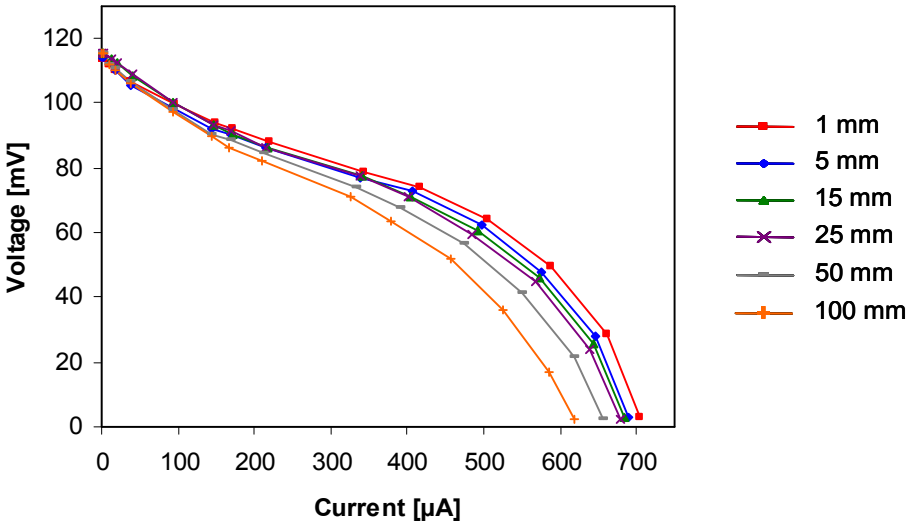

(a)

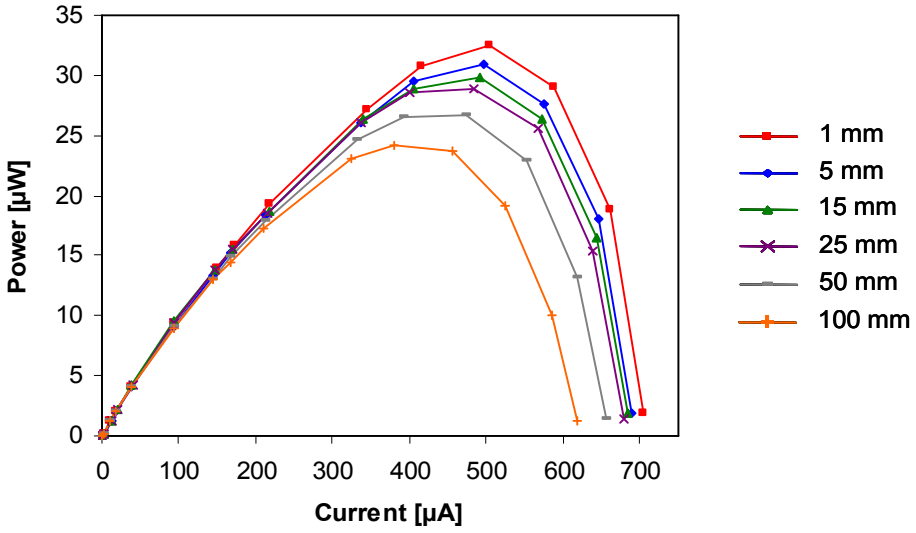

(b)

Figure 4.10. Effect of the distance between anode and cathode on the fuel cell output: (a) the output voltage versus the output current; (b) the output power versus the output current, and (c) the maximum output power versus distance between anode and cathode. The output voltage and current were measured with various external loads. The anode catalyst was nickel hydroxide and the cathode catalyst was silver oxide (6.45 cm^2). The fuel mixture of 0.1 M KOH + 1 M CH_3OH + 0.025 M H_2O_2 (65 ml) was supplied at a rate of 10 ml/min. Distance between anode and cathode was 20 mm.

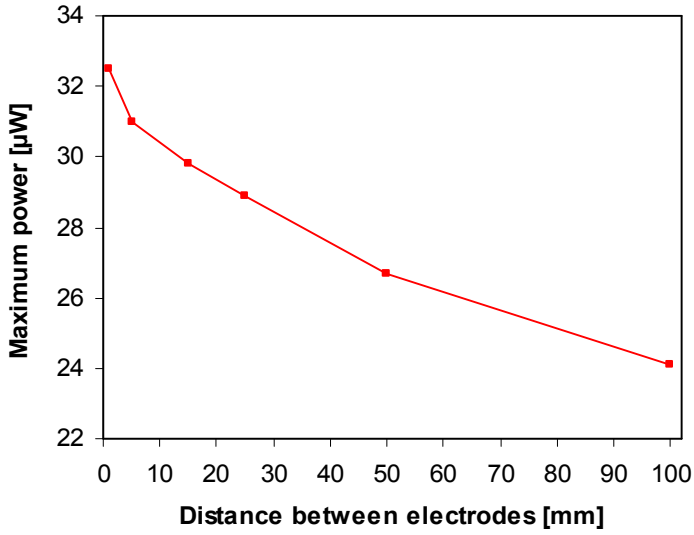

(c)

(Fig cont'd)

cathode decreased, the maximum output power increased (Figure 4.10 (c)). Considering the role of a charge carrier, a shorter diffusion length is believed to give a faster electrochemical reaction because the diffusion time of reacting species would be shorter. Therefore, more reactions can take place at a given time, which increases the total number of charges involving the electrochemical reactions at the anode and cathode.

4.4 Conclusions

This chapter addressed important issues regarding the feasibility of the fuel cell using nickel hydroxide and silver oxide as catalysts. Such non-noble catalysts were introduced to minimize cross reactions with the membraneless structure of the fuel cell studied in this work. The catalytic activity of nickel hydroxide and silver oxide for redox reactions was examined through cyclic voltammetry. In this chapter, the actual

performance of the catalysts was validated through fuel cell operation. Nickel hydroxide at the anode was stabilized through the long-term fuel cell operation. Using the stabilized catalysts in the fuel cell, the fuel mixture composition was optimized by applying different fuel mixture compositions. Considering both the magnitude and stability of the fuel cell output power, the fuel mixture of 0.2 M hydroxyl ions, 2 M methanol, and 0.05 M hydrogen peroxide was chosen as the optimal fuel mixture composition. The effect of distance between anode and cathode on the fuel cell output was also investigated. It was demonstrated that a shorter distance between anode and cathode gives a higher output power. This finding provided good evidence of the presence of a charge carrier moving between anode and cathode in the fuel mixture to complete redox reactions of the fuel cell.

CHAPTER 5. MICROSCALE FUEL CELL

5.1 Introduction

It was obvious that the higher the output power achieved with the shorter the distance between anode and cathode, as demonstrated in section 4.3.3 of Chapter 4. This can be explained that there is a charge carrier between anode and cathode. The transport time of reacting species is shorter as the distance between electrodes is narrower so that the electrochemical reaction rate increases. In this chapter, in order to further extend the distance effect the microscale fuel cell is developed, which enables microscale diffusion lengths of reacting species. Four different designs of the microscale fuel cell are prepared to examine the distance effect between anode and cathode on the fuel cell output (section 5.3.2). In addition, the microfluidic behavior of the microscale fuel cell is also characterized under different fuel flow rates (section 5.3.3).

5.2 Design and Fabrication

5.2.1 Design Considerations

The microscale fuel cell developed in this work is based on a planar and membraneless structure. Thus, electrodes can be arranged on the same plane without a proton exchange membrane, so that the fuel cell dimensions can be flexibly adjusted to meet specific design needs. For the planar configuration, interdigitated microelectrodes were employed as the anode and cathode as illustrated in Figure 5.1. Spacing between anodes and cathodes was determined by photolithography. Four different distances

between anode and cathode, 10, 20, 50, and 100 μm, were prepared and tested for comparison. In each design, the anode and cathode area was unchanged to 1.35 mm^2.

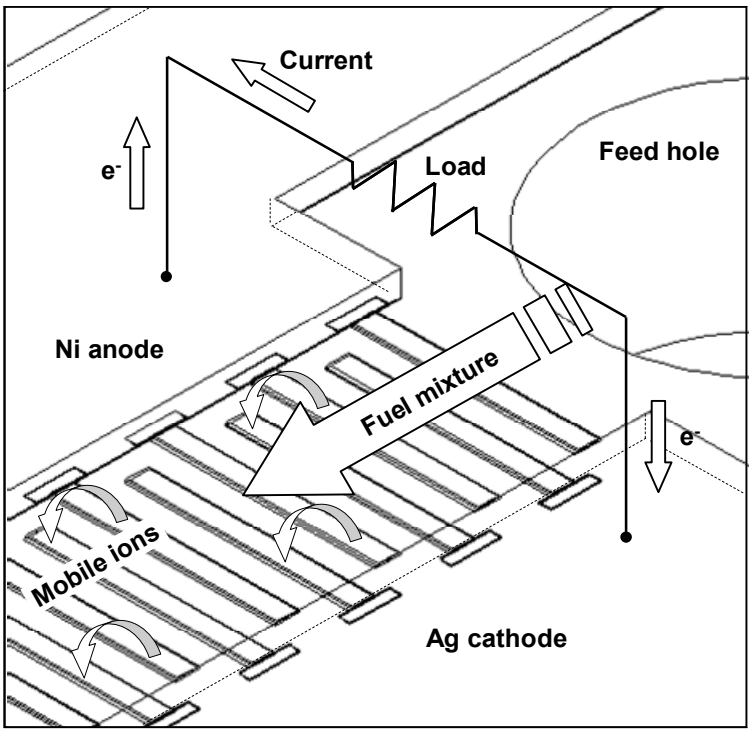

Figure 5.1. Schematic illustration of interdigitated microelectrodes design in the membraneless microscale fuel cell.

5.2.2 Fabrication of Microscale Fuel Cells

The microscale fuel cells were fabricated on a soda-lime microscope slide glass (75 × 25 × 1 mm^3, VWR). The glass substrate was first carefully cleaned in a piranha etching solution of 70 vol. % sulfuric acid to 30 vol. % hydrogen peroxide for 30 minutes. The cleaned glass substrate was then rinsed with deionized (DI) water and dried at 200°C for 10 minutes on a hotplate. The dried glass substrate was first coated with 200 Å of chromium followed by 3000 Å of gold using a Temescal BJD-1800 e-beam deposition system (Center for Advanced Microstructures and Devices (CAMD), Baton Rouge, LA).

The chromium/gold film later served as a seed layer of the electroplated nickel and silver for the anode and cathode, respectively. On the metallized glass substrate, a positive photoresist (Microposit S1813, Shipley) was spin-coated at 3000 rpm for 30 seconds and the substrate was soft-baked at 90°C for 4 minutes on a hotplate. The substrate was then exposed using a Quintel UL7000-OBS aligner (CAMD) at a wavelength of 365 nm, in hard contact mode. Exposure dose was on the order of 38 mJ/cm^2. After exposure, the exposed areas were developed by a 45 seconds immersion in a developing bath (Microposit Developer 354, Shipley) and then rinsed using DI water. After hard-baking at 110°C for 1 minute on a hotplate, etching was carried out. The gold layer (3000 Å) was first etched in a gold etchant (GE-8110, Transene) for 40 seconds, and the chromium layer (200 Å) was then etched in a chromium etchant (Cr-7, Cyantek) for 25 seconds. On the patterned chromium/gold layer, the anode and cathode were selectively formed by electroplating nickel and silver, respectively. Each electroplating condition was consistent with that applied to the macroscale fuel cell, as described in sections 3.2.1 and 3.2.2 of Chapter 3. During this process, two more photolithography steps were added to prevent cross contamination. The cathode was covered by a positive photoresist (Microposit S1813, Shipley) while nickel electroplating for the anode, and the anode was also covered while silver electroplating for the cathode. The resulting thickness of both nickel and silver was 2 μm. Then, the electroplated nickel and silver were subjected to the oxide formation in an alkaline solution (1 M KOH). The electroplated nickel was voltammetry-cycled within -1.2 to 0.6 V with respect to a silver/silver chloride (Ag/AgCl) reference electrode in 1 M KOH at a scan rate of 10 mV/s for 80 times, resulting in the electrochemically formed nickel hydroxide. During this treatment for 8

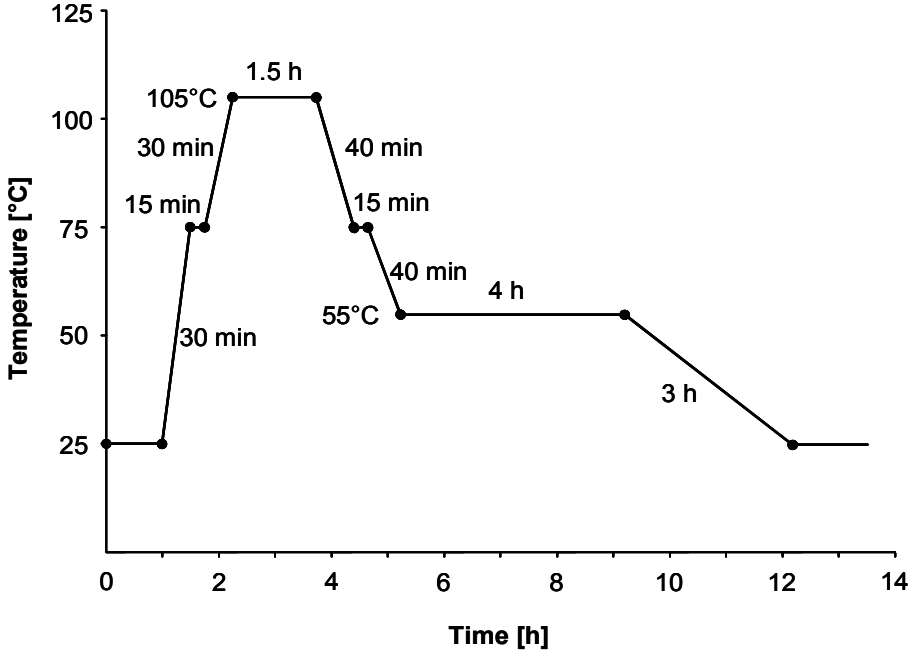

(a)

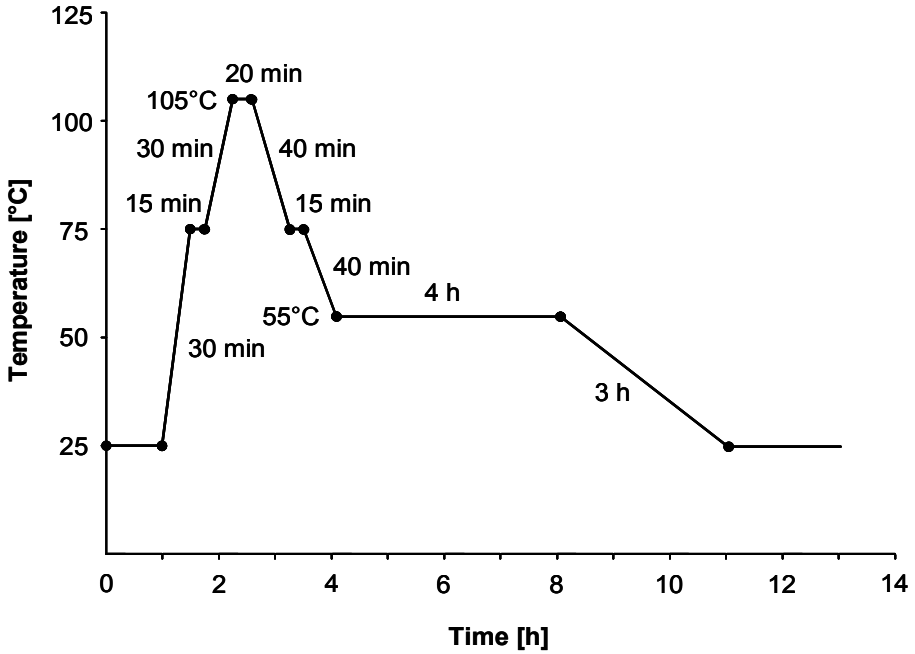

(b)

Figure 5.2. (a) Soft baking and (b) post-exposure baking process for 100 μm thick SU-8 50.

hours, the electroplated silver was involuntarily immersed in 1 M KOH along with the electroplated nickel, resulting in the chemically formed silver oxide.

Next, a 100 μm-thick microfluidic channel was constructed on the interdigitated microelectrodes array by means of a negative thick photoresist (Nano SU-8 50, MicroChem) photolithography. A 100 μm thickness (SU-8) was obtained by spinning for 30 seconds at 1000 rpm. The substrate was soft-baked at 97°C for 90 minutes on a hotplate. The applied soft-baking condition is detailed in Figure 5.2 (a). The SU-8 photoresist was then exposed using the same lithography equipment as used for the S1813 photoresist in the previous step. The exposure dose was approximately 390 mJ/cm^2. Immediately after exposure, the SU-8 layer was subjected to a post-exposure bake at 97°C for 20 minutes on a hotplate. The applied post-exposure baking condition is detailed in Figure 5.2 (b). Following post-exposure baking, the SU-8 photoresist was developed in a developing bath (Nano SU-8 Developer, MicroChem) for 10 minutes with mild agitation, then rinsed briefly with isopropyl alcohol (IPA), and finally dried with a gentle stream of nitrogen. Subsequently, the inlet and outlet holes of the microfluidic channel were drilled and the substrate was diced for packaging. The fabrication steps are illustrated in Figure 5.3. Figure 5.4 shows four different designs of the microscale fuel cell: 10, 20, 50, and 100 μm width and spacing of interdigitated microelectrodes. Figure 5.5 shows the assembled microscale fuel cell for testing.

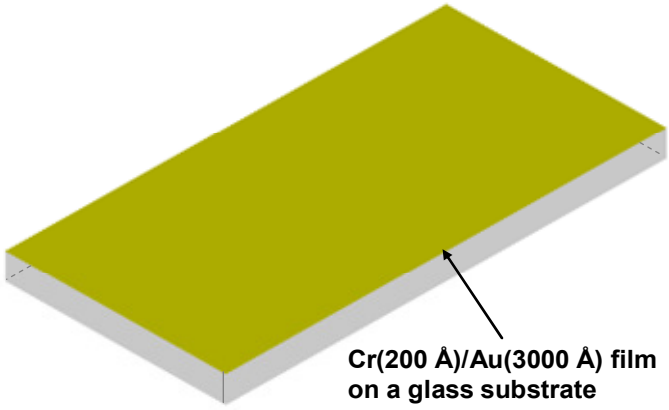

(a)

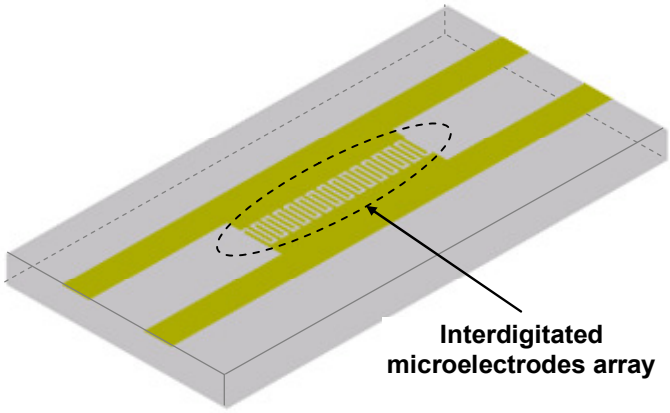

(b)

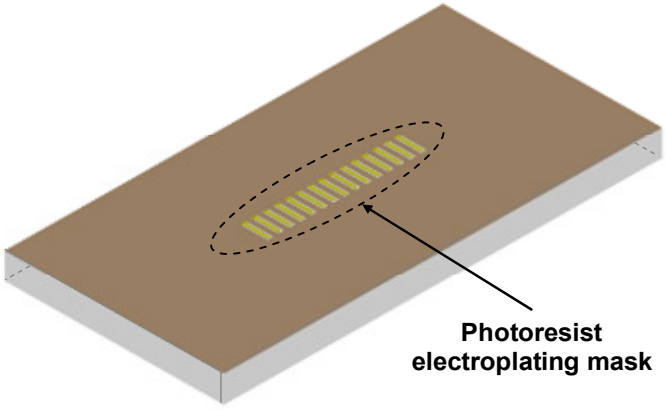

(c)

Figure 5.3. Fabrication steps of the microscale fuel cell.

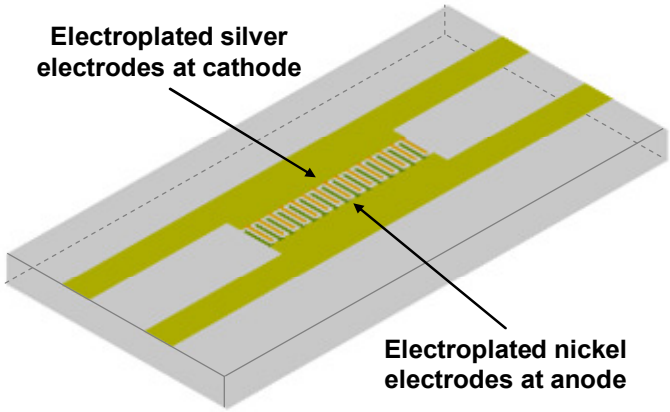

(d)

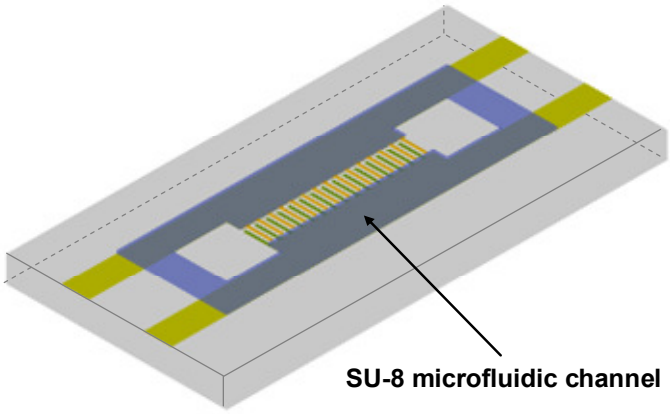

(e)

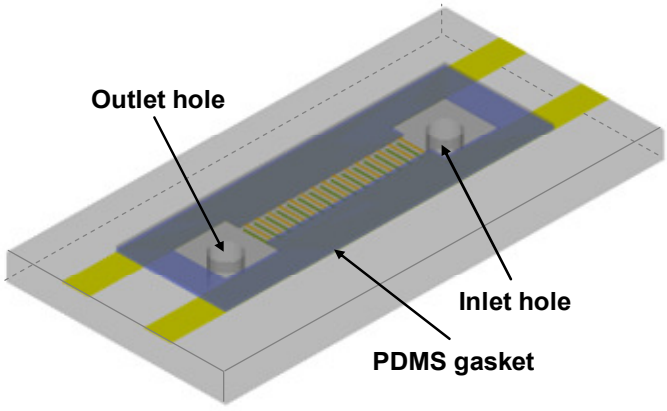

(f)

(Fig. cont'd)

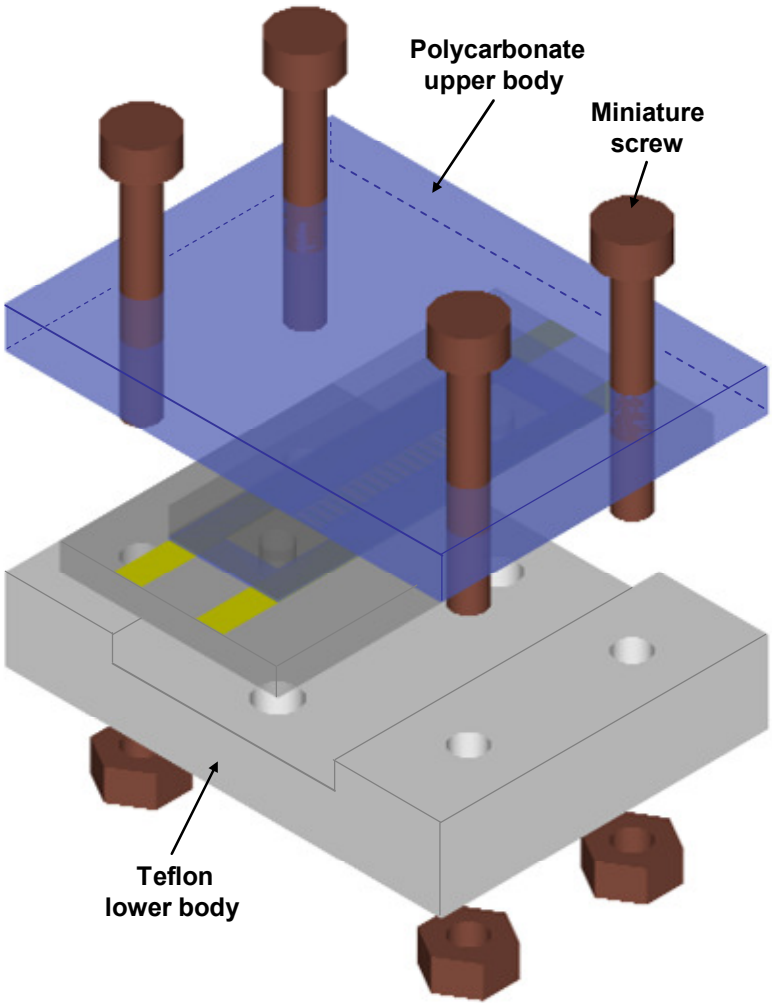
Polycarbonate
upper body
Miniature
screw
Teflon
lower body

(g)

(Fig. cont'd)

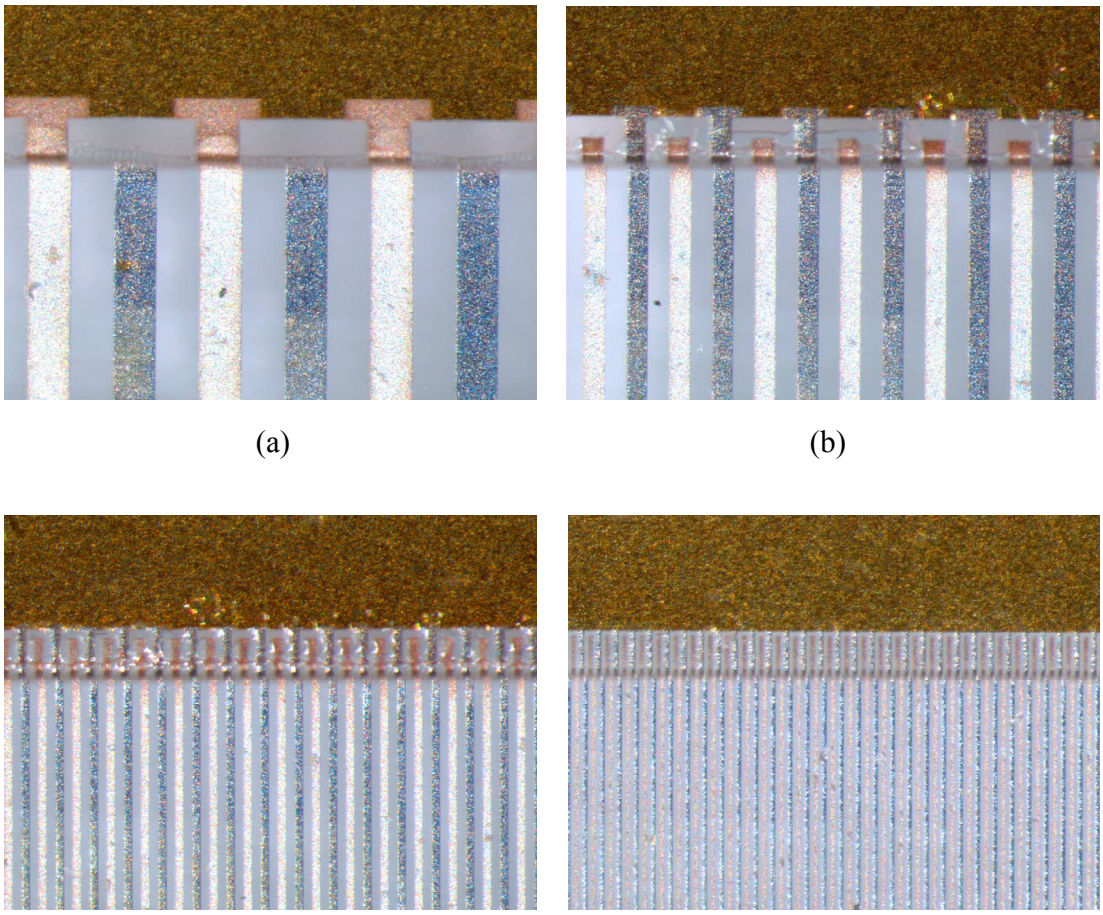

Figure 5.4. Microphotograph of interdigitated microelectrodes: (a) 100 μm; (b) 50 μm; (c) 20 μm, and (d) 10 μm width and spacing.

5.3 Microscale Fuel Cell Test Results

5.3.1 Electrical Measurement

To examine the electrical characteristics of the microscale fuel cell, the output voltages and currents were measured with various external loads. The output voltage measurement began in open circuit condition and finished in short circuit condition. The external loads were applied to control the output current in order of 1 MΩ, 470 kΩ,

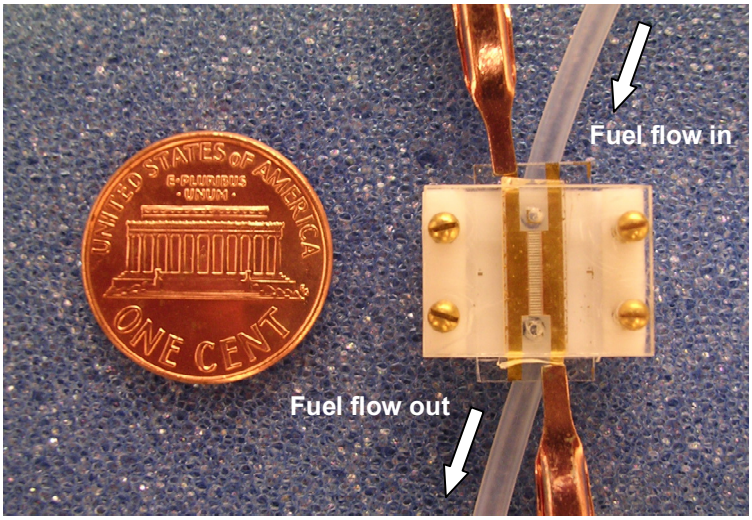

Figure 5.5. Photograph of the assembled microscale fuel cell. The packaged size is 15 mm × 12 mm × 5 mm.

270 kΩ, 100 kΩ, 56 kΩ, 27 kΩ, 10 kΩ, 5.6 kΩ, 2.7 kΩ, 1 kΩ, 560 Ω, 270 Ω, and 100 Ω. The output voltages and currents were measured by means of a Field Point module (FP-AI-110, National Instruments) and a user interface was created with LabVIEW (LabVIEW 7 Express, National Instruments). During the measurement, the fuel mixture (0.2 M KOH + 2 M CH_3OH + 0.05 M H_2O_2) was pumped into the microscale fuel cell using a syringe pump (PHD 2200, Harvard Apparatus). The fuel cell setup used for the electrical measurement is shown in Figure 5.6.

5.3.2 The Effect of Distance between Anode and Cathode

Depending on the distance effect observed at the macroscale, the effect of distance between anode and cathode on the fuel cell output was experimentally studied at the microscale: 10, 20, 50, and 100 μm. Such microscale dimensions were realized by

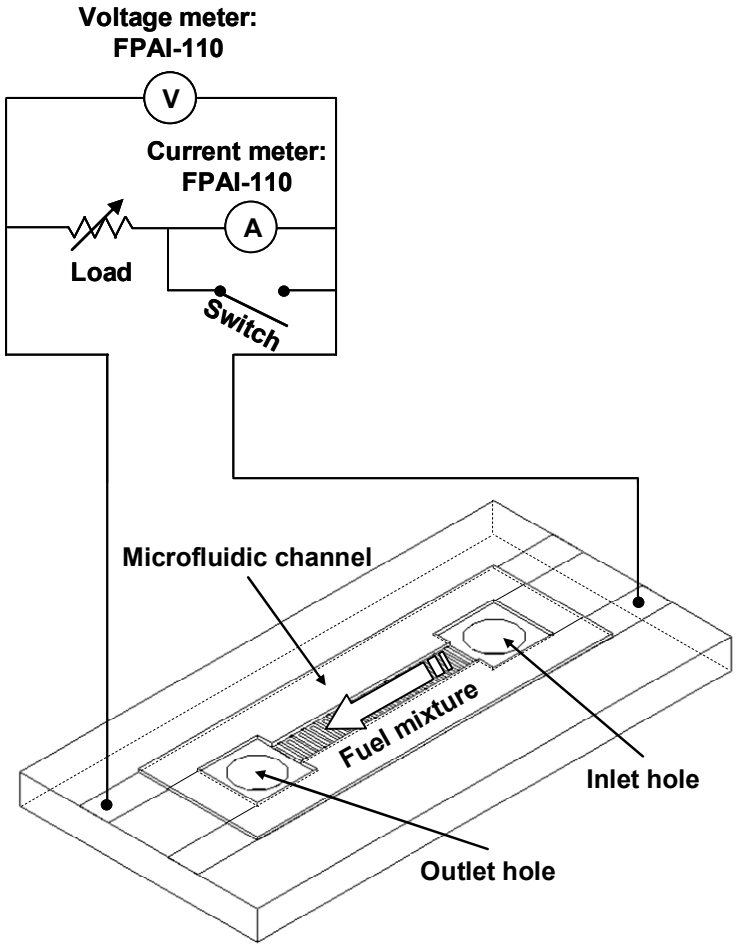

Figure 5.6. Schematic illustration of the experimental apparatus for testing the microscale fuel cell.

photolithography in microfabrication processes for the microscale fuel cell. For each distance, three microscale fuel cell samples were prepared and tested.

Nickel hydroxide at the anode was stabilized through the long-term fuel cell operation in conjunction with silver oxide at the cathode. At a fuel flow rate of 10 µl/min, the output current was measured with a load resistance of 100 Ω for 4 hours, and the result is shown in Figure 5.7. Despite different designs, the output current continuously decreased for 2 to 3 hours, and then settled at stabilized values, as observed with the

macroscale fuel cell (section 4.3.1 of Chapter 4). It is believed that the observed decline in the output current was caused by the aging effect of nickel hydroxide at the anode [56] as also explained in section 3.1.2 of Chapter 3.

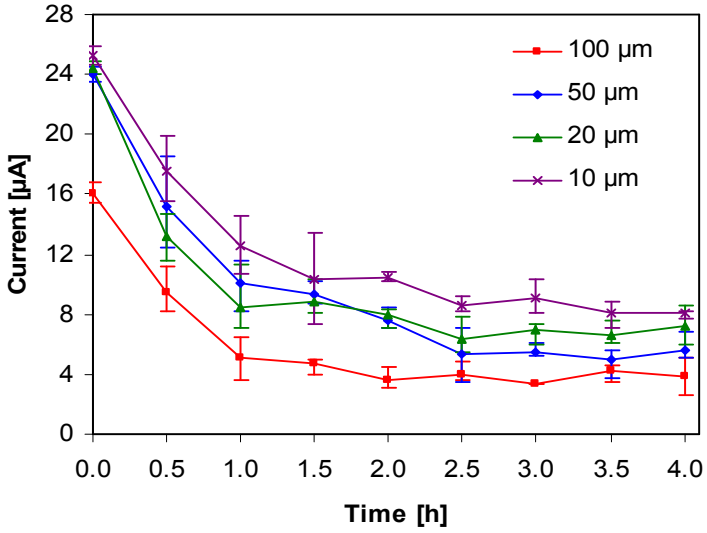

Figure 5.7. Aging effect of the anode catalyst (nickel hydroxide) on the fuel cell output current. The cathode catalyst was silver oxide. The output current was measured with a 100 Ω load resistance for 4 hours. Three samples of four different designs were tested: 10, 20, 50, and 100 μm width and spacing of interdigitated microelectrodes (1.35 mm^2). For each design, three sets of the output current were averaged and then plotted with an error bar. The fuel mixture of 0.2 M KOH + 2 M CH_3OH + 0.05 M H_2O_2 was supplied at a rate of 10 μl/min. Temperature was 22.5°C.

After stabilizing the catalysts in the microscale fuel cell, the output voltage and current were measured with various external loads for different distances between anode and cathode. As shown in Figure 5.8, not only at the macroscale but also at the microscale, the maximum output power density was dependent on the distance between anode and cathode. At a fuel flow rate of 10 μl/min, the 10 μm design showed an approximately 20%, 90%, and 137% higher maximum output power density compared to the 20, 50, and 100 μm designs, respectively. Considering the presence of reacting

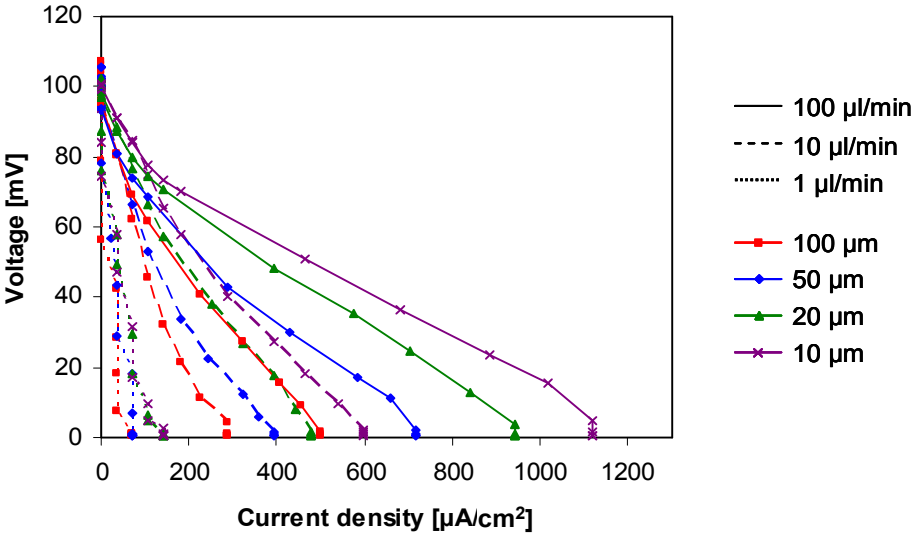

(a)

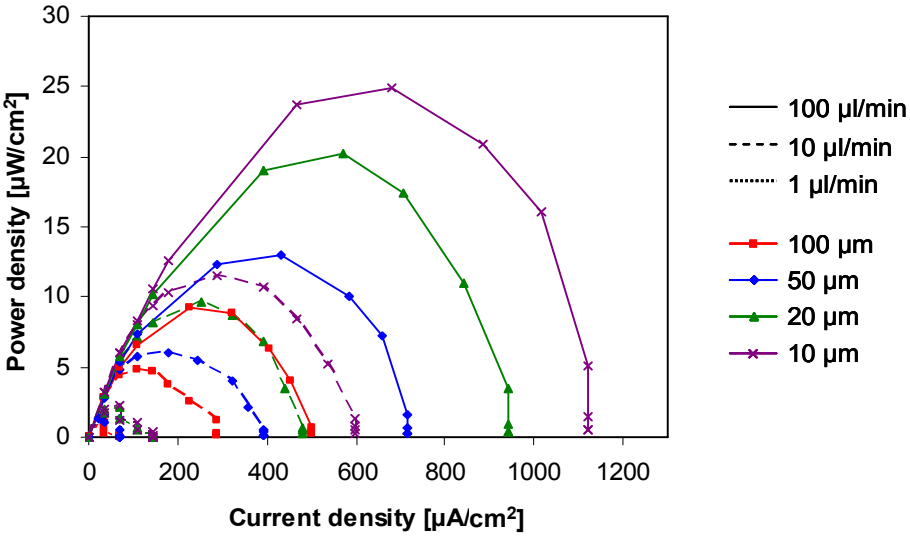

(b)

Figure 5.8. Effect of distance between anode and cathode on the fuel cell output: (a) the output voltage versus the output current density; (b) the output power density versus the output current density, and (c) the maximum output power density versus the distance between electrodes. For comparison, three different fuel mixture flow rates are present. The output voltage and current were measured with various external loads. For each design, three microscale fuel cell samples were tested. Three sets of the fuel cell output were averaged and then plotted. The fuel mixture of 0.2 M KOH + 2 M CH_3OH + 0.05 M H_2O_2 was supplied at a rate of 10 µl/min. Temperature was 22.5°C.

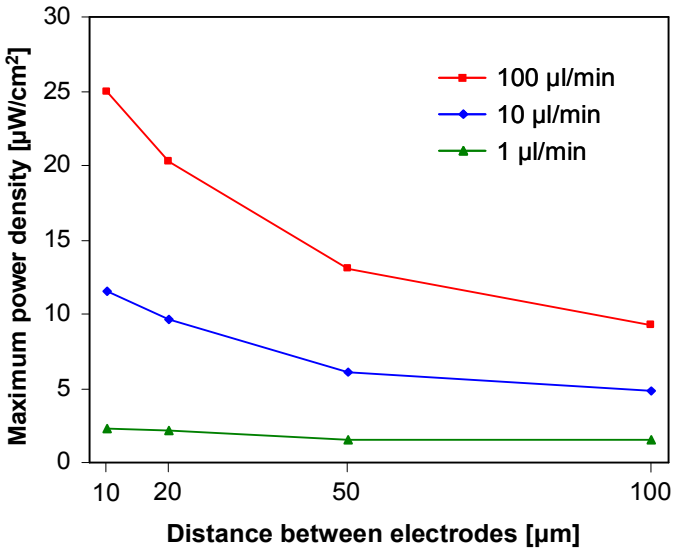

(c)

(Fig. cont'd)

species moving between anode and cathode, it is believed that a shorter distance between anode and cathode would lead to a faster transport time of reacting species and then more electrochemical reactions would occur at a given time developing a higher fuel cell output current.

5.3.3 The Effect of Fuel Mixture Flow Rate

As an another method to control the transport time of reacting species moving between anode and cathode, different fuel mixture flow rates were applied to the microscale fuel cell. In this experiment, flow rates of 1, 2, 5, 10, 20, 50, 100, and 200 μl/min were tested. Except for the fuel mixture flow rate, other test conditions were consistent with the previous experiment.

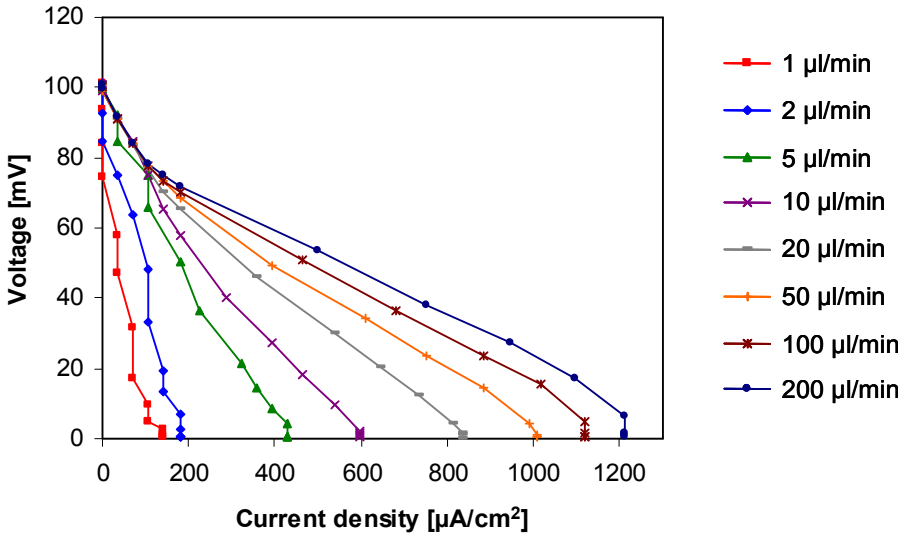

(a)

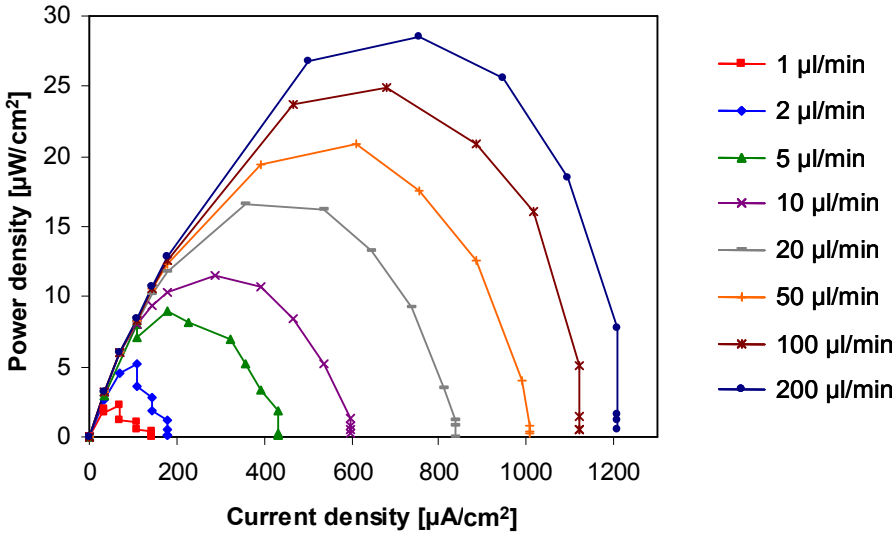

(b)

Figure 5.9. Effect of fuel mixture flow rate on the fuel cell output: (a) the output voltage versus the output current density (10 μm design); (b) the output power density versus the output current density (10 μm design), and (c) the maximum output power density versus the fuel mixture flow rate. For each flow rate, three microscale fuel cell samples were tested. Three sets of the fuel cell output were averaged and then plotted. The fuel mixture of 0.2 M KOH + 2 M CH_3OH + 0.05 M H_2O_2 was supplied. Temperature was 22.5°C.

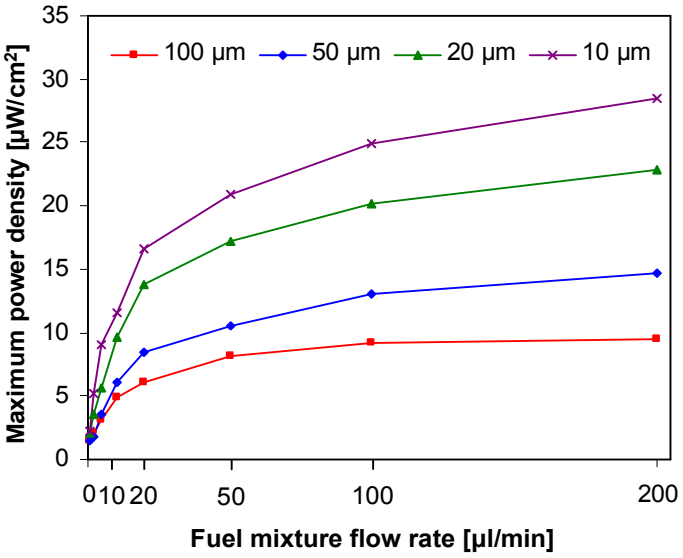

(c)

(Fig. cont'd)

The output voltage and current were measured with different external loads as a function of the fuel mixture flow velocity. A flow velocity can be calculated from the flow rate applied and the cross-sectional area of the microfluidic channel used. As shown in Figure 5.9, as the flow rate increased, the maximum output power density increased. A maximum output power density of 2.28, 11.67, and 25.44 µW/cm^2 was extractable from the 10 µm design at a flow rate of 1, 10, and 100 µl/min, respectively. Like a shorter distance between electrodes, a higher fuel mixture flow rate could enable a shorter transport time of reacting species moving between anode and cathode. Thus, it is believed that more electrochemical reactions would take place at a given time and a greater fuel cell output current could develop in the end. Despite insufficient evidence, it is also expected that besides mobile ions fuel and oxidant molecules can be also

influenced by the forced flow of fuel mixture. Thus, the number of fuel and/or oxidant species available at the surface of an electrode might increase and the electrochemical reaction rate could also increase.

5.4 Conclusions

The observed benefit from a reduced diffusion length of reacting species at the macroscale level was shown to extend to the microscale level. For this purpose, the microscale fuel cells with four different designs, 10, 20, 50, and 100 μm width and spacing of interdigitated microelectrodes, were fabricated and tested. At a fuel mixture flow rate of 200 μl/min, the maximum output power density of the 10 μm design (28.73 $\mu W/cm^2$) was nearly three times higher than that of the 100 μm design (9.72 $\mu W/cm^2$). This consequence can be interpreted that a shorter distance between anode and cathode would lead to a faster transport time of reacting species, which results in more electrochemical reactions at a given time and thus a higher output power. In addition, different fuel mixture flow rates from 1 to 200 μl/min were applied to the microscale fuel cell and their responses were also measured. As a result, the output power density was dependent on the fuel mixture flow velocity.

The advantages of the microscale fuel cell developed in this work, particularly over previously reported microscale direct methanol fuel cells [25-32], are no proton exchange membrane, inexpensive catalysts, and a simple planar structure. These merits enable high design flexibility and easy integration of the microscale fuel cell into actual microfluidic systems.

CHAPTER 6. CONCLUSIONS

6.1 Summary

As shown through the course of this thesis, the feasibility and characteristics of a methanol and hydrogen peroxide fuel cell concept was studied. In this work, methanol was used as a reductant at the anode, while hydrogen peroxide was used as an oxidant at the cathode in the presence of hydroxyl ions. A membraneless structure is one of the unique aspects of this fuel cell. Although a proton exchange membrane has been most commonly used for low-temperature fuel cells, it also has limitations in thickness, structural complexity, and a swelling problem due to hydration. Such operational complications led the development of a fuel cell without a proton exchange membrane in this work.

Due to the membraneless structure between anode and cathode, non-noble metals with relatively mild catalytic activity were selected to minimize cross reactions and thus to prevent mixed potentials at both electrodes. Therefore nickel hydroxide and silver oxide were employed as anode and cathode catalysts for the membraneless fuel cell structure. Although several studies of methanol oxidation on nickel hydroxide as well as hydrogen peroxide reduction on silver oxide have been reported, the actual catalytic reactions for the fuel cell applications were not well understood. Uncertain reaction mechanisms contribute to the difficulty of designing fuel cells, particularly microscale fuel cells. The associated reaction mechanism was therefore electroanalytically studied using cyclic voltammetry in Chapter 3.

For the anode and cathode catalysts, hydroxyl ions were essential to be electroactive for the redox reactions. In the presence of hydroxyl ions, nickel hydroxide catalyzed the anodic oxidation of methanol and silver oxide catalyzed the cathodic reduction of hydrogen peroxide. However, hydrogen peroxide was also reactive at nickel hydroxide, while methanol was not insensitive at silver oxide, which indicates that cross reactions could occur during fuel cell operation.

In Chapter 4, the actual performance of these catalysts was validated using a macroscale fuel cell. Nickel hydroxide at the anode was stabilized through the long-term fuel cell operation in conjunction with silver oxide at the cathode. Using the stabilized catalysts, the optimal fuel mixture composition was determined to be 0.2 M hydroxyl ions, 2 M methanol, and 0.05 M hydrogen peroxide, which produced the maximum output power density of 5.02 $\mu W/cm^2$. Based on the stabilized catalysts and the optimized fuel mixture, the distance effect on the fuel cell output was experimentally studied. A shorter distance between anode and cathode was shown to give a higher output power.

The microscale fuel cells (electrode area: 1.35 mm^2) with four different dimensions, 10, 20, 50, and 100 μm width and spacing of interdigitated microelectrodes, were fabricated and tested in Chapter 5. With the fuel mixture flow rate of 200 μl/min, the maximum output power density of 28.73 $\mu W/cm^2$ was obtained from the 10 μm design, which was nearly three times higher than the 100 μm design. In addition to different distances between anode and cathode, the microfluidic behavior of the microscale fuel cell was tested with various fuel mixture flow rates.

In this research, the methanol and hydrogen peroxide fuel cell was developed and demonstrated using non-noble catalysts in an alkaline solution. Based on a membraneless structure in this fuel cell, a shorter distance between anode and cathode was shown to generate a higher output power. Further developing this distance effect, the microscale fuel cell was constructed, which enabled microscale lengths for reactant diffusion and expedited the electrochemical reactions. The developed fuel cells do not require noble catalysts such as platinum and/or platinum alloy. Due to the simple structure of the developed fuel cells, the anode and cathode can be arranged on the same plane without a proton exchange membrane, which enables that the fuel cell dimensions can be flexibly adjusted to meet specific design needs for the applications of microfluidic systems and portable power sources.

6.2 Future Research

The viability of a methanol and hydrogen peroxide fuel cell was shown in this work. As a result, there are many opportunities suggested for future research. Some of these opportunities are briefly discussed below.

The membraneless structure gives reasonable promise to overcome the critical limitations of a proton exchange membrane. Future work could include the comparative study of fuel cells with and without a proton exchange membrane in order to elucidate the advantages and disadvantages of the membraneless fuel cell structure.

Considering probable cross reactions from the membraneless structure, non-noble metals were employed as catalysts in the developed fuel cell. However, the mild catalytic activity of the non-noble metals causes the low fuel cell output power. Thus, future work should include the development of catalysts that are reactive comparable to precious

catalysts but applicable to the membraneless structure. For the characterization of catalysts, diverse analytical methods including spectroscopy could be utilized along with voltammetry.

The fuel cell tests carried out in this work were based on a single cell, but future work would include fuel cell tests with multiple cells connected in series, parallel, or combinations of both. The uncomplicated structure of the developed fuel cell can facilitate the cell-to-cell connection. Further, due to its structural simplicity, a large scale cell-to-cell connection can be feasible for the improved extractable power density.

On the microscale fuel cells, the output power was shown to be dependent on the fuel mixture flow rate, but the related explanation was not clearly provided in this thesis. Therefore, more in-depth investigations are required in future work. Further, these studies would lead to a comprehensive understanding of the microfluidic behavior of microscale fuel cells.

REFERENCES

[1] L. J. M. J. Blomen and M. N. Mugerwa, *Fuel Cell Systems,* New York and London: Plenum Press, 1993.

[2] G. Hoogers, *Fuel Cell Technology Handbook,* Boca Raton: CRC Press, 2002.

[3] U. S. Department of Energy (DoE), "DOE – Fossil Energy: DOE's Fuel Cell R&D Program," July 2006, http://www.fossil.energy.gov/programs/powersystems/fuelcells.

[4] T. E. Lipman, "What Will Power the Hydrogen Economy? Present and Future Sources of Hydrogen Energy," Institute of Transportation Studies, Davis, CA, Tech. Rep. UCD-ITS-RR-04-10, 2004.

[5] A. J. Appleby, "Fuel Cell Technology: Status and Future Prospects," *Energy,* vol. 21, pp. 521-653, August 1996.

[6] J.-H. Wee, "Applications of Proton Exchange Membrane Fuel Cell Systems," *Renewable and Sustainable Energy Reviews,* Article in Press.

[7] C. Stone and A. E. Morrison, "From Curiosity to Power to Change the World," *Solid State Ionics,* vol. 152, pp. 1-13, December 2002.

[8] G. F. McLean, T. Niet, S. Prince-Richard, and N. Djilali, "An Assessment of Alkaline Fuel Cell Technology," *International Journal of Hydrogen Energy,* vol. 27, pp. 507-526, May 2002.

[9] J. C. Yang, Y. S. Park, S. H. Seo, H. J. Lee, and J. S. Noh, "Development of A 50 kW PAFC Power Generation System," *Journal of Power Sources,* vol. 106, pp. 68-75, April 2002.

[10] N. Sammes, R. Bove, and K. Stahl, "Phosphoric Acid Fuel Cells: Fundamentals and Applications," *Current Opinion in Solid State and Materials Science,* vol. 8, pp. 372-378, October 2004.

[11] A. Dicks and A. Siddle, "Assessment of Commercial Prospects of Molten Carbonate Fuel Cells," *Journal of Power Sources,* vol. 86, pp. 316-323, March 2000.

[12] O. Yamamoto, "Solid Oxide Fuel Cells: Fundamental Aspects and Prospects," *Electrochimica Acta,* vol. 45, pp. 2423-2435, May 2000.

[13] S. C. Singhal, "Advances in Solid Oxide Fuel Cell Technology," *Solid State Ionics,* vol. 135, pp. 305-313, November 2000.

[14] J. Larminie and A. Dicks, *Fuel Cell Systems Explained, 2nd ed.,* Chichester: John Wiley & Sons Ltd., 2003.

[15] A. S. Aricó, S. Srinivasan, and V. Antonucci, "DMFCs: From Fundamental Aspects to Technology Development," *Fuel Cells,* vol. 1, pp. 133-161, September 2001.

[16] S. Song and P. Tsiakaras, "Recent Progress in Direct Ethanol Proton Exchange Membrane Fuel Cells (DE-PEMFCs)," *Applied Catalysis B: Environmental,* vol. 63, pp. 187-193, March 2006.

[17] Y. Zhu, S. Y. Ha, and R. I. Masel, "High Power Density Direct Formic Acid Fuel Cells," *Journal of Power Sources,* vol. 130, pp. 8-14, May 2004.

[18] M. M. Mench, H. M. Chance, and C. Y. Wang, "Direct Dimethyl Ether Polymer Electrolyte Fuel Cells for Portable Applications," *Journal of the Electrochemical Society,* vol. 151, pp. A144-A150, December 2003.

[19] C. Ponce de Leon, F. C. Walsh, D. Pletcher, D. J. Browning, and J. B. Lakeman, "Direct Borohydride Fuel Cells," *Journal of Power Sources,* vol. 155, pp. 172-181, April 2006.

[20] R. F. Service, "Shrinking Fuel Cells Promise Power in Your Pocket," *Science,* vol. 296, pp. 1222-1224, May 2002.

[21] J.-M. Tarascon and M. Armand, "Issues and Challenges Facing Rechargeable Lithium Batteries," *Nature,* vol. 414, pp. 359-367, November 2001.

[22] S. K. Dhar, S. R. Ovshinsky, P. R. Gifford, D. A. Corrigan, M. A. Fetcenko, and S. Venkatesan, "Nickel/Metal Hydride Technology for Consumer and Electric Vehicle Batteries – A Review and Up-Date," *Journal of Power Sources,* vol. 65, pp. 1-7, April 1997.

[23] C. K. Dyer, "Fuel Cells for Portable Applications," *Journal of Power Sources,* vol. 106, pp. 31-34, April 2002.

[24] H. L. Maynard and J. P. Meyers, "Miniature Fuel Cells for Portable Power: Design Considerations and Challenges," *Journal of Vacuum Science and Technology B,* vol. 20, pp. 1287-1297, August 2002.

[25] S. C. Kelley, G. A. Deluga, and W. H. Smyrl, "A Miniature Methanol/Air Polymer Electrolyte Fuel Cell," *Electrochemical and Solid-State Letters,* vol. 3, pp. 407-409, July 2000.

[26] S. C. Kelley, G. A. Deluga, and W. H. Smyrl, "Miniature Fuel Cells Fabricated on Silicon Substrates," *Journal of American Institute of Chemical Engineers,* vol. 48, pp. 1071-1082, May 2002.

[27] S. R. Narayanan, T. I. Valdez, and F. Clara, "Development of A Miniature Fuel Cell for Portable Applications," in *Proceedings of the 199th Meeting on Direct Methanol Fuel Cell, Electrochemical Society,* 2001, pp. 254-263.

[28] H. Chang, J. R. Kim, J. H. Cho, H. K. Kim, and K. H. Choi, "Materials and Processes for Small Fuel Cells," *Solid State Ionics,* vol. 148, pp. 601-606, June 2002.

[29] C. Xie, J. Bostaph, and J. Pavio, "Development of A 2 W Direct Methanol Fuel Cell Power Source," *Journal of Power Sources,* vol. 136, pp. 55-65, July 2004.

[30] T. J. Yen, N. Fang, X. Zhang, G. Q. Lu, and C. Y. Wang, "A Micro Methanol Fuel Cell Operating at Near Room Temperature," *Applied Physics Letters,* vol. 83, pp. 4056-4058, November 2003.

[31] G. Q. Lu, C. Y. Wang, T. J. Yen, and X. Zhang, "Development and Characterization of A Silicon-Based Micro Direct Methanol Fuel Cell," *Electrochimica Acta,* vol. 49 pp. 821-828, February 2004.

[32] S.-C. Yao, X. Tang, C.-C. Hsieh, Y. Alyousef, M. Vladimer, G. K. Fedder, and C. H. Amon, "Micro-Electro-Mechanical Systems (MEMS)-Based Micro-Scale Direct Methanol Fuel Cell Development," *Energy,* vol. 31, pp. 636-649, April 2006.

[33] S. Aravamudhan, A. R. A. Rahman, and S. Bhansali, "Porous Silicon Based Orientation Independent, Self-Priming Micro Direct Ethanol Fuel Cell," *Sensors and Actuators A,* vol. 123-124, pp. 497-504, September 2005.

[34] J. Yeom, R. S. Jayashree, C. Rastogi, M. A. Shannon, and P. J. A. Kenis, "Passive Direct Formic Acid Microfabricated Fuel Cells," *Journal of Power Sources,* Article in Press.

[35] X. Ren, M. S. Wilson, and S. Gottesfeld, "High Performance Direct Methanol Polymer Electrolyte Fuel Cells," *Journal of the Electrochemical Society,* vol. 143, pp. L12-L15, January 1996.

[36] D. H. Jung, C. H. Lee, C. S. Kim, and D. R. Shin, "Performance of A Direct Methanol Polymer Electrolyte Fuel Cell," *Journal of Power Sources,* vol. 71, pp. 169-173, March 1998.

[37] S. Slade, S. A. Campbell, T. R. Ralph, and F. C. Walsh, "Ionic Conductivity of An Extruded Nafion 1100 EW Series of Membranes," *Journal of the Electrochemical Society,* vol. 149, pp. A1556-A1564, October 2002.

[38] J. Ling and O. Savadogo, "Comparison of Methanol Crossover Among Four Types of Nafion Membranes," *Journal of the Electrochemical Society,* vol. 151, pp. A1604-A1610, September 2004.

[39] J. G. Liu, T. S. Zhao, Z. X. Liang, and R. Chen, "Effect of Membrane Thickness on the Performance and Efficiency of Passive Direct Methanol Fuel Cells," *Journal of Power Sources,* vol. 153, pp. 61-67, January 2006.

[40] J.-W. Choi and W. Sung, "A Planar and Membraneless Microscale Fuel Cell Using Nickel and Silver as Catalysts," in *Technical Digest of the 13th International Conference on Solid-State Sensors, Actuators, and Microsystems,* 2005, pp. 1852-1855.

[41] S. M. Haile, "Fuel Cell Materials and Components," *Acta Materialia,* vol. 51, pp. 5981-6000, November 2003.

[42] G. Q. Lu and C. Y. Wang, "Electrochemical and Flow Characterization of A Direct Methanol Fuel Cell," *Journal of Power Sources,* vol. 134, pp. 33-40, July 2004.

[43] P. Argyropoulos, K. Scott, and W. M. Taama, "Carbon Dioxide Evolution Patterns in Direct Methanol Fuel Cells," *Electrochimica Acta,* vol. 44, pp. 3575-3584, June 1999.

[44] D.-S. Meng, T. Cubaud, C.-M. Ho, and C.-J. Kim, "A Membrane Breather for Micro Fuel Cell with High Concentration Methanol," in *Technical Digest of Solid-State Sensor, Actuator and Microsystems Workshop, 2004*, pp. 141-144.

[45] K. Tüber, D. Pócza, and C. Hebling, "Visualization of Water Buildup in the Cathode of A Transparent PEM Fuel Cell," *Journal of Power Sources,* vol. 124, pp. 403-414, November 2003.

[46] C. Iwakura, H. Tamura, and T. Ishino, "On the Methanol-Hydrogen Peroxide Fuel Cell," *Journal of the Electrochemical Society of Japan,* vol. 36, pp. 107-113, January 1968.

[47] T.-C. Wen, S.-M. Lin, and J.-M. Tsai, "Sulphur Content and the Hydrogen Evolving Activity of NiS_x Deposits Using Statistical Experimental Strategies," *Journal of Applied Electrochemistry,* vol. 24, pp. 233-238, March 1994.

[48] C. Fan, D. L. Piron, A. Sleb, and P. Paradis, "Study of Electrodeposited Nickel-Molybdenum, Nickel-Tungsten, Cobalt-Molybdenum and Cobalt-Tungsten as Hydrogen Electrodes in Alkaline Water Electrolysis," *Journal of the Electrochemical Society,* vol. 141, pp. 382-387, February 1994.

[49] I. A. Raj and K. I. Vasu, "Transition Metal-Based Hydrogen Electrodes in Alkaline Solution – Electrocatalysis on Nickel Based Binary Alloy Coatings," *Journal of Applied Electrochemistry,* vol. 20, pp. 32-38, January 1990.

[50] M. A. Casadei and D. Pletcher, "The Influence of Conditions on the Electrocatalytic Hydrogeneration of Organic Molecules," *Electrochimica Acta,* vol. 33 pp. 117-120 January 1988.

[51] M. Fleischmann, K. Korinek, and D. Pletcher, "The Oxidation of Organic Compounds at A Nickel Anode in Alkaline Solution," *Journal of Electroanalytical Chemistry,* vol. 31, pp. 39-49, June 1971.

[52] J. Taraszewska and G. Roslonek, "Electrocatalytic Oxidation of Methanol on A Glassy Carbon Electrode Modified by Nickel Hydroxide Formed by Ex Situ Chemical Precipitation," *Journal of Electroanalytical Chemistry,* vol. 364, pp. 209-213, January 1994.

[53] A. A. El-Shafei, "Electrocatalytic Oxidation of Methanol at A Nickel Hydroxide/Glassy Carbon Modified Electrode in Alkaline Medium," *Journal of Electroanalytical Chemistry,* vol. 471, pp. 89-95, August 1999.

[54] M. A. Abdel Rahim, R. M. Abdel Hameed, and M. W. Khalil, "Nickel as A Catalyst for the Electro-Oxidation of Methanol in Alkaline Medium," *Journal of Power Sources,* vol. 134, pp. 160-169, August 2004.

[55] P. Oliva, J. Leonardi, J. F. Laurent, C. Delmas, J. J. Braconnier, M. Figlarz, F. Fievet, and A. de Guibert, "Review of the Structure and the Electrochemistry of Nickel Hydroxides and Oxy-Hydroxides," *Journal of Power Sources,* vol. 8, pp. 229-255, April 1982.

[56] P. V. Kamath, M. Dixit, L. Indira, A. K. Shukla, V. G. Kumar, and N. Munichandraiah, "Stabilized Alpha-$Ni(OH)_2$ as Electrode Material for Alkaline Secondary Cells," *Journal of the Electrochemical Society,* vol. 141, pp. 2956-2959, November 1994.

[57] M.-S. Kim, T.-S. Hwang, and K.-B. Kim, "A Study of the Electrochemical Redox Behavior of Electrochemically Precipitated Nickel Hydroxides Using Electrochemical Quartz Crystal Microbalance," *Journal of the Electrochemical Society,* vol. 144, pp. 1537-1543, May 1997.

[58] A. van der Ven, D. Morgan, Y. S. Meng, and G. Cender, "Phase Stability of Nickel Hydroxides and Oxyhydroxides," *Journal of the Electrochemical Society,* vol. 153, pp. A210-A215, February 2006.

[59] S. B. Hall, E. A. Khudaish, and A. L. Hart, "Electrochemical Oxidation of Hydrogen Peroxide at Platinum Electrodes. Part 1. An Adsorption-Controlled Mechanism," *Electrochimica Acta,* vol. 43, pp. 579-588, November 1997.

[60] S. B. Hall, J. J. Nairn, and E. A. Khudaish, "Potential and Temperature Dependence of Hydrogen Peroxide Oxidation at Nickel Electrodes," *Physical Chemistry Chemical Physics,* vol. 3, pp. 4566-4571, October 2001.

[61] S. U. Falk and A. J. Salkind, *Alkaline Storage Batteries,* New York: John Wiley & Sons Ltd., 1969.

[62] H.-K. Lee, J.-P. Shim, M.-J. Shim, S.-W. Kim, and J.-S. Lee, "Oxygen Reduction Behavior with Silver Alloy Catalyst in Alkaline Media," *Materials Chemistry and Physics,* vol. 45, pp. 238-242, September 1996.

[63] N. Wagner, M. Schulze, and E. Gülzow, "Long Term Investigations of Silver Cathodes for Alkaline Fuel Cells," *Journal of Power Sources,* vol. 127, pp. 264-272, March 2004.

[64] K. Matsuoka, Y. Iriyama, T. Abe, M. Matsuoka, and Z. Ogumi, "Alkaline Direct Alcohol Fuel Cells Using An Anion Exchange Membrane," *Journal of Power Sources,* vol. 150, pp. 27-31, October 2005.

[65] G. Bianchi, G. Caprioglio, F. Mazza, and T. Mussini, "The Electrochemical Behavior of Oxygen and Hydrogen Peroxide on Silver Electrodes," *Electrochimica Acta,* vol. 4, pp. 232-241, August 1961.

[66] C. Iwakura, Y. Matsuda, and H. Tamura, "Cathodic Reduction of H_2O_2 on Silver in Alkaline Solution," *Electrochimica Acta,* vol. 16, pp. 471-477, April 1971.

[67] M. Honda, T. Kodera, and H. Kita, "On the Electrochemical Behavior of H_2O_2 at Ag in Alkaline Solution," *Electrochimica Acta,* vol. 28, pp. 727-733, May 1983.

[68] E. R. Savinova, S. Wasle, and K. Doblhofer, "Structure and Activity Relations in the Hydrogen Peroxide Reduction at Silver Electrodes in Alkaline NaF/NaOH Electrolytes," *Electrochimica Acta,* vol. 44, pp. 1341-1348, December 1998.

[69] D. J. Brodrecht, D. N. Prater, and J. J. Rusek, "Novel Fuel Cells Using Hydrogen Peroxide," Swift Enterprises Ltd., West Lafayette, IN, Tech. Rep. 2001.

[70] W. T. Hess, "Hydrogen Peroxide," in *Kirk-Othmer Encyclopedia of Chemical Technology, 4th ed.,* J. I. Kroschwitz, Ed., New York: John Wiley & Sons Ltd., 1995, pp. 37-42.

[71] D. N. Prater and J. J. Rusek, "Energy Density of A Methanol/Hydrogen Peroxide Fuel Cell," *Applied Energy,* vol. 74, pp. 135-140, February 2003.

[72] A. Nagy and G. Mestl, "High Temperature Partial Oxidation Reactions over Silver Catalysts," *Applied Catalysis A: General,* vol. 188, pp. 337-353, November 1999.

[73] M. Qian, M. A. Liauw, and G. Emig, "Formaldehyde Synthesis from Methanol over Silver Catalysts," *Applied Catalysis A: General,* vol. 238, pp. 211-222, January 2003.

[74] I. E. Wachs, "Extending Surface Science Studies to Industrial Reaction Conditions: Mechanism and Kinetics of Methanol Oxidation over Silver Surfaces," *Surface Science,* vol. 544, pp. 1-4, October 2003.

[75] The Paul Lutz Microfabrication Center, University of Louisville, "Nickel Electroplating Using Shipley Megaposit SPR220 Positive Resist as a Mold," 2001, http://mitghmr.spd.louisville.edu/lutz/resources/sops/niplate/nieplate.htm.

[76] C. G. Granqvist, *Handbook of Inorganic Electrochromic Materials,* Amsterdam: Elsevier, 1995.

[77] A. Soto, "Electrochromism in Nickel-Based Oxides," Ph. D. dissertation, Uppsala University, Sweden, 2004.

[78] D. A. Skoog, D. M. West, F. J. Holler, and S. R. Crouch, *Fundamentals of Analytical Chemistry 8th ed.,* Belmont: Thomson Brooks/Cole, 2004.

[79] P. M. S. Monk, *Fundamentals of Electroanalytical Chemistry,* Chichester: John Wiley & Sons Ltd., 2001.

[80] G. Vértes and G. Horányi, "Some Problems of the Kinetics of the Oxidation of Organic Compounds at Oxide-Covered Nickel Electrodes," *Journal of Electroanalytical Chemistry,* vol. 52, pp. 47-53, April 1974.

[81] P. M. Robertson, "On the Oxidation of Alcohols and Amines at Nickel Oxide Electrodes: Mechanistic Aspects," *Journal of Electroanalytical Chemistry,* vol. 111, pp. 97-104, July 1980.

[82] E. R. Choban, P. Waszczuk, and P. J. A. Kenis, "Characterization of Limiting Factors in Laminar Flow-Based Membraneless Microfuel Cells," *Electrochemical and Solid-State Letters,* vol. 8, pp. A348-A352, May 2005.

APPENDIX. CYCLIC VOLTAMMETRY SETUP

A.1 Introduction

Cyclic voltammetry is an effective method to investigate the mechanism of redox reactions in an electrochemical cell. Cyclic voltammetry is based on the measured current in response to the applied voltage. The voltage applied to the electrode makes its surface negatively or positively charged, so that reducible species can receive electrons from the surface or oxidizable species can generate electrons to the surface. During oxidation or reduction, the current is measured at the electrode [79]. For this purpose, a three-electrode system consisting of working, auxiliary, and reference electrodes is used in the cyclic voltammetry setup (section A.2.1). These three electrodes are immersed in an analyte solution and connected to a potentiostat. The potentiostat enables a potential difference between the reference electrode and working electrode to track the applied voltage with minimal interference from an IR drop [83]. Along with the potentiostat, a voltage follower ensures minimal current flows through the reference electrode, thereby avoiding the polarization of the reference electrode and thus keeping the applied potential between the reference electrode and working electrode stable [83]. Most of the actual current flows between the auxiliary electrode and working electrode. As a current-measuring instrument, a current-to-voltage converter is adopted (section A.2.2). For signal generation and data input/output in the cyclic voltammetry setup, LabVIEW with Field Point modules is utilized. In the actual operation, microprocessor-based instruments are interfaced with analog circuits including a potentiostat, voltage follower,

and current-to-voltage converter. LabVIEW offers diverse built-in functions on the basis of a graphic user interface and has universal acceptance in research and manufacturing settings [84]. In this work, the LabVIEW-based control program is developed not only to generate voltage-time functions, but also to gather current-voltage signals. The Field Point module serves as a digital-to-analog converter between the LabVIEW-based control program and an electrochemical cell. Through the Field Point module, voltage excitations digitally generated by LabVIEW are applied to the analog potentiostat. In the same way, current responses from the cell are transformed at the analog current-to-voltage converter and then digitally sampled by the Field Point module (section A.2.3). The developed cyclic voltammetry setup is validated with the standard electroanalyte, the ferricyanide/ferrocyanide redox couple (section A.3).

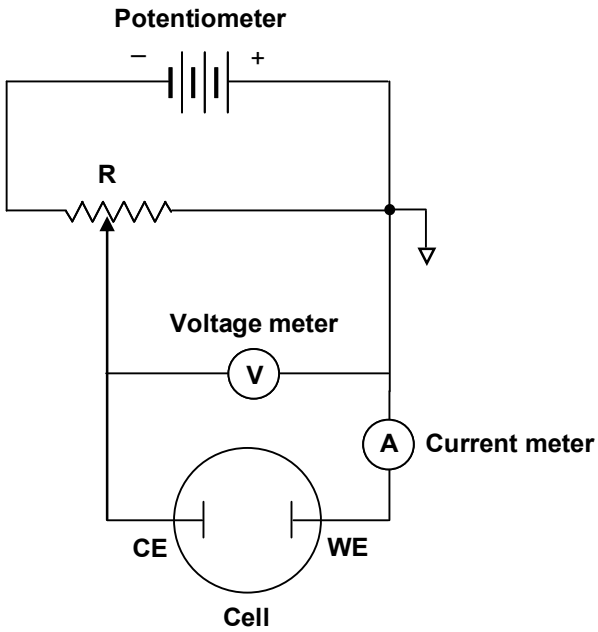

Figure A.1. Schematic illustration of the two-electrode system equipped with a potentiometer.

A.2 Cyclic Voltammetry Setup

A.2.1 Three-Electrode System

Note: Main body of this section is primarily based on Kissinger's article in *Laboratory Techniques in Electroanalytical Chemistry* edited by Kissinger and Heineman [85].

Early voltammetry was carried out using a two-electrode system rather than a three-electrode system [78]. The two-electrode system consists of the working electrode and counter electrode. Figure A.1 illustrates the two-electrode system equipped with a potentiometer to apply a potential difference to an electrochemical cell. The applied voltage is measured between the counter electrode and working electrode, and the resulting current is measured from the working electrode. The working electrode is grounded, regardless of a potential difference between the counter electrode and working electrode. Figure A.2 depicts the situation inside the two-electrode cell [85]. The applied voltage (V_{in}) is divided into the interfacial potential difference at the counter electrode ($Ø_c$) and at the working electrode ($Ø_w$), so there is no potential difference across the bulk solution. The interfacial region where a high potential gradient (typically 10^6 V/cm) exists is called the electrical double layer. Within this layer, electrochemical reactions actually occur [85]. Ideally, in the two-electrode system, the interfacial potential difference at the counter electrode ($Ø_c$) is fixed using a large metal electrode such like a pool of mercury or reversible redox couple such as silver/silver chloride, while the interfacial potential difference at the working electrode is variable ($Ø_w$), tracking the applied voltage [85]. This ideal condition can be realized under the zero-current condition as presented in Figure A.2 (a). However, under the finite-current condition (Figure A.2 (b) and (c)), the two-electrode system suffers from an IR drop. At the given

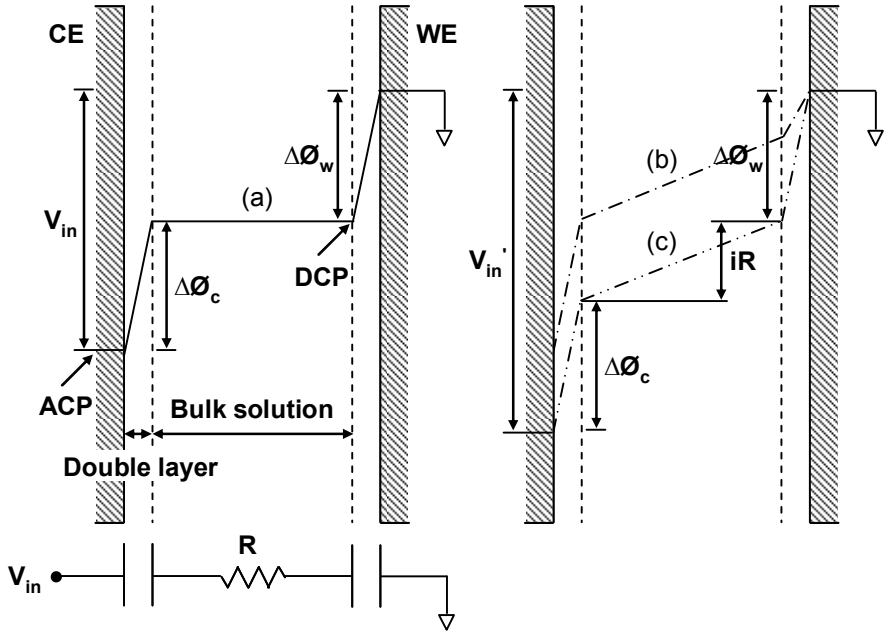

Figure A.2. Schematic illustration of potential gradients between the counter electrode and working electrode in a two-electrode cell [85]. (a) Under the zero-current condition, the interfacial potential difference at the counter electrode ($\Delta Ø_c$) is fixed by employing a large metal electrode or reversible redox couple, while the interfacial potential difference at the working electrode ($\Delta Ø_w$) is adjustable by controlling the applied voltage (V_{in}). Thus, the desired control point (DCP) is necessarily at the interface between the bulk solution and charge double layer, though the actual control point (ACP) is on the metal side of the counter electrode interface. (b) Once reacting species in an analyte solution are electroactive at the given $\Delta Ø_w$, the associated redox reaction would take place, which leads to a charge flow and thus to an IR drop across the bulk solution. (c) Under such finite-current condition, $\Delta Ø_w$ will necessarily drop, but the associated redox reaction could resume immediately, since the applied voltage must be increased by the value of IR drop so as to maintain $\Delta Ø_w$ at the desired value. With the given potentiometer, though, such IR drop compensation should be performed manually. For automatic adjustment, a potentiostat is required.

interfacial potential difference at the working electrode, reacting species in the solution become electroactive, so that the associated electrochemical reaction can take place. The electron transfer reaction results in a flow of charge and thus the IR drop across the bulk solution. In the solution, a higher resistance and a larger current can lead to a greater IR drop. To maintain the interfacial potential difference at the working electrode at the

desired value, the applied voltage must be increased by the value of IR drop across the bulk solution, as shown in Figure A.2 (c) [85]. Such undesirable situations are mainly attributed to the remoteness of the actual control point from the desired control point as indicated in Figure A.2 (a) [85].

As discussed above, the counter electrode in the two-electrode system serves two functions at the same time: enabling the flow of charge through the cell and maintaining a constant interfacial potential difference irrespective of the current. Both tasks can be better undertaken by two separate electrodes: an auxiliary electrode for the first purpose and a reference electrode for the second [85]. With the addition of these two electrodes to the working electrode, the three-electrode system is constituted as illustrated in Figure A.3. For the cyclic voltammetry setup used in this work, a platinum wire coil and commercially available Ag/AgCl in 3.5 M KCl (WRE5001, Weiss Research) were used

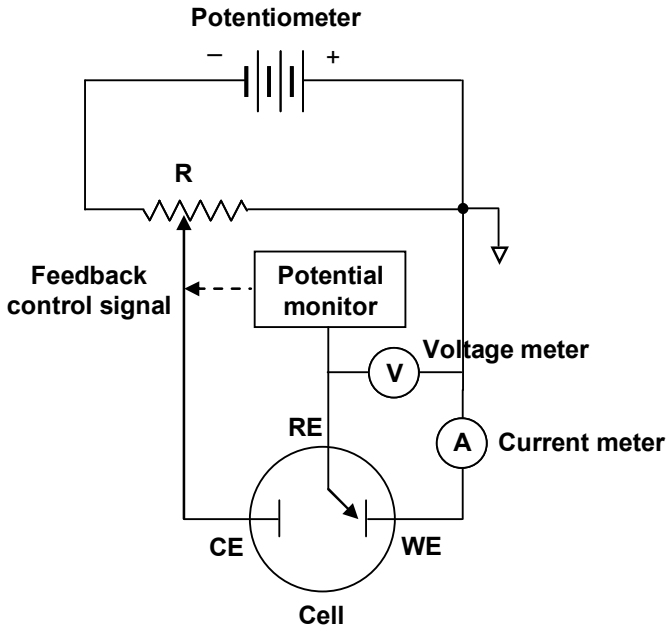

Figure A.3. Schematic illustration of the three-electrode system equipped with a potentiometer.

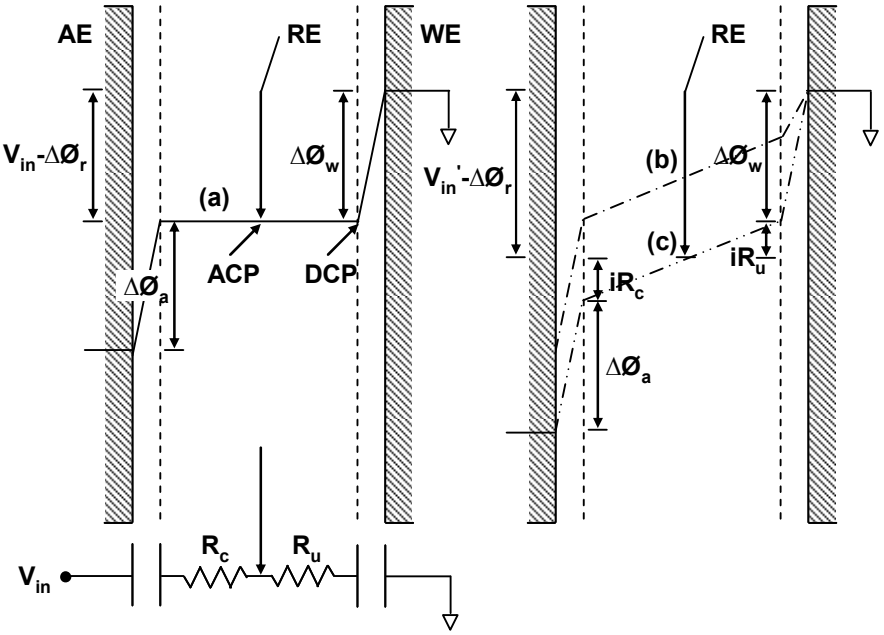

Figure A.4. Schematic illustration of potential gradients between the auxiliary electrode and working electrode in a three-electrode cell [85]. (a) In contrast to the two-electrode system, the interfacial potential difference at the working electrode ($\Delta Ø_w$) is monitored by employing the reference electrode, relative to its own interfacial potential different ($\Delta Ø_r$). Thus, the actual control point (ACP) is much closer to the desired control point (DCP) compared to that in the two-electrode cell. (b) Once reacting species in an analyte solution are electroactive at the given $\Delta Ø_w$, the associated redox reaction would occur, resulting in a charge flow and an IR drop across the bulk solution. (c) Under such finite-current condition, $\Delta Ø_w$ will necessarily drop, but the associated redox reaction could resume immediately, since the applied voltage must be increased by the value of IR drop so as to maintain $\Delta Ø_w$ at the desired value. Although the ACP is brought closer to the DCP by means of the reference electrode, a certain IR drop will be unavoidable because they are still apart. The total cell resistance (R) can be separated into a compensated resistance (R_c) and an uncompensated resistance (R_u). Only the ohmic loss IR_u will be affected by the position of the ACP with respect to the DCP. This implies that the placement of the reference electrode may be a crucial consideration, also depending on the resistance of the solution.

as the auxiliary electrode and reference electrode, respectively. Inside the three-electrode cell, as shown in Figure A.4, the reference electrode is employed as a potentiometric probe to monitor the interfacial potential difference at the working electrode ($Ø_w$) with respect to its own interfacial potential difference ($Ø_r$) [85]. Such a potential difference

between the reference electrode and working electrode is compared to the applied voltage, and according to the discrepancy between them, the applied voltage is altered. As a result of such potentiostatic control, the interfacial potential difference at the working electrode can track the applied voltage under varying current loading conditions. Compared to the two-electrode system, the three-electrode system has the actual and desired control points much closer together, though they are still not the same. There would be some IR drop, albeit negligible [85]. Heretofore, an instrument for the potentiostatic control is assumed to be a potentiometer, which can be regarded as a manual potentiostat. However, in the practical sense, such an instrument is not applicable to the three-electrode system for cyclic voltammetry. For this reason, an op amp-based potentiostat that could perform the potentiostatic control automatically was deployed for the cyclic voltammetry setup used in this work.

A.2.2 Circuit Construction

The cyclic voltammetry setup developed in this work requires three different op amp-based circuits: a potentiostat (OP_1); a current-to-voltage converter (OP_2), and a voltage follower (OP_3 and OP_4), as shown in Figure A.5. In the three-electrode system, as discussed in section A.2.1, the potentiostat is employed to ensure the potential difference between the reference electrode and working electrode follows the applied voltage provided by an excitation signal generator, that is, LabVIEW along with the Field Point modules in this setup. The potentiostat (OP_1) in this circuit depends on a fully-differential op amp (THS4141, Texas Instruments) that was developed and demonstrated by S. M. Martin *et al.* [86]. The fully-differential op amp controls the voltages of both the auxiliary electrode and working electrode to achieve twice the applicable range of

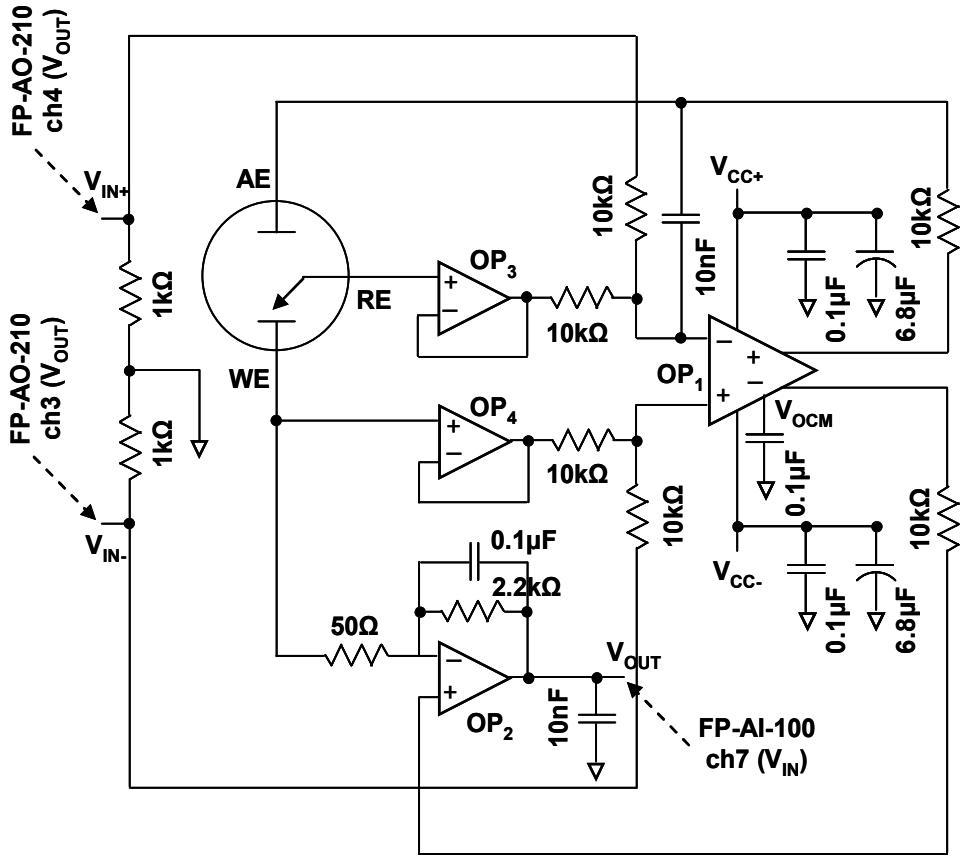

Figure A.5. Schematic diagram of op amp-based circuits in the developed cyclic voltammetry setup: a potentiostat (OP_1), current-to-voltage converter (OP_2), and voltage follower (OP_3 and OP_4). The op amp-based circuits are interfaced with the LabVIEW-controlled Field Point modules: the voltage output module (FP-AO-210) for applying voltage excitations and the voltage input module (FP-AI-100) for reading current responses.

voltage excitations of a single-ended op amp-based potentiostat [87]. With the potentiostat, the circuit employs the voltage followers (OP_3 and OP_4) that are based on a single-ended op amp (LM741CN, National Semiconductor) to measure the potential difference between the reference electrode and working electrode without drawing any current from the cell. This voltage is compared to a differential source voltage, and their difference is applied to the cell through the fully-differential op amp [86]. The single-

ended op amp-based current-to-voltage converter (OP_2) is connected to the working electrode to measure redox currents in the cell. Due to the extremely high input resistance of the op amp (2M Ω), the current bypasses through the resistor. Thus, the voltage at the output of the op amp (V_{out}) is

$$V_{out} = -I \times R \,, \qquad \text{(A.1)}$$

which means that the current can be calculated from the measured voltage and the applied resistance. During the actual operation, the LabVIEW-controlled Field Point module (FP-AI-210), an excitation signal generator in this setup, sweeps the potential between the reference electrode and working electrode through the potentiostat. The current that develops in the cell is then measured as a function of the applied voltage. The output voltage of the current-to-voltage converter, which is proportional to the current from the cell, is recorded by the LabVIEW-controlled Field Point module (FP-AI-100) for data analysis.

A.2.3 LabVIEW Programming

In the cyclic voltammetry setup built in this work, the LabVIEW-based control program provides two functions: signal generation and data input/output. Accordingly, the program is divided by two parts as shown in the block diagrams (Figure A.6).

The voltage-time function for the cyclic voltammetry must be based on a triangular waveform. The triangular waveform produces the forward and then the reverse scan. The voltage is ramped from an initial voltage to a final voltage, the scan direction is then reversed, and the voltage is returned to the initial voltage in the end. The change of voltage with time during the scan is referred to as a scan rate. In fact, the scan is not continuous but staircase, which is related to the resolution of a signal generator. In this

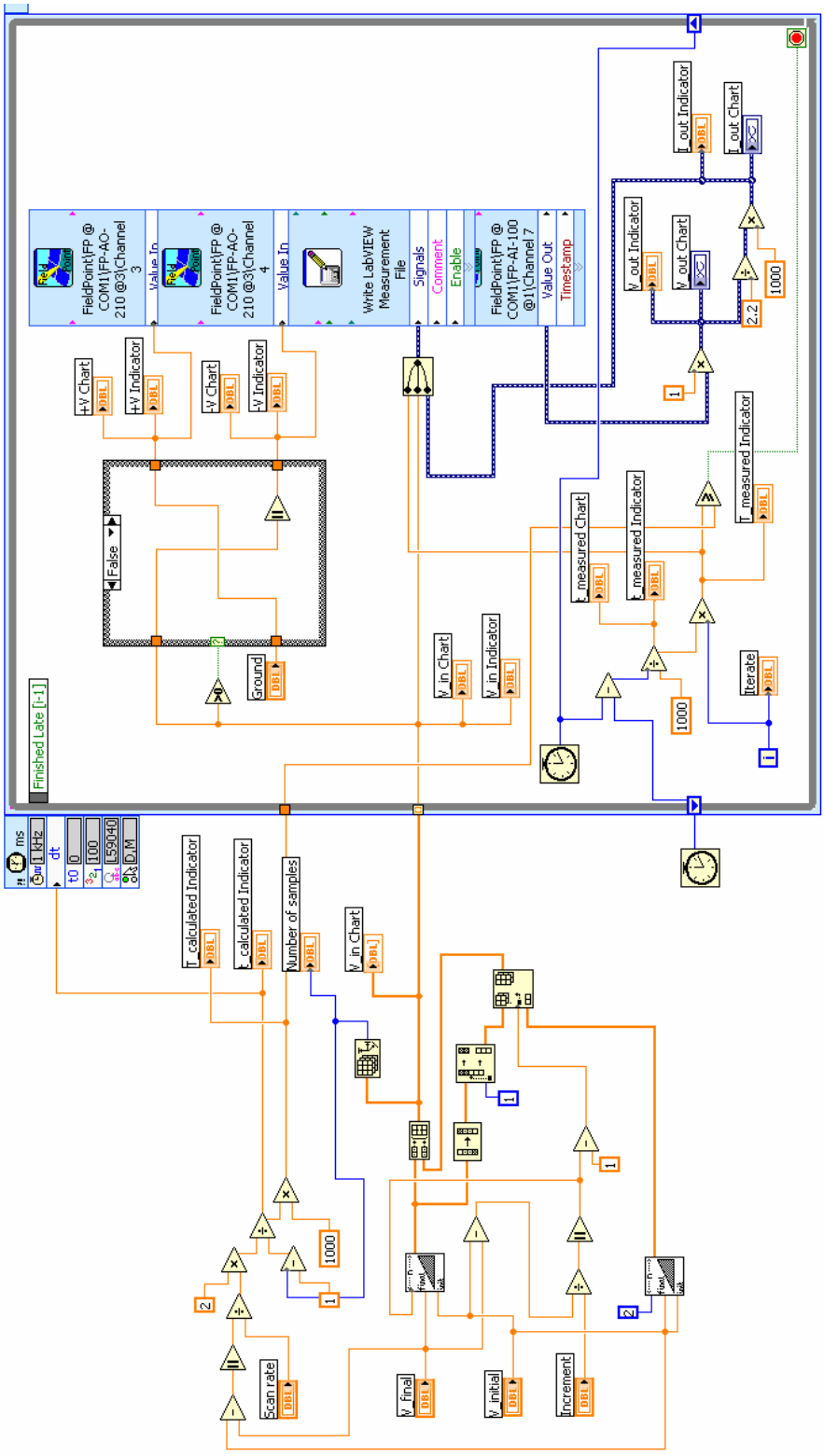

Figure A.6. Block diagram of the LabVIEW-based control program for cyclic voltammetry.

respect, the change of voltage in each step is denoted as an increment. To create the triangular waveform-based voltage-time function, those four parameters: initial and final voltages, a scan rate, and an increment are inputted to the signal generation block as illustrated in Figure A.7 (a). In the actual operation, those inputs can be selected via the front panel of the program as exhibited in Figure A.8. Figure A.7 (b) is the detailed view of the way to set a ramp pattern function in the signal generation block. First, the number

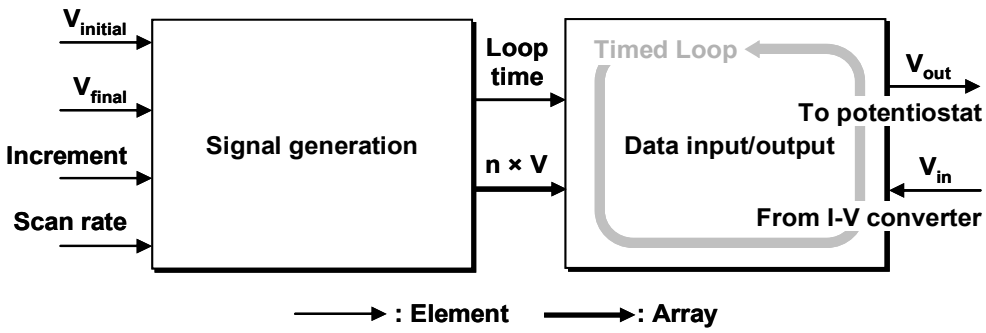

(a)

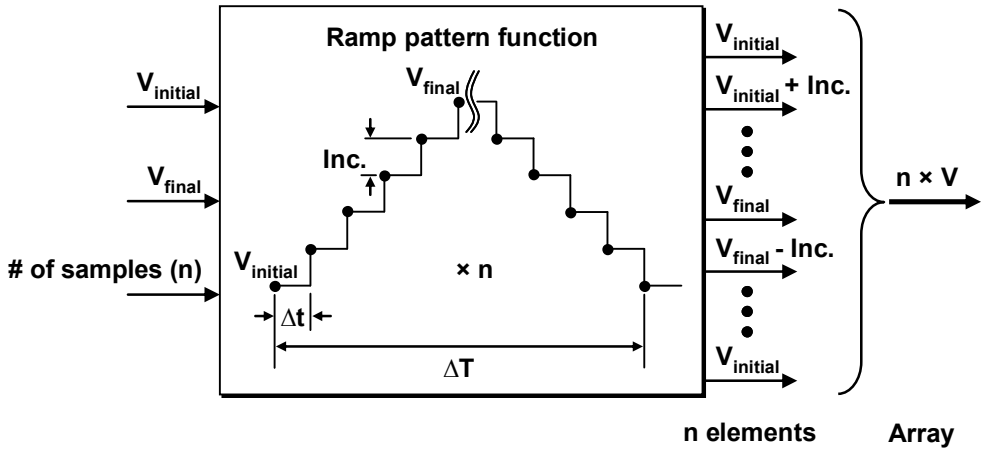

(b)

Figure A.7. Working principle of the LabVIEW-based control program: (a) overview of the program structure consisting of the signal generation division and the data input/output division; (b) detailed view of the signal generation part, and (c) detailed view of the data input/output part.

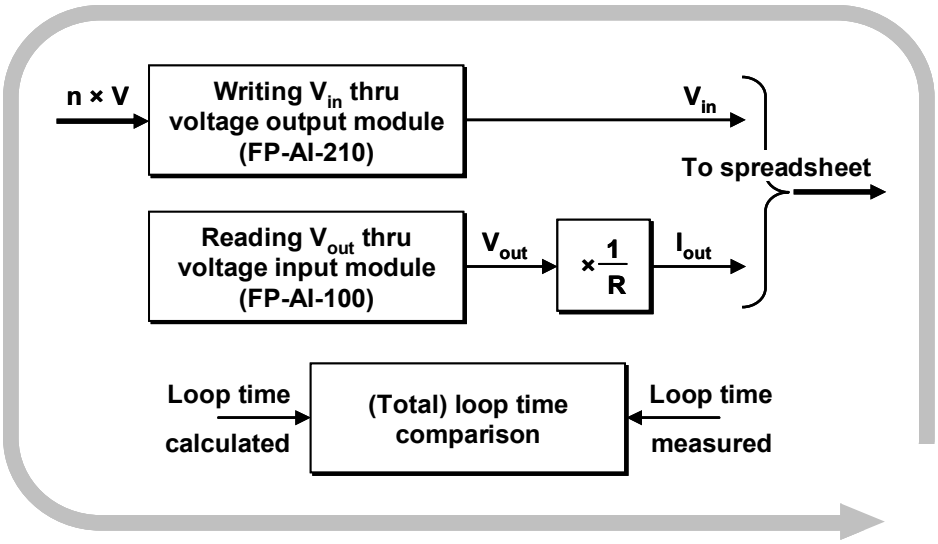

(c)

(Fig. cont'd) Working principle of the LabVIEW-based control program.

of samples (n) indicating the number of discrete values of the voltage is computed

$$n = \frac{\left|V_{initial} - V_{final}\right|}{Increment} \times 2, \tag{A.2}$$

thereby resulting in the array of values of the voltage. Subsequently, a loop time (Δt) determining the duration of time elapsed between two successive values of the voltage is set by

$$\Delta t = \frac{\left|V_{initial} - V_{final}\right|}{Scanrate} \times \frac{1}{n}. \tag{A.3}$$

Thus, the total loop time (ΔT) can be calculated as

$$\Delta T = \Delta t \times n. \tag{A.4}$$

As shown in Figure A.7 (c), the data input/output block is based on the timed loop. The time duration of each loop is determined by the loop time. For each loop, the values of the voltage in a queue are called one by one. Then, the designated value of voltage is

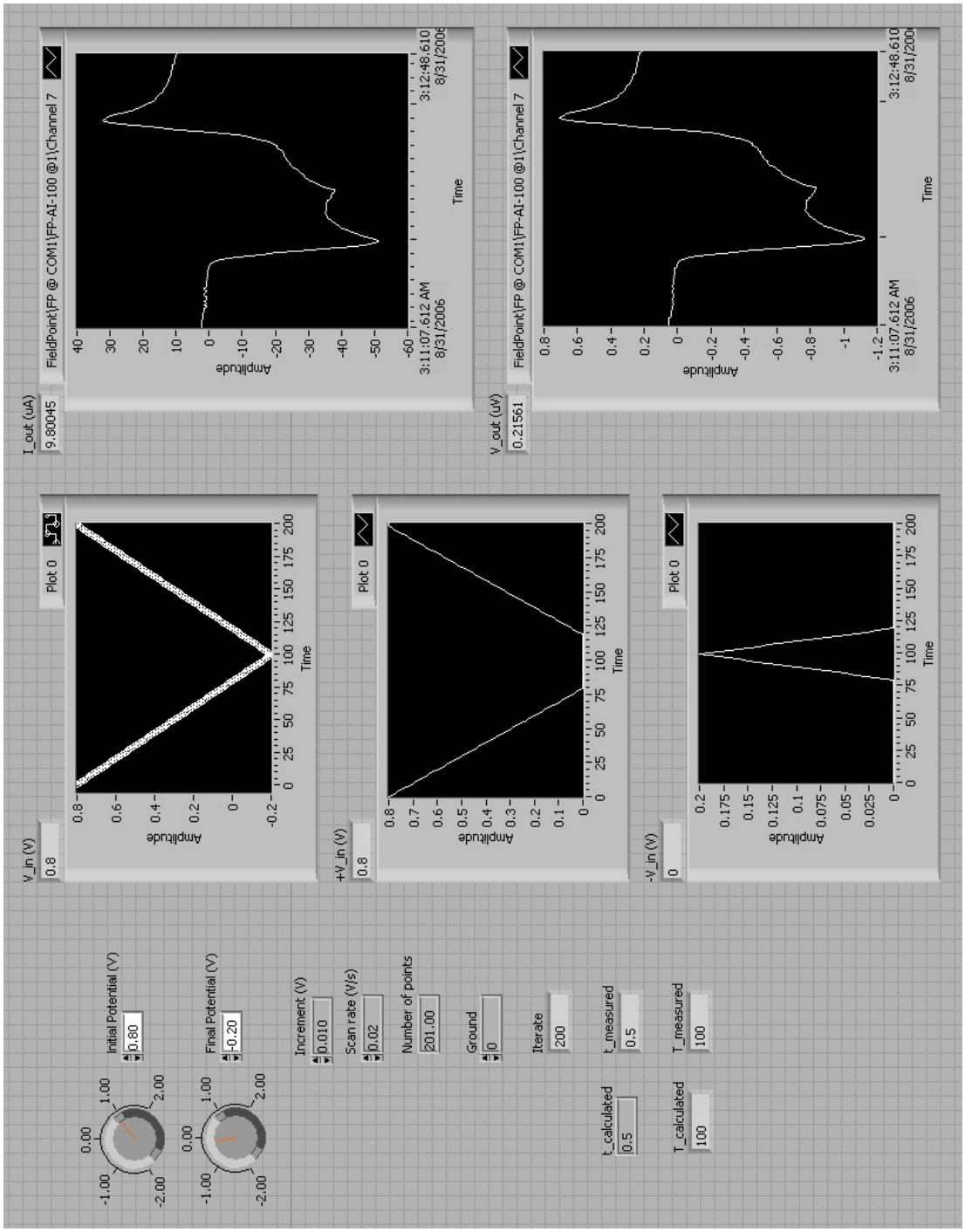

Figure A.8. Front panel of the LabVIEW-based control program for cyclic voltammetry. Cyclic voltammetry in 1 M KNO_3 + 4 mM $K_3Fe(CN)_6$ at a scan rate of 50 mV/s is underway.

applied to the potentiostat through the Field Point module (FP-AI-210). Simultaneously, the converted value of the voltage is measured at the current-to-voltage converter through the Field Point module (FP-AI-100), then it is converted back to the value of the current. Also, the value of the applied voltage and the measured current are recorded pairwise in each loop. Those outputs can be monitored via the front panel of the program as displayed in Figure A.8. At the end of the loop iteration, the resulting arrays of values of the applied voltage and the measured current are stored in spreadsheet format to give the associated cyclovoltammogram. Additionally, the actual loop time is measured in each loop and then compared to the desired loop time; certainly, no difference is allowed between them. However, too high scan rates and/or too small increments would produce too many values of the voltage to be swept in a given time, which could cause a discrepancy between the calculated loop time and measured loop time as summarized in Table A.1. As a result of such discrepancy, the voltage excitations and current responses in the cyclovoltammogram are distorted, which is demonstrated using the ferricyanide/ferrocyanide redox couple in the following section.

A.3 System Validation Test

The developed cyclic voltammetry setup underwent system validation tests after construction. For this application, a reversible redox couple, ferricyanide/ferrocyanide, was applied to the constructed cyclic voltammetry setup to validate the system. For this experiment, potassium ferricyanide ($K_3Fe(CN)_6$, Sigma-Aldrich) and reagent grade potassium nitrate (KNO_3, Sigma-Aldrich) were employed. 1 M KNO_3 was used as a supporting electrolyte that would suppress the migration of charged reacting species. Based on this supporting electrolyte, 1, 2, 4, and 8 mM $K_3Fe(CN)_6$ were prepared for the

system validation test to observe the dependence of analyte concentration on the current responses. A platinum wire working electrode (about 1 mm^2), a silver/silver chloride (Ag

Table A.1. Applicable scan rate and increment determination by comparing the measured (actual) loop time to the calculated (desired) loop time. The initial voltage was 0 V and the final voltage was 0.5 V. In this voltage range, at a scan rate of 100 mV/s, increments smaller than 12 mV was not allowed. Thus, at a scan rate of 50, 20, and 10 mV/s, the minimal increment was determined to be 7, 3, and 2 mV, respectively.

Scan rate (mV/s)	Increment (mV)	Number of values of voltage	Loop time calculated (seconds)	Loop time measured (seconds)
100	50	19	0.556	0.556
	25	39	0.264	0.264
	12	83	0.122	0.122
	10	99	0.102	0.204/0.102
50	25	39	0.526	0.526
	10	99	0.204	0.204
	7	141	0.143	0.143
	5	199	0.101	0.202/0.101
20	10	99	0.51	0.51
	5	199	0.253	0.253
	3	333	0.151	0.151
	2	499	0.1	0.2/0.1
10	5	199	0.505	0.505
	2	499	0.201	0.201
	1	999	0.1	0.2

/AgCl) reference electrode in 3.5 M KCl (WRE5001, Weiss Research), and a platinum wire coil auxiliary electrode were immersed in the prepared $K_3Fe(CN)_6$ solution. Prior to the experiment, the working electrode was polished with emery paper and rinsed with DI water. For the ferricyanide/ferrocyanide redox couple, the voltage window was between 800 and 0 mV (versus Ag/AgCl). For a fixed increment of 10 mV, four different scan rates, 10, 20, 50, and 100 mV/s, were applied for the system validation test to observe the dependence of scan rate on the current responses.

Cyclic voltammetry was carried out in 1 M KNO_3 with various $K_3Fe(CN)_6$ concentrations: 1, 2, 4, and 8 mM, at a range of scan rates: 10, 20, 50, and 100 mV/s. Figure A.9 (a) shows the cyclovoltammogram in 1 M KNO_3 + 4 mM $K_3Fe(CN)_6$ at a scan rate of 50 mV/s. At the initial potential of 800 mV (versus Ag/AgCl), a small anodic current appeared, which instantly disappeared as the scan was continued. This initial anodic current is believed to arise from the oxidation of water to oxygen [88]. No current was detected between a potential of 700 and 400 mV (versus Ag/AgCl) since no reducible or oxidizable species existed in this potential range. At 400 mV (versus Ag/AgCl), a cathodic current began to develop due to the reduction of ferricyanide ions to ferrocyanide ions, which can be expressed as [88]:

$$Fe(CN)_6^{3-} + e^- \rightarrow Fe(CN)_6^{4-}. \qquad (A.5)$$

At a potential of 0 mV (versus Ag/AgCl), the scan direction was reversed. The current, however, continued to be cathodic although the scan was toward more positive potentials because the potentials were still negative enough to cause the reduction of $Fe(CN)_6^{3-}$. At potentials more positive than about 250 mV (versus Ag/AgCl), the reduction of $Fe(CN)_6^{3-}$ no longer took place and the current became anodic. The anodic current arose

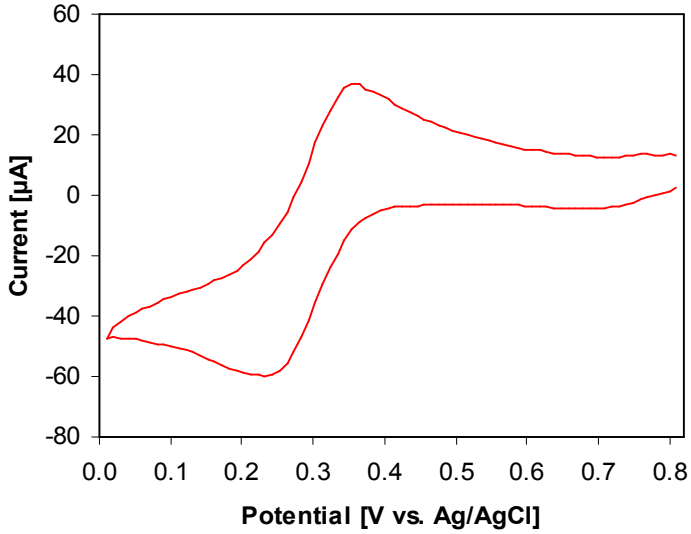

(a)

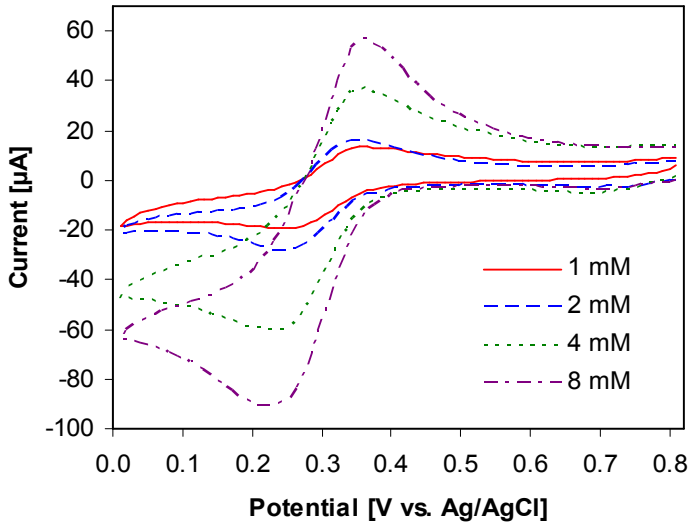

(b)

Figure A.9. Cyclovoltammograms for the validation of the developed system: (a) cyclovoltammogram for the ferricyanide/ferrocyanide redox couple (4 mM $K_3Fe(CN)_6$) in 1 M KNO_3; (b) effect of $K_3Fe(CN)_6$ concentration on the redox currents, and (c) effect of scan rate on the redox currents. Temperature was 22.5°C, electrode area was about 1 mm^2, scan rate was 50 mV/s, and potential window was 0.8 to 0 V (versus Ag/AgCl).

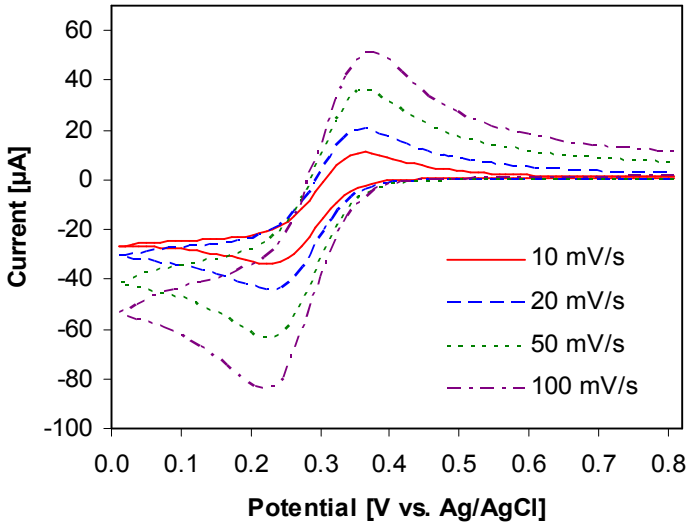

(c)

(Fig. cont'd) Cyclovoltammograms for the validation of the developed system: (a) Cyclovoltammogram for the ferricyanide/ferrocyanide redox couple (4 mM $K_3Fe(CN)_6$) in 1 M KNO_3; (b) effect of $K_3Fe(CN)_6$ concentration on the redox currents, and (c) effect of scan rate on the redox currents.

from the oxidation of $Fe(CN)_6^{4-}$ that was produced from the reduction of $Fe(CN)_6^{3-}$ during the forward scan. This anodic current peaked and then decreased as the accumulated $Fe(CN)_6^{4-}$ near the electrode surface was consumed by the oxidation reaction. Additionally, the effects of the analyte concentration and the scan rate on the current response were examined, which resulted in an increase of oxidation/reduction currents with $K_3Fe(CN)_6$ concentration and scan rate as shown in Figures A.9 (b) and A.9 (c), respectively.

As discussed in section A.2.3, too fast scan rates and/or too small increments would cause difference between the desired loop time and actual loop time. As shown in Table A.1, too small increments at a given scan rate, such as 10 mV at a scan rate of 100 mV/s, 5 mV at a scan rate of 50 mV/s, and 2 mV at a scan rate of 20 mV/s, created a

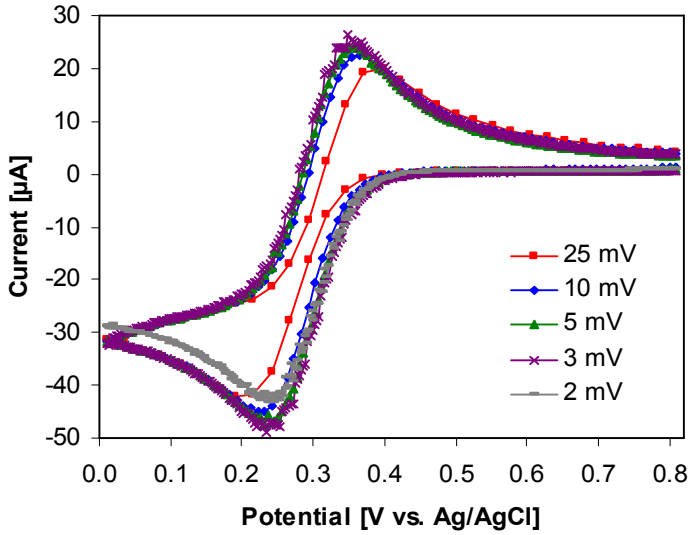

Figure A.10. Effect of increment on the voltage excitations and current responses. Cyclovoltammogram for the ferricyanide/ferrocyanide redox couple (4 mM $K_3Fe(CN)_6$) in 1 M KNO_3. Temperature was 22.5°C, electrode area was about 1 mm^2, scan rate was 20 mV/s, and potential window was 0.8 to 0 V (versus Ag/AgCl).

mismatch between the calculated loop time and measured loop time. As shown in Figure A. 10, for a fixed scan rate of 20 mV/s, increments in a range of 2 to 25 mV were applied, which determined the number of values of the voltage. In consequence, a too small increment (3 mV) accompanying too many values of the voltage (532 samples) created appreciable noise. Further, the smaller increment (2 mV) underwent an incomplete cycle, a significant noise, and a breakaway from the correct cyclovoltammogram. This problem is essentially because all events in the loop could not be completed in a given loop time, which is related to the limited performance of the cyclic voltammetry setup. With a scan rate of 20 mV/s, increments larger than 5 mV were required for the desired cyclovoltammogram. Thus, in general, the faster a scan rate is, the smaller an increment is applicable. An increment of 5 mV along with a scan rate of 20 mV/s produced 318 values of the voltage and a loop time of 0.25 seconds. The higher increment (10 mV)

belonging to 158 values of the voltage resulted in the desired cyclovoltammogram as well. However, a too large increment (25 mV) accompanying too few values of the voltage (62 samples) also created the incorrect cyclovoltammogram, which is related to the resolution of the staircase scan provided by the LabVIEW-based control program.

A.4 References

[83] F. Scholz, *Electroanalytical Methods: Guide to Experiments and Applications,* Berlin and Heidelberg: Springer-Verlag, 2002.

[84] R. H. Bishop, *Learning with LabVIEW 7 Express,* Upper Saddle River: Pearson Prentice Hall, 2003.

[85] P. T. Kissinger, "Introduction to Analog Instrumentation," in *Laboratory Techniques in Electroanalytical Chemistry 2nd ed.,* P. T. Kissinger and W. R. Heineman, Ed., New York: Marcel Dekker, Inc., 1996, pp. 165-194.

[86] S. M. Martin, F. H. Gebara, T. D. Strong, and R. B. Brown, "A Low-Voltage, Chemical Sensor Interface for Systems-On-Chip: The Fully-Differential Potentiostat," in *2004 IEEE International Symposium on Circuits and Systems,* 2004, pp. 892-895.

[87] J. Karki, "Fully Differential Amplifiers," Texas Instruments Inc., Dallas, TX, Tech. Rep. SLYT-165, 2000.

[88] S. Petrovic, "Cyclic Voltammetry of Hexachloroiridate(IV): An Alternative to the Electrochemical Study of the Ferricyanide Ion," *The Chemical Educator,* vol. 5, pp. 231-235, October 2000.

VITA

Woosuk Sung was born in Keoje, Korea, in February 1979. He graduated from Bosung High School, Seoul, in February 1997. Beginning in March 1997, he attended Sungkyunkwan University, Seoul, where he obtained the degree of Bachelor of Science in both mechanical and electrical engineering in August 2003. After graduation, he pursued his graduate studies in the department of Electrical and Computer Engineering at Louisiana State University. At the December 2006 commencement, he will receive the degree of Master of Science in Electrical Engineering.